Model Predictive Control of a Grid-Connected Converter With LCL-Filter

by

Joanie Michellene Claudette Geldenhuys

Thesis presented in partial fulfilment of the requirements for the degree of Master of Science in Electrical and Electronic Engineering in the Faculty of Engineering at Stellenbosch University

Department of Electrical and Electronic Engineering,
University of Stellenbosch,
Private Bag X1, Matieland 7602, South Africa.

Supervisors:

Prof. H. du T. Mouton and Dr. A. Rix

March 2018

Declaration

By submitting this thesis electronically, I declare that the entirety of the work contained therein is my own, original work, that I am the sole author thereof (save to the extent explicitly otherwise stated), that reproduction and publication thereof by Stellenbosch University will not infringe any third party rights and that I have not previously in its entirety or in part submitted it for obtaining any qualification.

Date: 2017/12/01 .....

Abstract

Model Predictive Control of a Grid-Connected Converter With LCL-Filter

J.M.C. Geldenhuys

Department of Electrical and Electronic Engineering,
University of Stellenbosch,
Private Bag X1, Matieland 7602, South Africa.

Thesis: MScEng (E&E)

March 2018

Improved efficiency of power conversion is high priority when it comes to renewable energy applications. Model predictive control (MPC) can be used to optimise the switching pattern applied in the converter to reduce switching losses. During this research the suitability of a direct MPC strategy with long horisons is evaluated for current control of a three-phase two-level grid-tied converter with LCL-filter.

A cost function was formulated to include two weighted control objectives, namely reducing the reference tracking error and switching frequency. The grid voltage was incorporated into the state-space model as an additional input vector. Therefore the optimisation approach, used to transform the cost-function minimisation problem towards the integer least-squares (ILS) problem, had to be reworked to consider this additional element, hereby extending on previous work done on the integer quadratic programming formulation for long horisons. A sphere decoding algorithm was incorporated to reduce the computational burden.

The current controller shows fast transient response and good reference tracking of the fundamental 50 Hz component. The developed strategy complies to the grid-side current harmonic limits set out in the South African grid code at high switching frequencies, but is unable to comply to the even and high-order harmonic limits at low switching frequencies.

Uittreksel

Model Voorspellende Beheer van 'n Netwerk-Gekoppelde Omsetter met 'n LCL-Filter

("Model Predictive Control of a Grid Connected Converter With LCL-Filter")

J.M.C. Geldenhuys

Departement Elektriese en Elektroniese Ingenieurswese,
Universiteit van Stellenbosch,
Privaatsak X1, Matieland 7602, Suid Afrika.

Tesis: MScIng (E&E)

Maart 2018

Verbeterde doeltreffendheid van kragomsetting is 'n hoë prioriteit wat betref hernubare energie toepassings. Model voorspellende beheer (MVB) kan gebruik word om die skakelpatroon wat in die omsetter toegepas is te optimeer om skakelverliese te verminder. Gedurende hierdie navorsing is die geskiktheid van direkte MVB met lang horisonne ge-evalueer vir die beheer van 'n drie-fase, twee-vlak, netwerkgekoppelde omsetter met 'n LCL-filter.

'n Kostefunksie is geformuleer om twee beheermikpunte, naamlik die vermindering van die stroomvolgfout en skakelfrekwensie in te sluit. Die netwerkspanning is by die toestandsruimte model as 'n bykomende intreevektor inkorporeer. Hierdie bykomende element het gemaak dat die optimeringsbenadering wat gebruik is om die kostefunksie minimeringsprobleem tot die kleinste vierkant probleem te transformer, gewysig moes word. Dit is 'n voortsetting van vorige werk oor heeltallige kwadratiese programmeringsformulering vir lang horison toepassings. 'n Algoritme vir 'n sfeer dekodeerder is geïmplementeer om die berekeningslas te verminder.

Die stroombeheerder wys vinnige oorgang en bied akkurate stoomvolging van die 50Hz fundamentele frekwensie komponent. Die ontwikkelde strategie voldoen teen hoë skakelfrekwensies aan netwerkstroom harmoniekbeperkings soos in die Suid-Afrikaanse netwerkkode uiteengesit, maar kan nie teen lae frekwensies voldoen aan die ewe en hoë orde harmoniekbeperkinge nie.

List of Publications

Geldenhuys, J., Mouton, H.d.T. and Rix, A.: Current control of a grid-tied inverter with LCL-Filter through model predictive control. : *Southern African Universities Power Engineering Conference (SAUPEC)*. Vereeniging, South Africa, 2016.

Geldenhuys, J., Mouton, H.d.T., Rix, A. and Geyer, T.: Model predictive control of a grid connected converter with LCL-Filter. : *Proceedings of the 17th IEEE Workshop on Control and Modeling for Power Electronics (COMPEL 2016)*. Trondheim, Norway, 2016.

Acknowledgements

To my Creator, thank you for the opportunity and ability You have given me, and how You have always strengthened me during my hardest times. I give You all the glory.

My sincere gratitude to my project supervisors and mentors, Professor Mouton and Dr. Rix. Thank you for your patience, understanding, guidance and the sharing of your knowledge during this research.

Scatec Solar, thank you for your generous support in providing me with a scholarship. I would not have had the opportunity to do a master's degree without your support.

Heinrich, your amazing drive and perseverance inspires me to prevail and to see beyond that which seems impossible. Thank you for never allowing me to doubt myself.

My parents, Willem and Felicity Engelbrecht, you have always given a hundred-and-ten per cent of yourselves to your children. I realise now how much you have sacrificed so that I can grow and excel. Your dedicated prayer also means a lot to me.

My parents-in-law, Jacques and Lucresia Geldenhuys, thank you for the support you have given me and your son, Heinrich.

Thank you to all my family and friends who kept us in their prayers and provided support and understanding.

Dedication

This thesis is dedicated to my husband Heinrich, you have changed my life in radical and exciting ways. Thank you for being an inspirational life partner.

Contents

List of Figures

List of Tables

Nomenclature

Constants

$\pi =$	3.14159
$\mathrm{j} =$	$\sqrt{(-1)}$

Variables

C	Capacitance	[F]
f	Frequency	[Hz]
f_s	Sampling frequency	[Hz]
f_{sw}	Switching frequency	[Hz]
i	Instantaneous current	[A]
J	Cost	[ ]
k	Discrete time index	[ ]
L	Inductance	[H]
m_a	Amplitude modulation index	[ ]
N	Horison length	[ ]
R	Resistance	[Ω]
t	Time	[s]
T_s	Sampling period	[s]
u	Switch state	[ ]
v	Instantaneous voltage	[V]
Z	Impeadance	[Ω]
λ	Weighting factor	[ ]
ϕ	Modulation angle	[deg]
ρ	Radius	[ ]
ω	Angular velocity	[rad/s]

Vectors and Matrices

$\boldsymbol{H}$	Lattice-generator (transformation) matrix
$\boldsymbol{u}$	Switch state (three-phase)

$\boldsymbol{v_g}$	Grid voltage vector
$\boldsymbol{x}$	State vector
$\boldsymbol{y}$	Output vector (three-phase)
$\boldsymbol{U}$	Switching sequence
$\boldsymbol{Y}$	Predicted output sequence
$\boldsymbol{Y}^*$	Reference output sequence
$\boldsymbol{\xi}$	Xi
$\boldsymbol{\Gamma}$	Gamma
$\boldsymbol{\Theta}$	Theta
$\boldsymbol{\Upsilon}$	Upsilon
$\boldsymbol{\Psi}$	Psi

Subscripts

a	a-phase
abc	abc reference frame
b	b-phase
c	c-phase
C	Capacitor
e	Error
g	Grid
ini	Initial
opt	Optimal
s	Sampling
sw	Switching
unc	Unconstrained
α	α-component in the $\alpha\beta$ reference frame
$\alpha\beta$	$\alpha\beta$ reference frame
β	β-component in the $\alpha\beta$ reference frame

Abbreviations

A	Ampere
AC	Alternating current
AD	Active damping
dB	Decibel
DC	Direct current
DNI	Direct nominal irradiation
DPC	Direct power control

DTC	Direct torque control
EMC	Electromagnetic compatibility
F	Farad
FCS	Finite-control set
FLOPS	Floating point operations
FOC	Field orientated control
GC	Grid code
GPC	Generalised predictive control
H	Henry
Hz	Hertz
IEC	International Electronic Commission
ILS	Integer least-squares
IM	Induction machine
IRP	Integrated Resource Plan
LCL	Inductor-capacitor-inductor configuration
LCOE	Levelised cost of electricity
k	Kilo
KVL	Kirchoff's voltage law
MPC	Model predictive control
MPCC	Model predictive current control
MPDCC	Model predictive direct current control
MPDTC	Model predictive direct torque control
MV	Medium voltage
MW	Megawatt
MVB	Model voorspellende beheer
NERSA	National energy regulator of South Africa
NPC	Neutral-point-clamped
PI	Proportional-integral
PV	Photovoltaic
PWM	Pulse width modulation
REI4P	Renewable Energy Independent Power Producer Procurement Programme (REIPPPP)
s	Seconds
SA	South Africa
STFT	Short-time Fourier transform
SVM	Space vector modulation
THD	Total harmonic distortion

TWh	Terawatt hour
VR	Virtual resistor
VOC	Voltage-orientated control
VSC	Voltage-source converter
V	Volts

Chapter 1

Introduction

1.1 Background to the research problem

Energy is regarded as an important building block of society and is required for the creation of goods from natural resources [17]. Fossil fuels such as oil, coal and gas are still predominantly used for electricity production, but renewable energy sources have since the 1970s slowly gained importance [17]. Global energy demand and access of renewable energy sources to the electricity grid are rapidly growing in proportion [18], as can be seen in Figure 1.1. Despite an increase in energy efficiencies over time, an immense increase in global energy demand is predicted from now until 2040, especially in developing countries [19; 20; 21].

Renewable energy is currently projected as the fastest-growing energy

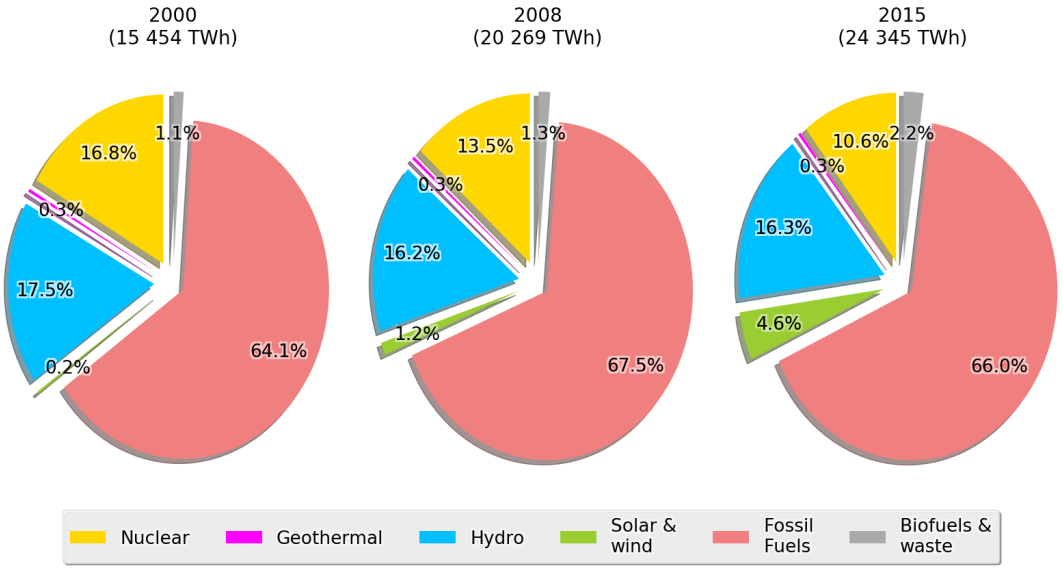

Figure 1.1: Total electricity produced globally, analysed according to source. Produced from data in [1; 2; 3].

source with its global consumption predicted to increase by an average of 2.6% per year until 2040 [19]. Integrating renewable energy sources into the grid can bring many environmental and economic benefits [22]. Key challenges entail managing variability of supply from renewable energy sources with regards to integration with the power grid, and remaining competitive with traditional power generation [21]. Renewable energy sources have received growing interest as a valuable means for nations to reduce their carbon emission [23; 24; 25].

Political commitments were made at the United Nations conference on climate change where nations agreed to promote the universal access to renewable energy and its deployment [26; 24; 21]. The South African national objective is to have 30% clean energy by 2025 [27].

South Africa's solar potential is among the highest in the world, yet coal-generated electricity still dominates [28]. Coal, linked to high carbon emissions, supplies 93% of South-African energy [29], and can be dated to the early 1880s when the Kimberley diamond fields were supplied with coal from Vereeniging [30]. This is high compared to the world average which is around 40% [31]. Coal has for many years been the preferred source of electricity generation in South Africa due to abundant local coal reserves, relative cost effectiveness and reliability [30].

In the SA White Paper on Energy Policy published in 1998 it is advocated that South Africa should improve on its energy efficiency [32] in order for the country to maintain its economic competitiveness [33] since worldwide economic development is influenced by the production of electricity [34]. The South African government has realised the importance of creating a sustainable energy mix by investing in renewable energy resources. This led to the White Paper on Renewable Energy in 2003 in which renewable energy investment through well-structured tariffs and creating public awareness on the use of renewable energy and energy efficiency is promoted [35]. The Integrated Resource Plan (IRP) followed in 2010 and the Renewable Energy Independent Power Producer Procurement Programme (REI4P) in 2014 to drive the installation of renewable electricity generation capacity until 2030. Initially the REI4P was seen as an expensive option used to counter criticism of the country's coal dependance and high carbon footprint [4]. However, this later changed due to the increasing competitiveness of the REI4P bidding process, the escalating costs of coal-based electricity generation and the rapidly decreasing costs for wind and photovoltaic power [4]. This trend is supported by the comparison of the levelised cost of electricity (LCOE) for PV and coal-generated electricity in Figure 1.2. Renewable energy is finally gathering momentum in South Africa [4]. In 2014 South Africa was the country with the largest renewable energy asset growth and made the eighth largest investments in renewable energy [36].

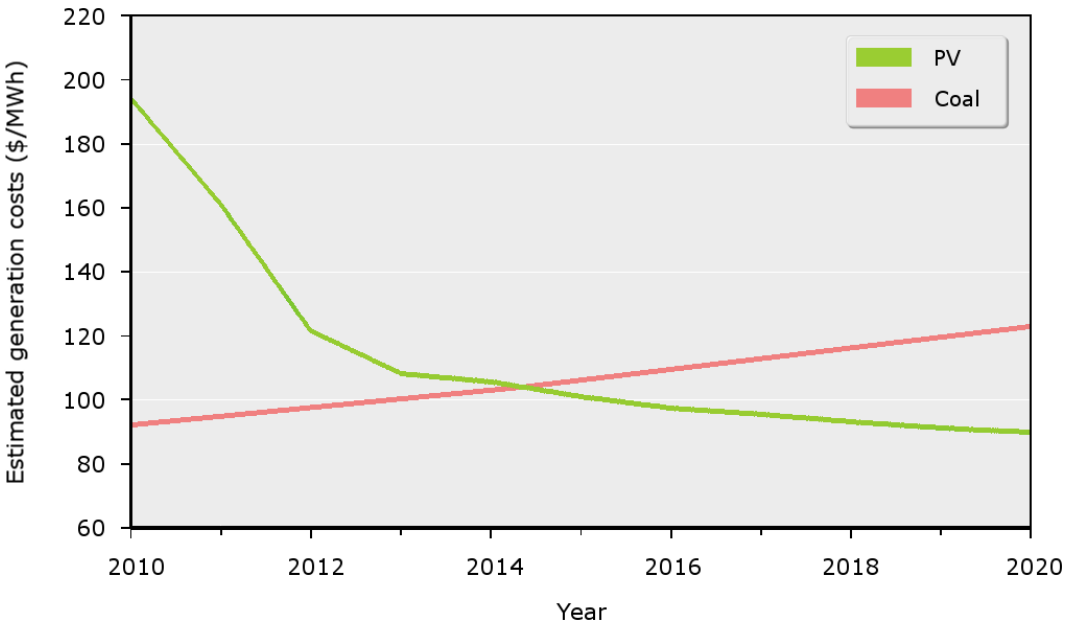

Figure 1.2: Comparison of LCOE costs for PV and coal-generated electricity from actual and predicted data. Reproduced from [4; 5].

1.2 Renewable energy

Sources of electricity generation such as nuclear and fossil fuels (oil, coal and natural gas) are unsustainable as the replenish rate of these resources cannot indefinitely support continued electricity generation in the future [37; 38; 39; 40]. The process of generating electricity from these non-renewable sources also leads to damage of the environment [37]. A more sustainable option is renewable energy as it holds the potential to be economically viable, environmentally friendly and to bring socio-economic benefits such as employment creation [4; 41], which align with the three pillars of sustainable development (economic, environmental and social sustainability).

Renewable energy sources are constantly replenished by the environment with the energy obtained from the sun either directly (for example photo-electric, photo-chemical and thermal), or indirectly (bioenergy, hydro and wind), as well as from other natural phenomena (such as tidal and geothermal energy) [42]. In Figure 1.3 the different types of renewable energy are listed [6; 7].

In South Africa renewable energy can be traced back to 100 years ago when farmers used windmills for pumping water or grinding grain [43; 44]. However it is only from the 1970s that the first attempts were made as to develop renewable energy technologies on a commercially viable scale [43].

These renewable energy technologies have evolved and passed the stage of trying to catch up with fossil fuel technologies and are now rather positioned to have equivalent or surpassing performance [43]. Traditional

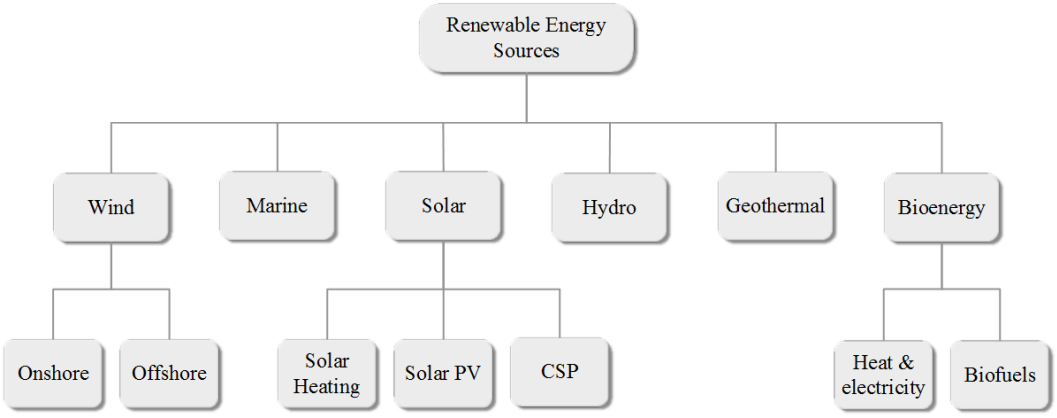

Figure 1.3: Different types of renewable energy. Reproduced from [6; 7].

fossil fuel technologies have undergone a process of refinement spanning over more than a century, requiring trillions of dollars in subsidies, research and development [43]. Currently these traditional technologies require large investment to produce marginal improvement, while many renewable energy technologies are in an innovation phase where small investments are bringing about large performance gains and cost reductions [43].

One of the technologies that greatly influence the performance of renewable energy systems is power electronics [42; 45]. Wind energy systems use power electronic converters to regulate the variable input power and maximise electrical energy converted from the wind energy [42]. Inverters are used in photovoltaic (PV) systems to effectively convert the DC voltage to AC for connection to the electrical grid or other AC applications [42]. A typical grid-connected setup for a PV system is presented in Figure 1.4.

1.2.1 Research focus

Power electronics entail the control and conversion of electricity by means of applying a certain sequence of operation to semiconductor switches [42]. In renewable energy technologies efficiency is a priority especially in high power systems. One measure that can reduce losses in the system is to minimise switching losses by switching the semiconductor devices at lower frequencies. This however compromises the quality of the current injected into the grid. Model predictive control (MPC) can be used to perform current control by effectively managing the trade-off between switching frequency and current reference tracking. It is a control method that has received increasing attention within power electronics and entails online optimisation of a cost function that encompasses the control objectives. Finite control set (FCS) model predictive control, alternatively known as direct MPC, directly changes the switch states of the semiconductor switches, which is therefore seen as the manipulated

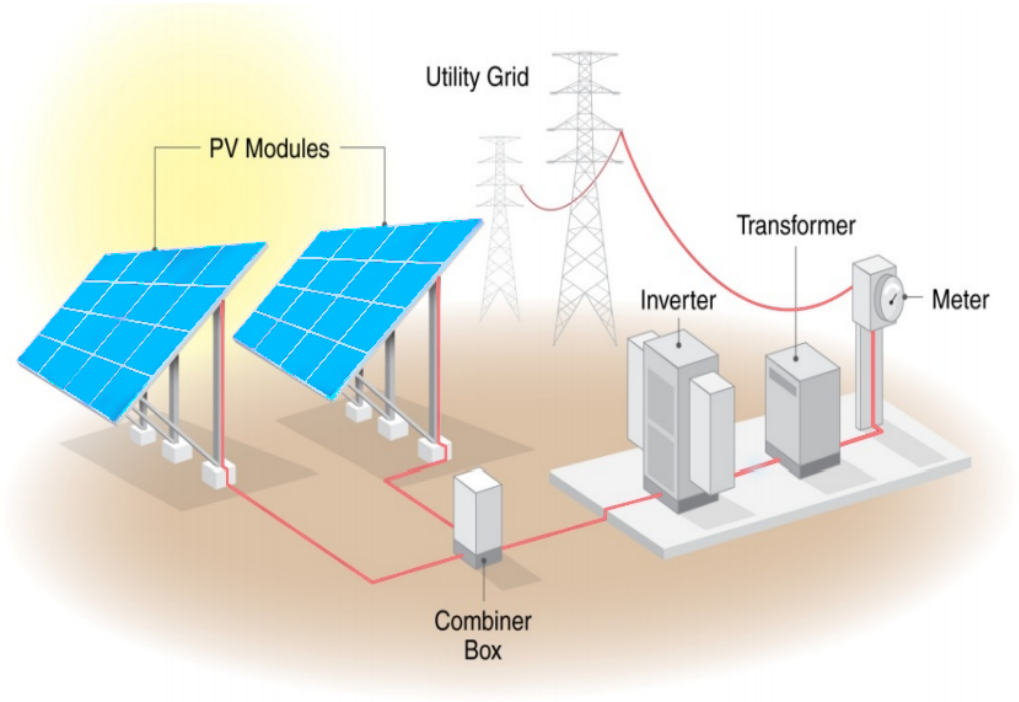

Figure 1.4: General configuration to connect a photovoltaic power plant to the grid [8].

variable of the controller. MPC addresses the modulation and current control need in one computational stage, not needing a modulator, and is an attractive alternative to traditional controllers such as PWM and PI control. However, the optimisation problem of determining the optimal value for the discrete optimisation variable (switching sequence) is very challenging computationally, especially when predictions are considered further into the future, known as long prediction horisons.

In [46] an efficient optimisation algorithm is derived by an amalgamation between sphere decoding concepts and the optimisation approach. The development of this algorithm makes it possible to efficiently solve the optimisation problem for longer prediction horisons by reducing the exponentially increasing computational burden.

There are MPC strategies available that can perform current control for an inverter, but they do not provide for the effect of the grid voltage. The direct model predictive control method used in the research done by [46] seems most suitable for this application, but will have to be extended to incorporate the grid voltage.

1.3 Research statement

Evaluate the suitability of a direct model predictive control technique with long prediction horisons for the current control of a grid-tied inverter with LCL-filter.

1.4 Research objectives

The researcher aims to fulfil the following objectives:

- To develop a mathematical model that describes the behaviour of the three-phase grid-connected converter with a LCL-filter.
- To extend on the work done in [46] regarding the optimisation approach underlying MPC for long horisons to incorporate the effect of the grid voltage.
- To incorporate the following control objectives into a cost function;
  - To minimise current tracking error.
  - To minimise switching frequency.
- To solve the optimisation problem in a computationally efficient manner using the sphere decoding algorithm.
- To implement and evaluate the developed mathematical model and sphere decoder by MATLAB-based simulations.

1.5 Brief overview of the research

Figure 1.5 provides a concise illustration of the process followed in this research:

In **Chapter 2** the background and literature study regarding the research statement are presented in order to provide the reader with the necessary introductory knowledge of the main concepts and theory involved in the study. An overview of the role and application of power converters is given, as well as a review of the different types of control methods available. The suitability of predictive control is described at the hand of the characteristics present in modern control systems and power converters. The model predictive control (MPC) approach is then introduced, where-after the advantages and disadvantages of this approach are discussed. The basic principles according to which MPC functions is also explained before a review is given of the existing research relevant to the study.

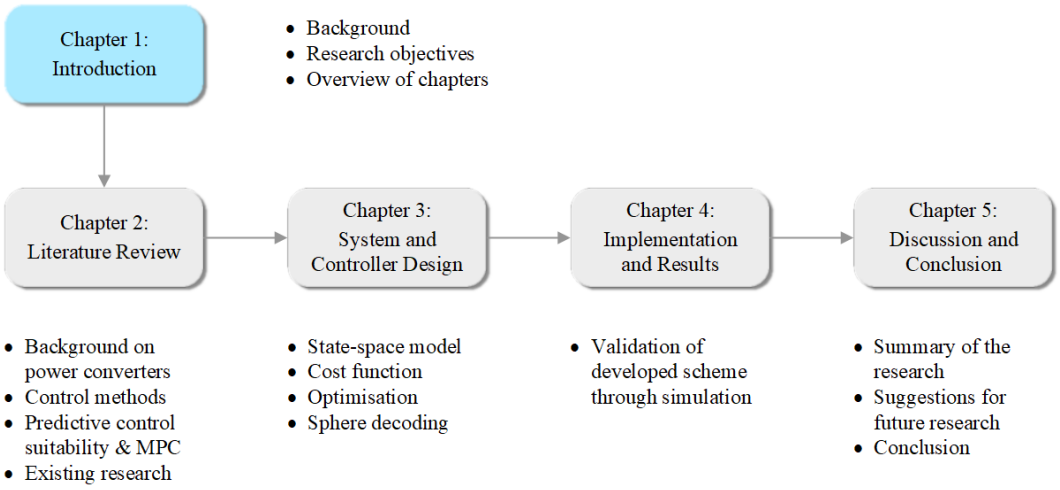

Figure 1.5: Brief overview of the thesis chapters.

The design of the system and controller are discussed in **Chapter 3**. A state-space model is derived to describe the behaviour of the system according to the actuation applied to the switches. The model is similar to the one in [46], except that the grid voltage is included in the model as an input vector alongside the actuation input vector, which differs from the augmented models in [47; 48]. The continuous-time model is then discretised to a discrete-time model. A cost function is compiled according to the control objectives for the system, namely accurate reference tracking and minimisation of the switching frequency. The cost function uses the state-space model to predict system behaviour across the time steps in a prediction horison in order to calculate the overall cost of each available actuation sequence. The actuation sequence that minimises the cost function is the optimal solution, but as the horison length is increased, the solution search enlarges exponentially, implying an exhaustive search through each of the many candidates. The optimisation approach that changes the cost function minimisation problem into an integer least-squares (ILS) problem, is reworked to include the additional input vector of the cost function for the grid voltage. An efficient solving algorithm known as the sphere decoder is used to reduce the computational burden associated with longer horisons by excluding as many sub-optimal solutions from the search as possible.

In **Chapter 4** the control scheme developed in Chapter 3 is implemented as a simulation in order to evaluate its performance. In the first part of the chapter an explanation is given on how the mathematical model is implemented in a MATLAB-based simulation in order to obtain and analyse the results in the time and frequency domain. In the second part the suitability of the developed model is evaluated in terms of the grid-code harmonic distortion limits for the grid current. The evaluation is performed at two different switching frequencies by comparison between four control approaches: MPC

with a short horison, MPC with a long horison, open-loop pulse width modulation and naturally-sampled space vector modulation.

In **Chapter 5** the research is summarised, the main findings are reviewed, suggestions are made for future research and final conclusions are drawn.

Chapter 2

Background and Literature Review

In this chapter a literature review is presented in order to provide background on the applications of power converters and the types of converter control schemes. A motivation as to why predictive control is the preferred method, and an explanation of the characteristics and basic principles of model predictive control, are provided. The need to implement an optimisation algorithm, specifically sphere decoding, will also be explained.

2.1 Power converters

Power converters are used for diverse applications and in many industries, such as the industrial, transportation, power systems, residential sectors and renewable energy. In photovoltaic (PV) systems the power from the solar panel passes through a DC-DC converter that manages the optimal operation of the panel. Thereafter the DC power is converted to AC by an inverter, so that sinusoidal current can be injected into the grid. In Figure 2.1 an example of this setup is given. Power converters for renewable energy generation offer the optimisation of energy extraction, performance and quality of the power injected into the grid [10; 49], and in the case of wind energy eliminates the need for a mechanical gearbox [50].

System stability and dynamic performance were the main focus in traditional control requirements, but today the industry requirements pose more demanding constraints, technical specifications, codes and regulations. These requirements cannot be satisfied with hardware alone, and have to be dealt with by the control system. Therefore more advanced control systems have emerged and power electronic converter design has become an optimisation problem, also having to satisfy various objectives and constraints at once. A list of important objectives, constraints and challenges regarding control in power electronics follows [10]:

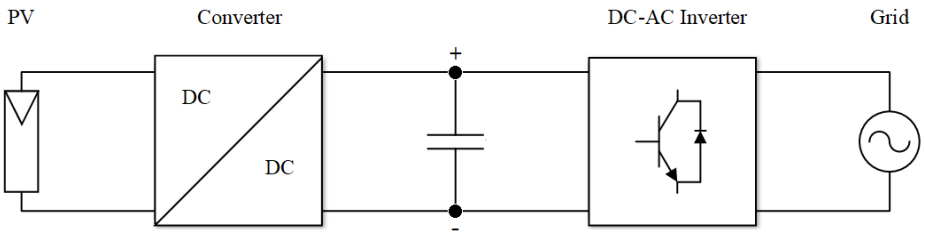

Figure 2.1: System diagram for a renewable energy power converter application. Amended from [9].

- Reduction of switching losses, related to the switching frequency. This drives efficiency and optimal utilisation of semiconductor components.
- Improved dynamics for minimising the tracking error between the controlled variables and their references, as well as optimal disturbance rejection.
- It is challenging to acquire good performance of a non-linear system if its linearised control model is adjusted for a specific operating point. It is desirable to achieve good operation for a wide range of conditions.
- The modulation stage generates harmonic content, which is an inherent characteristic of switched systems. Many applications have restrictions regarding the total harmonic distortion (THD).
- Common-mode voltages are a concern because they induce leakage currents that threaten the lifetime and safety of the system.
- Attention must be paid to the standards and regulations regarding the electromagnetic compatibility (EMC) of the system.
- Each converter topology has its own specific limitations, requirements and constraints, for example forbidden actions such as changing a switch state in a three-level converter from -1 directly to 1 by avoiding the 0 state in-between.

2.2 Types of control methods

In Figure 2.2 a classification of power electronic control methods that are generally applied to power converters and drives is presented. Some of the techniques are only used for drive applications, indicated by the grey boxes in Figure 2.2, and are therefore not applicable to the system described in this study. This classification includes some classical methods and the more complex and recent methods requiring higher computational capabilities. A more detailed discussion on the main control methods follows.

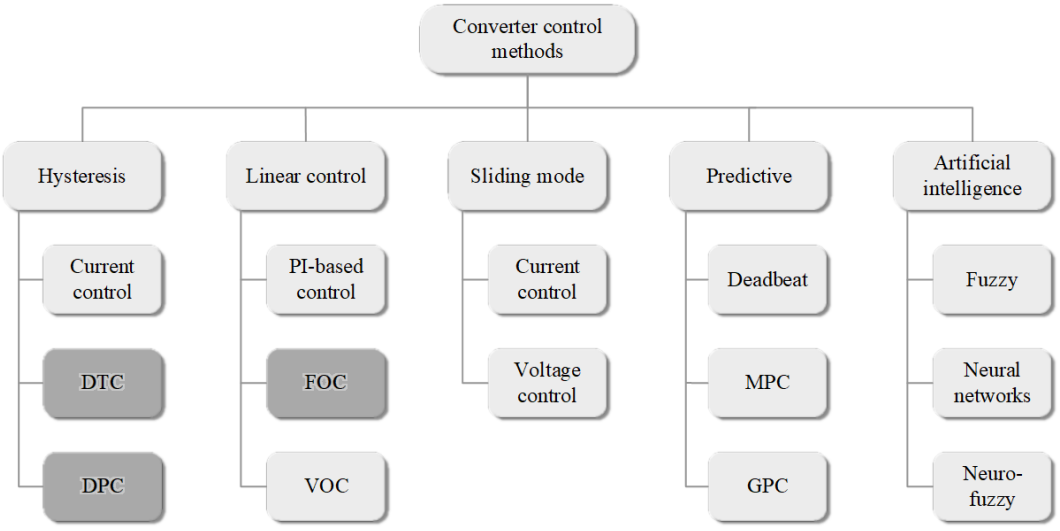

Figure 2.2: A classification of converter control methods for power converters and drives. Amended from [10].

With **hysteresis control** the switch states are determined by comparing the measured variable to a hysteresis error boundary around the reference signal. The switch state is changed as soon as the controlled current reaches the boundary. The method's applications are in the most cases simple like current control, but can also be applied to higher complexity applications like direct torque control (DTC) [51] and direct power control (DPC) [52]. The implementation is simple and does not require highly complex technology [10].

Hysteresis control is well established [11] and originated from analogue electronics. When implemented digitally the scheme requires a very high sampling frequency to continually keep the controlled variables within the hysteresis band. Hysteresis control is problematic for low power applications due to the switching losses [53]. A significant drawback of this control method is its variable switching frequency, dependent on the hysteresis width, load parameters, non-linearity and operating conditions. This causes resonance and a spread of spectral content requiring costly and unwieldy filters [10].

Any **linear controller** can be applied to a power converter that has a modulation stage. A modulator linearises the non-linear converter by generating control signals for the switching devices. The most common linear controller is the proportional-integral (PI) controller. Field-orientated control (FOC) is a general choice for drives [51; 54], while voltage-orientated control (VOC) can be used for grid-connected converters to control the current [55]. A very established approach used in conjunction with linear control is pulse width modulation (PWM) [11]. In this approach a PWM modulator compares the sinusoidal reference signal to a triangular carrier signal, generating a pulsed waveform to control the switching. For example, when the instantaneous value of the carrier is less than that of the reference

signal, the switch state is changed so that the output signal increases, and vice versa [10].

The drawback of applying linear schemes to control non-linear systems is that they can produce uneven performance throughout the dynamic range. With linear controller design, the various system constraints and requirements (like the maximum current and switching frequency or total harmonic distortion) cannot be directly incorporated [10].

Sliding mode control takes into account the switching characteristics of the power converter and offers robustness [11] during line and load variations, but it is a complex control algorithm [56].

Artificial intelligence techniques are used for applications where some parameters are unknown or where the system is undetermined; fuzzy logic is a suitable technique. Other advanced control schemes include neural networks and neuro-fuzzy control [10; 11].

Predictive control uses a model of the system to describe and predict the behaviour of the system according to its inputs. It applies optimisation criteria to select the actuation that will produce the most desirable outcome. With predictive control the cascaded structure, as found in linear schemes, can be avoided so as to produce very fast transient responses [11].

Deadbeat control uses the system model to determine the voltage that will eliminate the error in a single sampling interval, and applies this voltage by means of a modulator [11]. Model predictive control (MPC) evaluates its actuation options by means of a cost function consisting of the weighted control objectives. This method can be used to make predictions many time steps into the future so as to select a more optimal switching sequence, but this is also more demanding computationally [10].

2.3 Suitability of predictive control schemes

In Figure 2.3 the characteristics of power converters and the nature of control platforms that are presently available are set out to show their relation to predictive control approaches.

In order to improve the performance and efficiency of a system, its real nature and characteristics have to be taken into consideration. A power converter is a non-linear system comprising of both linear and non-linear components. A converter also comprises of a finite number of switches and switching states. The *on* and *off* transitions of each switch are commanded by discrete input signals. The system poses inherent restrictions, such as maximum output voltage, and requires protective restrictions, for the sake of its components and loads, such as current limitations [10].

Currently, it is the norm for control strategies to use discrete time steps and to be implemented on digital platforms. The models of converters are well known and can be used to adapt the controller to the system and its

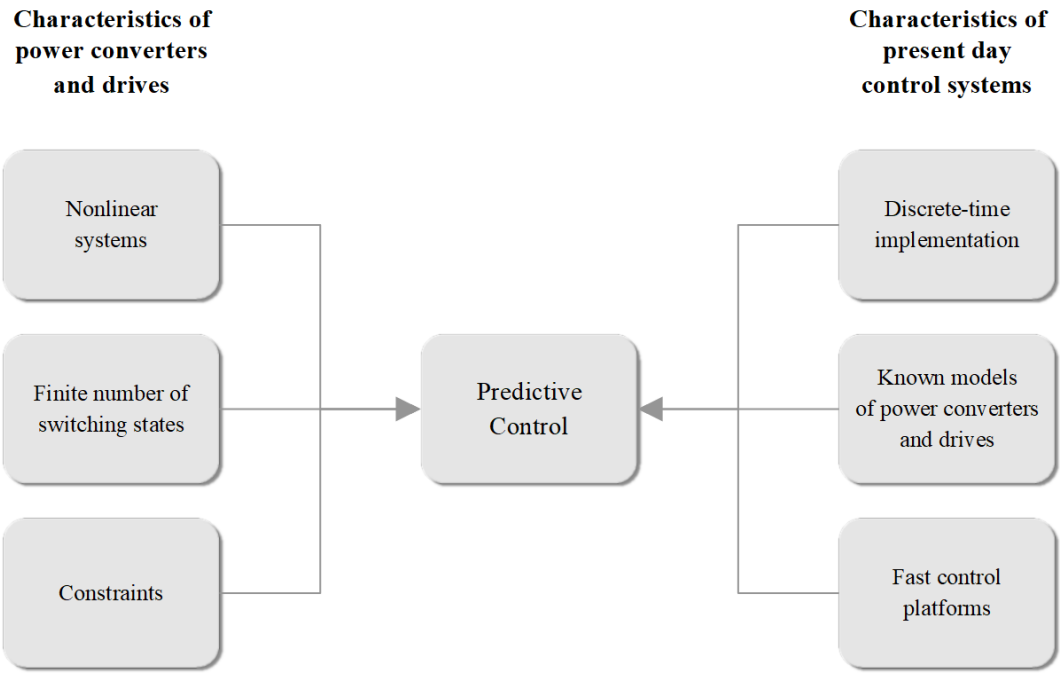

Figure 2.3: Characteristics of power converters, the nature of control platforms presently available and their relation to predictive control approaches. Amended from [10].

parameters. The computational abilities of control platforms have improved over the years, making computationally large and demanding algorithms more feasible today, such as MPC [10; 11].

In Figure 2.4 a breakdown is provided of the predictive control schemes used in power electronics. The dominant feature of predictive control is its use of a system model to predict the values of the controlled variables. Using this prediction it can determine the optimal actuation evaluated against the predefined optimisation criterion. The optimal actuation in deadbeat control is the option that eliminates the error within the next single sampling interval. The optimisation criterion for hysteresis-based predictive control requires the actuation to keep the controlled variable within the suitable hysteresis error boundary around the reference signal. Trajectory-based control has a predefined trajectory which the controlled variable is forced to track. The criteria involved for MPC are more flexible as they entail the minimisation of a cost function comprising of weighted control objectives. Of these types of predictive controllers, only deadbeat control and MPC (with the continuous control set) need modulators to produce the required voltage signal, resulting in a fixed switching frequency. The other methods generate the switching signals directly and their switching frequencies vary [11].

For predictive control non-linearities are easily included in the system model, eliminating the need to linearise it according to a specific operating

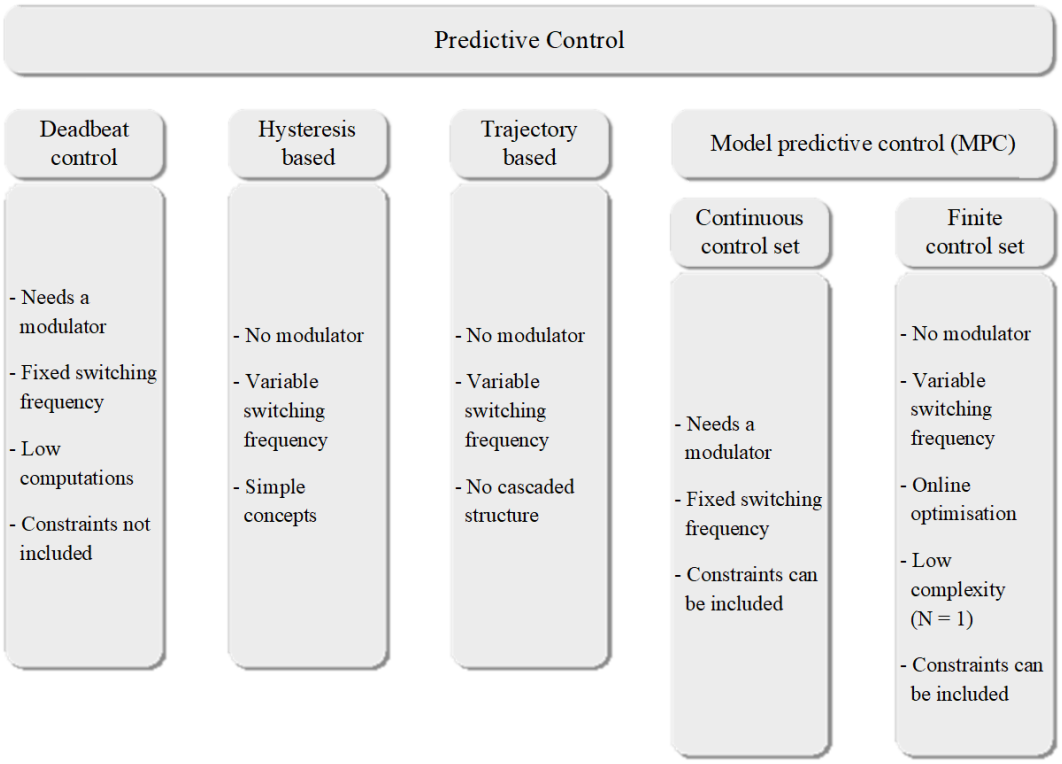

Figure 2.4: Classification of predictive control methods. Amended from [11].

point. This allows operation under any condition. Variable restrictions can also be included in the design. These advantages are easy to implement in some of the controller methods such as MPC, but very challenging in for instance deadbeat control [11].

2.4 Model predictive control

MPC is based on the following basic concepts [10]:

- A model is derived that describes the behaviour of the system. This model is then used to predict the system's behaviour over a predefined horison length (number of time steps) into the future.
- A cost function represents the control objectives, and assigns a weighting to each objective. The cost is used to evaluate and compare the suitability of future actuation options.
- The actuation sequence that minimises the cost function is selected as the optimal solution. Only the first actuation of the optimal sequence is applied, discarding the rest of the sequence. Hereafter the process is repeated in order to re-evaluate the state and performance of the system resulting from this actuation. In this sense the prediction horison is

shifted forward in time along with the control actions applied at each new time step. The controller thus never applies the rest of the sequence predicted during a specific time step. This concept is known as the receding horison principle.

The basic principles of MPC were developed in the 1960s and attracted interest from industry in the 1970s [57]. Thereafter MPC has been applied in the chemical and process industries. The time constants were sufficiently long for calculations to be completed. In the 1980s MPC was introduced in the power electronics industry in high-power applications with low switching frequencies [55]. The control algorithm needed long calculation times therefore applications with high switching frequencies were not possible at the time. As the technology regarding microprocessors rapidly developed, MPC started to receive more interest due to increased computational capabilities being available [10; 11]. MPC has several advantages to offer [10]:

- Multi-variable problems become simple.
- It allows compensation of dead time.
- The controller offers simple implementation for a wide variety of systems. There are many possibilities for adaptations and extensions to suit specific applications.
- Non-linearities are easily included in the system model, eliminating the need to linearise it according to a specific operating point. This allows operation under any conditions. Variable restrictions can also be included in the design. Aside from MPC, this advantage is very challenging to implement in other types of predictive controllers such as deadbeat control [11].

The disadvantages that come with MPC are [10]:

- The computational complexity involved in evaluating and selecting the optimal solution candidate increases exponentially as the prediction horison is lengthened further into the future. This can however be managed and mitigated by applying intelligent optimisation algorithms.
- The controller is dependent on the system's model. Therefore the quality of the model derived for the system will determine the quality of the controller and its performance [11]. If the system parameters change throughout time, an estimation or adaptation algorithm has to be incorporated.

2.5 Basic principles of model predictive control

An overview of basic principles on which a model predictive controller is based is provided in this section. This entails: deriving a mathematical model; understanding the finite control set; how predictions are made in terms of the prediction horison; evaluation of multiple possible solutions according to the control objectives by means of a cost function; the exhaustive search for an optimal solution; and optimising the search computationally by using a sphere decoding algorithm.

2.5.1 The state-space model

A linear system, like the one in Figure 2.5, can be described mathematically by means of a discrete-time state-space model:

$$\begin{aligned} \boldsymbol{x}(k+1) &= \boldsymbol{A}\boldsymbol{x}(k) + \boldsymbol{B}\boldsymbol{u}(k) \\ \boldsymbol{y}(k) &= \boldsymbol{C}\boldsymbol{x}(k) \end{aligned}$$

where k indicates the current position in the discrete time-line, and $k+1$ the next time step. The model contains the current state $\boldsymbol{x}(k)$ of the system, and predicts the future state values $\boldsymbol{x}(k+1)$ according to the switching actuation $\boldsymbol{u}(k)$ applied to it, as demonstrated in Figure 2.6. System states can include for instance, currents and voltages within the circuit. The output vector $\boldsymbol{y}(k)$ determines to which of these states the control is applied.

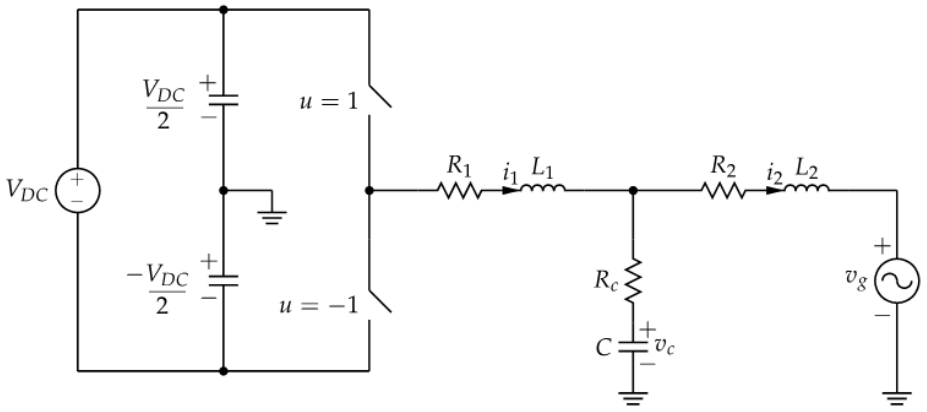

Figure 2.5: Example of a physical model of the system. A single-phase, two-level grid-tied converter with LCL-filter is used per illustration. From such a model a mathematical model is derived.

2.5.2 The finite control set (FCS) constraint

The use of switches poses certain constraints and therefore only a finite number of actuation options are available, also known as a finite control set.

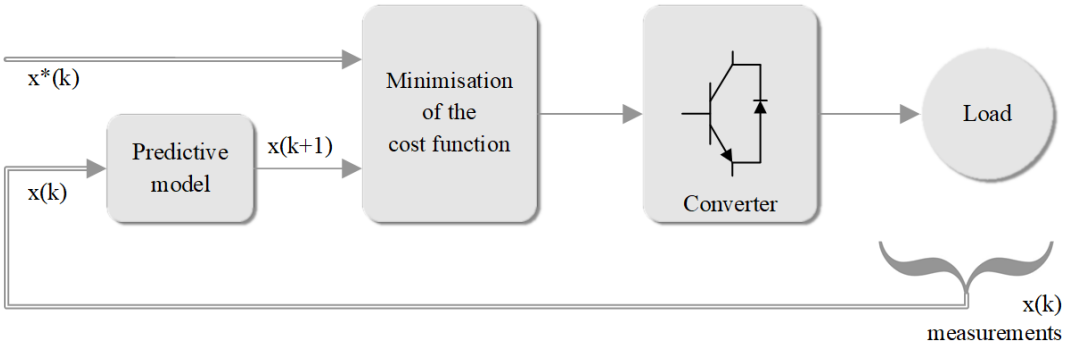

Figure 2.6: Diagram of how the MPC control scheme functions. Amended from [10].

For a two-level system the switches within the same phase leg are changed complementary of each other, so both cannot be on or off simultaneously, thus at any discrete instance in time , only one of the two switches is on. There are therefore two switch states in this case: $u = -1$ when only the bottom switch is on and $u = 1$ when only the top switch is on, as labelled in Figure 2.5.

2.5.3 The prediction horison

The controller makes predictions for a pre-defined horison length of N time steps into the future. The controller can directly manipulate the switch state $\boldsymbol{u}$ at every discrete position in time to best control the output sequence $\boldsymbol{Y} = [\ \boldsymbol{y}(k+1)\ \boldsymbol{y}(k+2)\ \ldots\ \boldsymbol{y}(k+N)\ ]^T$ to follow a reference $\boldsymbol{Y}^* = [\ \boldsymbol{y}^*(k+1)\ \ldots\ \boldsymbol{y}^*(k+N)\ ]^T$ of the desired system behaviour, as illustrated in Figures 2.7a and 2.7b. Of the N switch positions in the sequence selected as most optimal, $\boldsymbol{U}_{opt}$, only the first is applied, namely $\boldsymbol{u}(k)$. This principle where the rest of the switch states in the sequence, determined for each of the N time steps in the horison, is never applied but rather discarded and recalculated as the controller advances to the next time step to once again only implement the first one, is known as the *receding horison* principle. The controller will always predict a fixed number of steps ahead from its current point in time where the selected actuation is applied to the switches. In Figures 2.7a and 2.7b all possible current trajectories $\boldsymbol{Y}_1, \boldsymbol{Y}_2, \boldsymbol{Y}_3$ and $\boldsymbol{Y}_4$ are predicted for all the possible candidate switching sequences $\boldsymbol{U}_1, \boldsymbol{U}_2, \boldsymbol{U}_3$ and $\boldsymbol{U}_4$.

2.5.4 Cost function and control objectives

The cost function J evaluates each of the candidate switching sequences $\boldsymbol{U}(k) = [\ \boldsymbol{u}(k)\ \boldsymbol{u}(k+1)\ \ldots\ \boldsymbol{u}(k+N-1)\ ]^T$ over the horison of N time

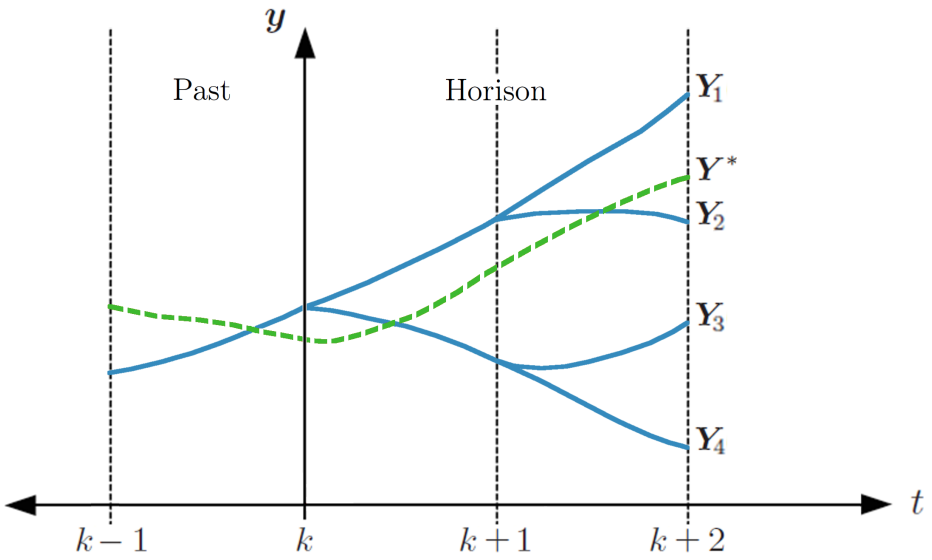

(a) Predicted current trajectories $\boldsymbol{Y}$ compared to the reference $\boldsymbol{Y}^*$.

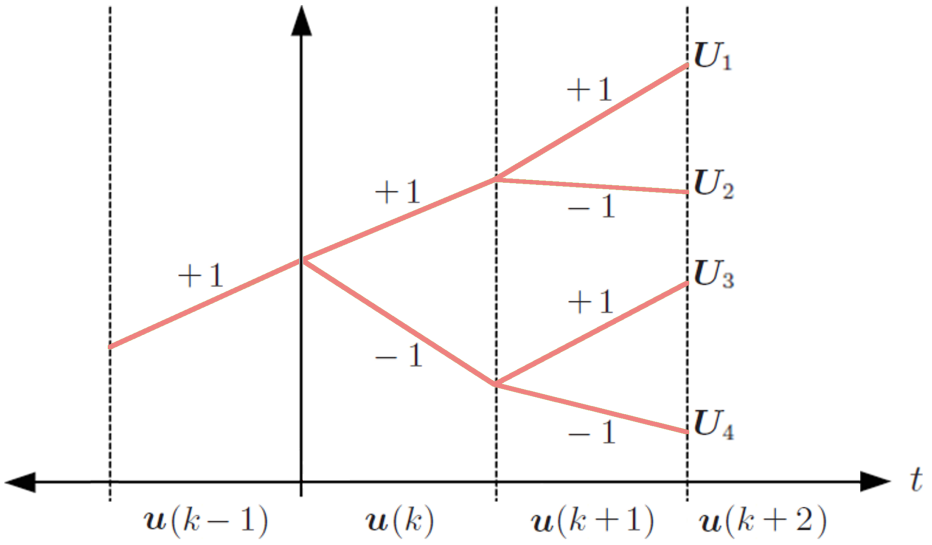

(b) Candidate switching sequences

Figure 2.7: Mapping of all the possible switching actions and their resulting current trajectories. Amended from [12].

steps into the future according to a combination of weighted control objective costs:

$$J = \sum_{\ell=k}^{k+N-1} \lambda_e J_e(\ell) + \lambda_u J_u(\ell) \quad \text{where} \quad \ell = k, \ldots, k+N-1.$$

For example, the first objective is to minimise the reference tracking error, penalised by the error cost J_e and prioritised by the weighting factor λ_e. The

second objective is to reduce the frequency of switching which is also treated according to its specific cost J_u and weighting λ_u.

Figure 2.8 provides an example of how the number of predicted solution sequences increases exponentially with longer prediction horisons in a three-level converter, having three possible switch states in its finite control set $u \in \{-1, 0, 1\}$. To evaluate each of these outcomes becomes an exhaustive search and is computationally challenging. Various optimised search strategies exist by which the computational complexity of the search can be reduced. This makes it easier to evaluate outcomes over longer prediction horisons into the future and therefore improve the overall system performance [58].

The optimal control sequence $\boldsymbol{U}_{opt}(k) = [\, \boldsymbol{u}(k)\ \boldsymbol{u}(k+1)\ \ldots\ \boldsymbol{u}(k+N-1)\,]^T$ is determined by solving the following problem [58]:

$$\boldsymbol{U}_{opt}(k) = \arg\min_{\boldsymbol{U}(k)}\ J$$

subject to predictive extension of the plant model:

$$\begin{aligned} \boldsymbol{x}(\ell+1) &= \boldsymbol{A}\boldsymbol{x}(\ell) + \boldsymbol{B}\boldsymbol{u}(\ell) \\ \boldsymbol{y}(\ell+1) &= \boldsymbol{C}\boldsymbol{x}(\ell), \end{aligned}$$

for $\ell = k, \ldots, k+N-1$. This problem is eventually rewritten as an integer least-squares (ILS) problem with $\boldsymbol{U}$ as the optimisation variable [58]:

$$\boldsymbol{U}_{opt}(k) = \arg\min_{\boldsymbol{U}(k)} \|\boldsymbol{H}\boldsymbol{U}(k) - \boldsymbol{H}\boldsymbol{U}_{unc}(k)\|_2^2 .$$

All of the 27 possible actuation vectors identified in Figure 2.8 for the three-level converter with horison $N = 3$, can be mapped in a N-dimensional discrete solution space according to their characteristics, as illustrated in Figure 2.9. The non-singular, upper triangular matrix $\boldsymbol{H}$ is referred to as the

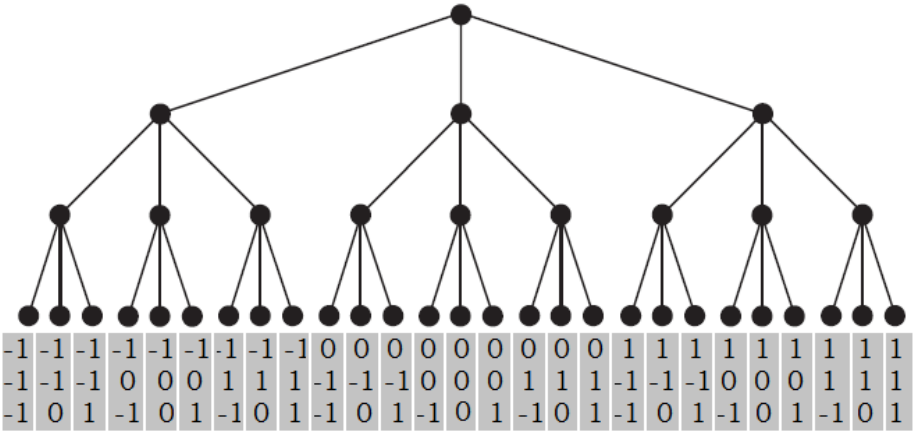

Figure 2.8: Exhaustive solution search tree of a three-level converter setup over a horison length of three steps into the future. Amended from [13].

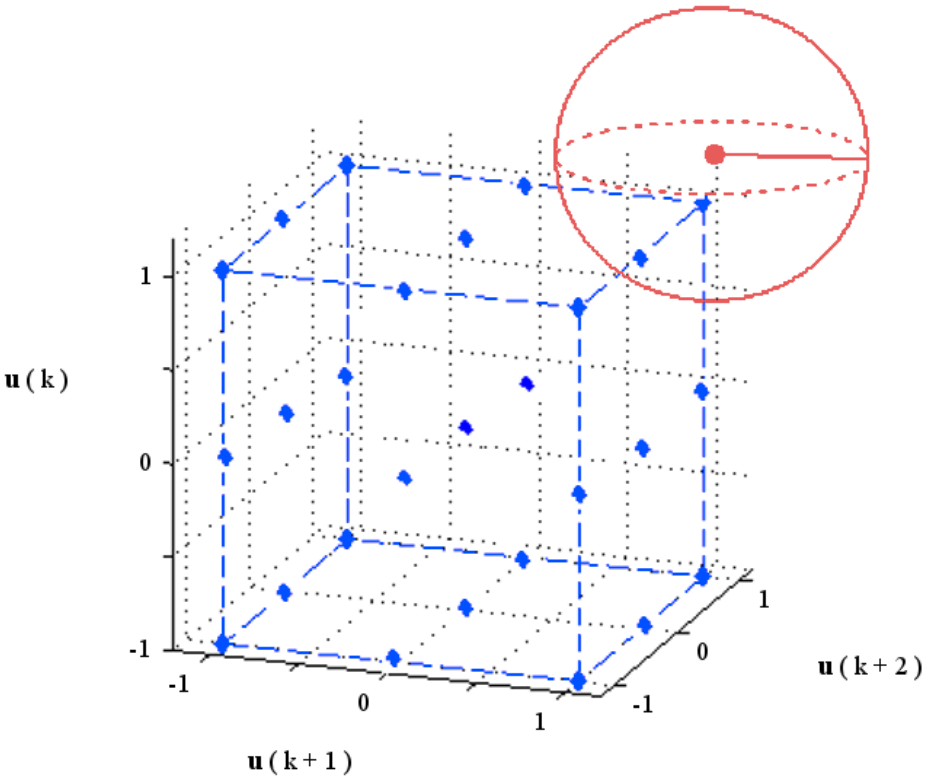

Figure 2.9: Solution space of a three-level converter, evaluated over a horison of $N = 3$ time steps, containing the 27 solution points of which two fall within the search sphere centred around the unconstrained solution.

transformation matrix or lattice generator matrix, as it is crucial to generating the discrete solution space [58].

In essence, the above-mentioned ILS problem takes the distance (Euclidean norm) between a candidate $\boldsymbol{U}(k)$ and the unconstrained solution $\boldsymbol{U}_{unc}(k)$, which is the most optimal actuation the system could offer in the case where the actuation voltage is not limited by the integer constraints incorporated by the switching setup. Traditionally, the distances regarding all 27 possible actuation vectors were investigated to identify the candidate $\boldsymbol{U}(k)$ that is the closest to the unconstrained optimum (and thus minimises the cost). This is known as the exhaustive search and becomes computationally intractable with longer horisons and increased system complexity [58].

2.5.5 Sphere decoding

To solve the ILS problem in a more efficient manner, the sphere decoding approach, adopted into power electronics from the communications field [59], is implemented to exclude as many sub-optimal solutions from the search as possible. The name of the sphere decoder is derived from the way the decoder compares the candidate solutions to the unconstrained optimum.

The unconstrained optimum serves as the midpoint of a hypersphere with a shrinking search radius, so as to narrow the search space to include the most favourable solutions and exclude as many sub-optimal solution options from the sphere as possible. The initial radius is determined by rounding the real values in the unconstrained optimum $\boldsymbol{U}_{unc}$ to the nearest integers, for instance $u \in \{-1, 0, 1\}$. The radius is reduced each time a candidate is found that is closer than the previously discovered, while those that lie outside the radius are automatically excluded from the search, pruning the branching of the search tree at early stages.

Figure 2.10 shows the approach by which the sphere decoder explores the search tree. The decoder starts at the origin of the tree and explores the branching options, starting with the left most branch and moving downward, prioritising middle and right branches for later. Therefore the left branch in the first level (which is representative of the first time step of the horison) is evaluated first. A node is evaluated to determine whether the solutions associated with it fall within the sphere or not. Those that comply with the criteria are open for further exploration, whereas a non-compliant node serves as a dead-end because it offers no improvement, and is pruned from the search tree. In Figure 2.10 the red nodes indicate the paths that fell outside the sphere during the search. The decoder then explores the next path alongside its current path, returning to previous nodes as it completes the evaluation of all three nodes in its current level. When the decoder reaches the bottom of the tree, these solutions represent a complete switching sequence for the specified horison. If such a node falls within the sphere, the sphere's radius is tightened to the current solution distance from the sphere's centre. This solution point is then recorded as a temporary optimum solution. After the decoder has completed its search, the last complete solution that was discovered as a better optimum is declared the official optimum solution.

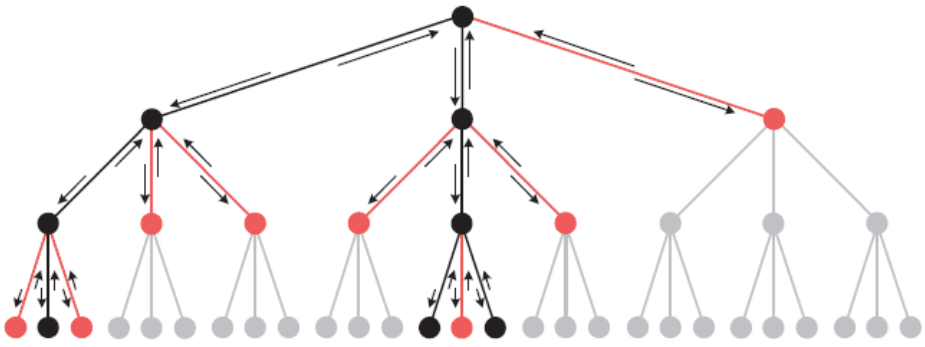

Figure 2.10: Pruning of the search tree for a three-level converter setup by means of the sphere decoding algorithm over a horison length of three time steps into the future [13].

2.6 Existing research

Model predictive control (MPC) provides a simplified way of handling non-linear dynamics, multiple inputs and outputs, as well as constraints for the inputs, states and outputs [60]. The MPC strategy is investigated as an alternative to traditional PWM modulation for grid-connected applications [61; 62; 63].

Inverters with pulse width modulation (PWM) modulators produce output voltages with significant harmonic content which need to be removed for grid-connected applications by means of a filter [64]. An LCL-filter is the most popular for this application as it offers better harmonic attenuation than the traditional series inductors and offers medium-voltage (MV) converters a reduction in switching frequencies while functioning within the acceptable harmonic limits [61]. The size, cost and filtering capacity trade-off of an L-filter becomes a limitation with increased power applications [65]. However, the LCL-filter capacitance causes a delay between the grid and converter making it difficult to perform control on grid-side quantities [47]. Active or passive damping can be used to perform damping. With passive damping, passive elements such as resistors are connected in series or parallel to the reactive elements in the LCL-filter [66]. This however is very costly in terms of the system's conduction losses and efficiency. For this reason active damping is preferred to passive damping and is based on closed-loop control [67]. Active damping is generally software-based relying on feedback of other control variables, acting as an additional damping term to suppress filter resonance, such as capacitor voltage, or current to the current control loop [65]. With active damping use is not made of physical components to perform damping, but additional sensors and circuitry could be incorporated which can result in increased system cost and complexity [65].

In [65] a control scheme is developed for a three-phase grid-connected converter with LCL-filter using a reduced order LCL-filter model by approximating it as an L-filter and adding an additional disturbance term to the state-space equation to represent the resonance of the LCL-filter. The controller design is a combination of state feedback and disturbance rejection (designed off-line) and MPC computed on-line. The control objectives are to perform fast reference-tracking response of active and reactive components and the damping of the LCL-filter resonance [65].

An unconstrained MPC approach is used in [64] to control the grid-side current of a single-phase grid-connected inverter with a space-vector PWM modulation stage and LCL-filter. Multiple resonant controllers are implemented into an augmented system model to provide disturbance rejection of the grid-voltage harmonics of the 3rd, 5th and 7th fundamental harmonics in order to effectively track the sinusoidal reference [64]. For validation by simulation the reference tracking accuracy was evaluated over a prediction horison of $N = 100$ time steps at a sampling frequency of 20 kHz, resulting

in a 5ms horison into the future, and only included the cost related to commutation over a control horison of 20 time steps [64]. The closed-loop system could perform current tracking with no steady-state error and a fast transient response of one 60 Hz cycle [64]. The grid-voltage harmonic rejection was tested by inserting disturbances into the grid voltage; the system is able to reject every disturbance with fast settling time [64]. The system proves that unconstrained MPC approaches provide good closed loop behaviour, however they do not address constraints in the system, such as a finite control set limiting the voltage values that can be applied at the ac-side output terminals of the converter, which poses a greater challenge in terms of efficient solving within one sampling period [64].

Many variations of MPC have been developed for power electronic applications, of which finite control set model predictive control (FCS-MPC) is among the most prominent [68; 60]. FCS-MPC handles the control task as an online optimisation problem where the responses to the possible switch-state options are predicted at every time step to effectively minimise the cost function [69]. The strategy is often only applied over a prediction horison length of one time step [68], but by using adequate optimisation techniques predictions can easily be performed over longer horisons [46; 70].

Different state feedback approaches of online optimised FCS-MPC are presented in [63] for a grid-tied three-phase two-level voltage-source converter (VSC) with LCL-filter. Converter-side current feedback, multi-variable control and direct line-side current control were compared. The approach most favourable for reducing switching frequency and current distortion is the line-side current control strategy in conjunction with long prediction horisons, which is also more demanding computationally and challenging to implement on control hardware, but can be managed by incorporating efficient algorithms [63].

Another MPC-based strategy that developed alongside FCS-MPC is model predictive direct torque control (MPDTC) as in [71; 72; 73; 74]. Its specific application is MV induction machine (IM) drives. It also directly manipulates the semi-conductor switches as with FCS-MPC. Model predictive direct current control (MPDCC) is an extension of MPDTC which directly regulates the stator currents of the IM [75; 76; 77].

In [61] a new MPDCC strategy is proposed for a MV neutral-point-clamped grid-connected converter with LCL-filter to address both the challenges of filter resonance damping and grid-voltage harmonic attenuation by means of the virtual resistor (VR) approach. The control strategy is thus referred to as MPDCC-VR. For filter resonance damping a resistor can be added in series or parallel to the filter capacitor. However, instead of inserting an actual passive damping resistor, a damping reference term is incorporated into the converter-side current reference. The VR-based references are predicted at each time step in conjunction with the state trajectories. Because the grid voltage harmonics are not similar to that in the capacitor voltage, the related

grid current harmonics can be attenuated by emulating a resistor in series with the grid-side inductor [61]. The study in [61] provided good steady-state performance even with grid-voltage distortion present. At the operating point it is able to surpass the performance of multi-loop control with space vector modulation [61].

A FCS-MPC strategy is presented by [14] that performs control on the active and reactive power injected into the grid from a three-phase three-level neutral-point-clamped (NPC) converter, as shown in Figure 2.11, with LCL-filter over a prediction horison of one time step. The cost function is formulated to include four control objectives. Firstly to provide the adequate active and reactive power to the grid by performing fundamental current tracking, secondly to reduce switching frequency, thirdly to maintain balance between the DC-link capacitor voltages and lastly to avoid excitation of the resonant frequencies of the LCL-filter [14]. These four objectives were incorporated into the cost function,

$$J = \lambda_{unb} J_{unb} + \lambda_{sw} J_{sw} + \lambda_{i_1} J_{i_1} + \lambda_{i_2} J_{i_2},$$

by summing the individual cost terms of each objective and assigning a relevant weighting factor λ to each. The cost related to unbalanced DC-link capacitor voltages, J_{unb}, is incorporated by predicting the future voltages of the DC-link capacitors and taking the square of their difference [14]. The switching cost J_{sw} is calculated by squaring the number of commutations that took place in the last fundamental period (20ms) [14]. The last two costs J_{i_1} and J_{i_2} are formulated around the performance of reference tracking and filter resonance damping in both the converter current $\boldsymbol{i}_1$ and grid-side current $\boldsymbol{i}_2$. The controller must try to avoid putting energy into the LCL-filter resonance frequencies. The first resonance relates to the parallel impedance between the grid-side inductor and the filter capacitor [14]. It can be expressed as

$$\omega_1 = \frac{1}{\sqrt{CL_2}}.$$

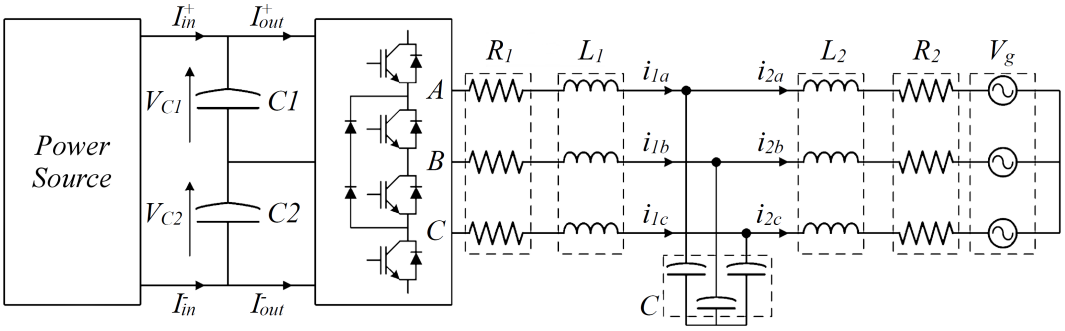

Figure 2.11: System topology used by [14]. Amended from [14].

The second resonance frequency is derived from the parallel connection of converter current L_1, filter capacitance C and grid-side inductance L_2:

$$\omega_2 = \frac{1}{\sqrt{C\dfrac{L_1 L_2}{L_1 + L_2}}}.$$

For the converter current, high gain around ω_1 is needed to incur a high cost for harmonic components close to that frequency. Distortion generated from the resonance in the converter current is penalised by means of a first-order band-pass filter tuned around ω_1 [14]. A stop-band filter is also needed at the fundamental frequency ω_f so that the controller prioritises placing energy there [14]. The cost related to the performance of the converter current can be expressed as

$$J_{i_1} = W_1(i_{1\alpha}^2 + i_{1\beta}^2)$$

where a digital filter W_1 performs the required filtering and the converter current, $\boldsymbol{i}_1 = [i_{1\alpha} \quad i_{1\beta}]^T$, is expressed in $\alpha\beta$-coordinates. For resonance damping at ω_2 a first-order pass-band filter is included in the cost J_{i_2} related to the grid-side current behaviour. To improve the grid-side current tracking a pass-band filter at the fundamental frequency is added to both the predicted current $\boldsymbol{i}_2(k+1)$ and the reference current $\boldsymbol{i}_2^*$. The cost related to the grid-side current behaviour is expressed as follows:

$$J_{i_2} = (W_2 i_{2\alpha}(k+1) - W_r i_{2\alpha}^*)^2 + \left(W_2 i_{2\beta}(k+1) - W_r i_{2\beta}^*\right)^2.$$

Figure 2.12 shows the frequency response of the digital filters W_1, W_2 and W_r. The same digital filter is used for both $\boldsymbol{i}_2$ and W_1, thus it can be seen that the filter for $\boldsymbol{i}_1$ in Figure 2.13 has peaks at both ω_1 and ω_2 but low cost at ω_f. Comparing the harmonics of the converter-side and grid-side currents to the corresponding filters applied to them as in Figures 2.13 and 2.14, it is observed that the controller avoided injecting harmonics at the frequencies associated with high cost.

The system in [14] was tested through MATLAB-Simulink simulations in which a 3 kV grid voltage and a 6 MW three-level NPC converter were considered. The THD of the NPC converter-side current was 13.49% and that of the grid-side current 3.74%, indicating the functioning of the LCL-filter. When the switching-cost weighting is set to $\lambda_{sw} = 0$, a switching frequency of about 2.5 kHz is obtained. By applying the switching cost, the switching frequency could be reduced to 1 kHz.

After reviewing the literature it is noted that it was a general occurrence that MPC controllers were mostly implemented with short horisons, such as only one time step long, in order to avoid an unmanageable computational burden. The availability of efficient solving algorithms makes it possible to simulate MPC controllers with long prediction horisons in order to draw upon the performance gain. Grid-side current control using a FCS MPC with

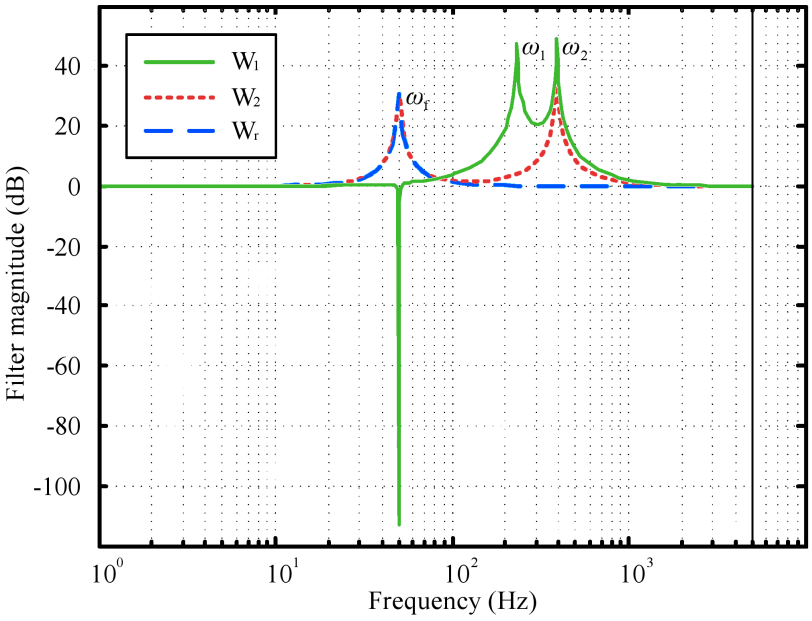

Figure 2.12: Frequency response of the digital filters W_1, W_2 and W_r. Amended from [14].

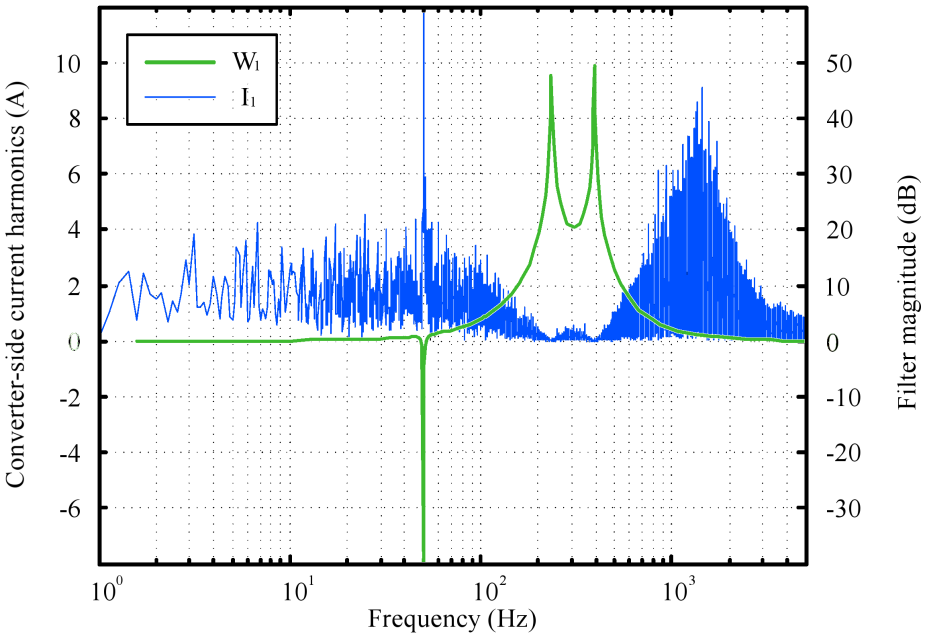

Figure 2.13: Spectrum of the converter-side current $\boldsymbol{i}_1$ compared to its filter. Amended from [14].

the long-horisons approach was found by [63] to be the most favourable for reducing switching frequency and current distortion. An LCL-filter will be used to remove harmonic content from the current injected into the grid. This filter is preferred above the traditional series inductors as it offers better

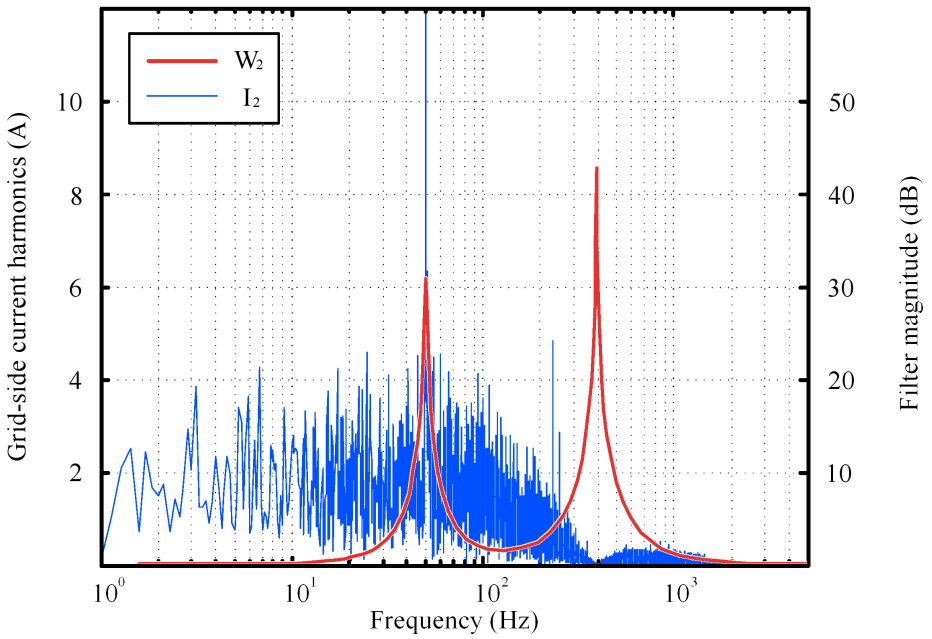

Figure 2.14: Spectrum of the grid-side current $\boldsymbol{i}_2$ compared to its filter. Amended from [14].

harmonic attenuation. Passive damping will not be considered as the power losses associated with it conflict with the efficiency aim of the MPC controller to be designed in this study. This study will include not only the grid-side current, but all the state variables in the controlled output vector to improve stability. Along with the ability of the long prediction horison to anticipate the reaction of the system to possible control sequences further into the future, the system is able to better distribute the switching energy to reduce resonance.

2.7 Summary

A brief overview of the main themes addressed within this chapter is provided in Figure 2.15. Background is given on power converters, predictive control methods and the advantages, drawbacks and basic principles of model predictive control (MPC). MPC provides a simplified way of handling non-linear dynamics, multiple variables and their related constraints. When applied over long horisons MPC can offer optimised control, but also brings a larger computational challenge along with it. Optimised search strategies such as the sphere decoder exist to solve the optimisation problem in a more computationally efficient way.

There is little existing literature on current control for a grid-connected converter with LCL-filter by means of finite control set MPC with long horisons. It is proposed that all state variables be controlled and that the grid voltage be incorporated into the state space model as an additional

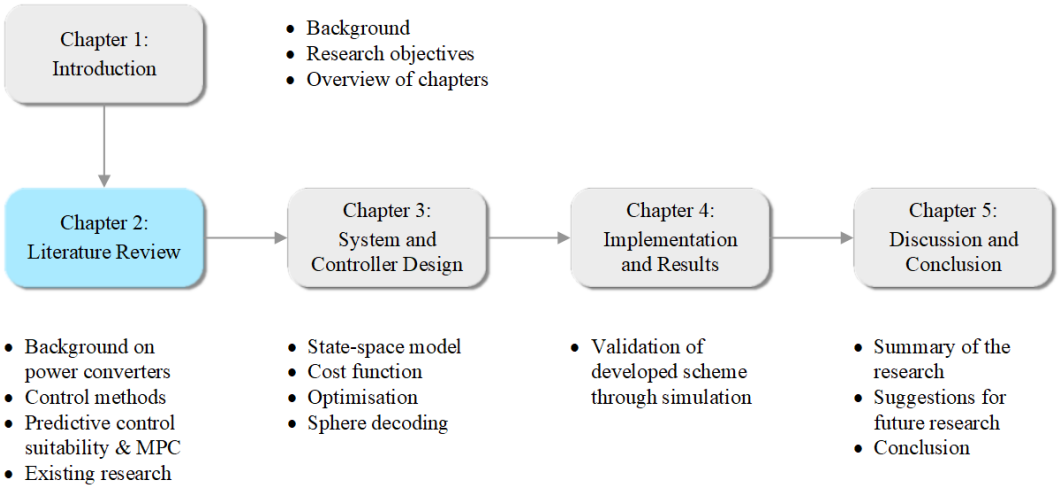

Figure 2.15: Brief overview of the thesis chapters.

input vector alongside the actuation-voltage vector. The aim with this study is to investigate the suitability of such a system to ensure the quality of the injected grid current, while also minimising power losses related to switching frequency.

Chapter 3

System and Controller Design

3.1 Introduction

A direct model predictive control (MPC) scheme is proposed for a three-phase two-level grid-connected converter with LCL-filter. The controller simultaneously controls the converter-side current, capacitor voltage and grid-side current by means of reference tracking. As a direct MPC controller it directly manipulates the switch-states of the converter. The control objectives are to minimise tracking error and switching losses. The control scheme is applied over long horisons and incorporates a sphere-decoding algorithm to overcome the computational effort that results from horisons longer than one. A mathematical model is derived and extends on previous work done by incorporating the grid-voltage into the model.

3.2 System Topology

The three-phase system of the grid-connected converter with LCL-filter is presented in Figure 3.1. The half-bridge converter has a DC-link voltage V_D that is assumed to stay constant. The semiconductor switches in each phase are only allowed to have one of either the top or bottom switches closed at a time, and are set directly by the controller. The LCL-filter consists of converter-side and grid-side inductors, L_1 and L_2, with internal resistances R_1 and R_2 respectively, and the filter capacitors C and capacitor resistances R_c that are connected in a star configuration. The LCL-filter filters the harmonics caused by the converter before they are injected into the grid. It is assumed that the amplitude and phase of the grid voltage remains constant for the model.

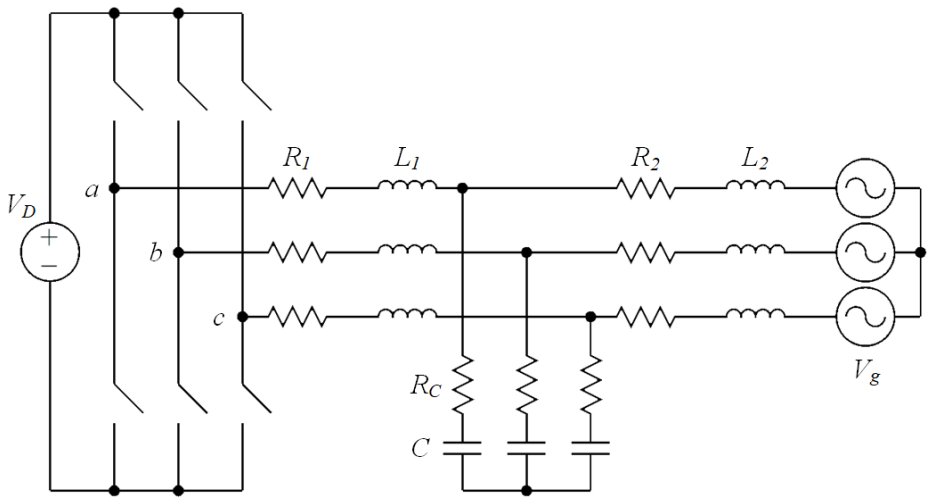

Figure 3.1: Three-phase grid-connected converter with LCL-filter.

3.3 Constraints

It is assumed that the switching components of the system are ideal. At any given time instance, each phase leg of the system may only assume one of two possible switch states contained in the finite control set:

$$u_a,\ u_b,\ u_c \in \{-1, 1\}, \tag{3.3.1}$$

where $u = -1$ represents closing the bottom switch and $u = 1$ closing the top switch. The voltage supplied to the filter by the converter can thus be expressed as $v_i = \frac{V_D}{2}u$, as in Figure 3.2.

3.4 Reference frames

Three-phase quantities can be transformed from the three-phase abc reference frame $\boldsymbol{\xi}_{abc} = [\xi_a\ \xi_b\ \xi_c]^T$ to the stationary orthogonal $\alpha\beta$ reference frame $\boldsymbol{\xi}_{\alpha\beta} = [\xi_\alpha\ \xi_\beta]^T$ by multiplication with the transformation matrix $\boldsymbol{K}_{\alpha\beta}$ [47]:

$$\boldsymbol{\xi}_{\alpha\beta} = \boldsymbol{K}_{\alpha\beta}\boldsymbol{\xi}_{abc}$$

$$\boldsymbol{K}_{\alpha\beta} = \frac{2}{3}\begin{bmatrix} 1 & -\frac{1}{2} & -\frac{1}{2} \\ 0 & \frac{\sqrt{3}}{2} & -\frac{\sqrt{3}}{2} \end{bmatrix}$$

In order to convert quantities from the $\alpha\beta$ reference frame back to the three-phase reference frame the following transformation can be used:

$$\boldsymbol{\xi}_{abc} = \boldsymbol{K}_{abc}\boldsymbol{\xi}_{\alpha\beta}$$

$$\boldsymbol{K}_{abc} = \frac{3}{2}\begin{bmatrix} \frac{2}{3} & 0 \\ -\frac{1}{3} & \frac{\sqrt{3}}{3} \\ -\frac{1}{3} & -\frac{\sqrt{3}}{3} \end{bmatrix}$$

3.5 State-space model

In order to capture the dynamics of the system, comprising of the converter, filter and grid, a model thereof is needed. Figure 3.2 provides a simple look at the filter as it is connected in the system by looking at its per-phase model.

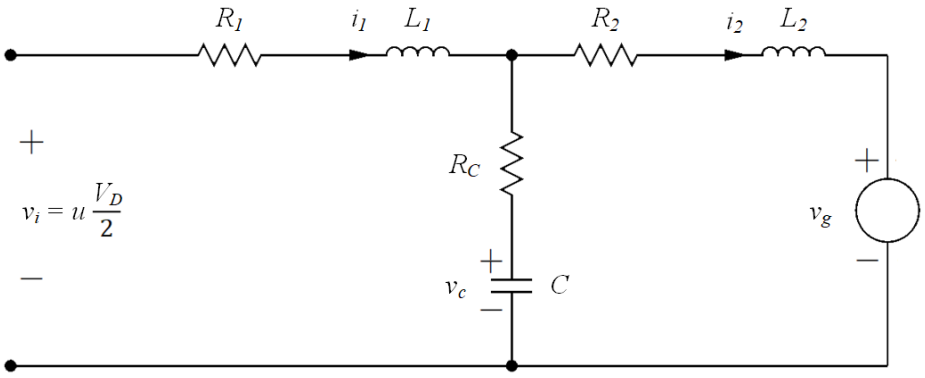

Figure 3.2: Per-phase model of the LCL-filter.

It is most convenient to describe the state of the system with i_1, i_2 and v_c as the state variables. Kirchoff's Voltage Law (KVL) is applied to the per-phase model in Figure 3.2 to obtain the following equations in the continuous-time domain:

$$\begin{aligned} 0 &= -u\left(\frac{V_D}{2}\right) + i_1 R_1 + L_1\left(\frac{di_1}{dt}\right) + (i_1 - i_2)R_c + v_c \\ 0 &= -v_c - (i_1 - i_2)R_c + i_2 R_2 + L_2\left(\frac{di_2}{dt}\right) + v_g \\ i_1 - i_2 &= C\left(\frac{dv_c}{dt}\right) \end{aligned}$$

These equations are rewritten to expose the terms that make up the state-space model:

$$\begin{aligned} \frac{di_1}{dt} &= -\left(\frac{R_c + R_1}{L_1}\right) i_1 + \left(\frac{R_c}{L_1}\right) i_2 - \left(\frac{1}{L_1}\right) v_c + \left(\frac{V_D}{2L_1}\right) u \\ \frac{di_2}{dt} &= \left(\frac{R_c}{L_2}\right) i_1 - \left(\frac{R_c + R_2}{L_2}\right) i_2 + \left(\frac{1}{L_2}\right) v_c - \left(\frac{1}{L_2}\right) v_g \\ \frac{dv_c}{dt} &= \left(\frac{1}{C}\right) i_1 - \left(\frac{1}{C}\right) i_2 \end{aligned}$$

The state vector $\boldsymbol{x}(t)$ contains the converter-side current $\boldsymbol{i}_1(t) = [i_{1\alpha}\ i_{1\beta}]^T$, the grid-side current $\boldsymbol{i}_2(t) = [i_{2\alpha}\ i_{2\beta}]^T$ and the capacitor voltage

$\boldsymbol{v}_c(t) = [v_{c\alpha}\ v_{c\beta}]^T$ as the state variables in the stationary $\alpha\beta$ reference frame:

$$\boldsymbol{x}(t) = [i_{1\alpha}\ i_{1\beta}\ \ i_{2\alpha}\ i_{2\beta}\ \ v_{c\alpha}\ v_{c\beta}]^T$$

The controller provides the three-phase switch states that serve as an input vector:

$$\boldsymbol{u}(t) = [u_a\ u_b\ u_c]^T$$

The grid voltage also serves as another input vector:

$$\boldsymbol{v_g}(t) = [v_{g_a}\ v_{g_b}\ v_{g_c}]^T$$

The continuous-time state-space model is derived from the KVL equations:

$$\begin{aligned} \frac{d\boldsymbol{x}(t)}{dt} &= \boldsymbol{F}\boldsymbol{x}(t) + \boldsymbol{G}\boldsymbol{u}(t) + \boldsymbol{P}\boldsymbol{v_g}(t) \\ \boldsymbol{y}(t) &= \boldsymbol{C}\boldsymbol{x}(t), \end{aligned} \tag{3.5.1}$$

where

$$\boldsymbol{F} = \begin{bmatrix} \frac{R_c+R_1}{-L_1} & 0 & \frac{R_c}{L_1} & 0 & \frac{1}{-L_1} & 0 \\ 0 & \frac{R_c+R_1}{-L_1} & 0 & \frac{R_c}{L_1} & 0 & \frac{1}{-L_1} \\ \frac{R_c}{L_2} & 0 & \frac{R_c+R_2}{-L_2} & 0 & \frac{1}{L_2} & 0 \\ 0 & \frac{R_c}{L_2} & 0 & \frac{R_c+R_2}{-L_2} & 0 & \frac{1}{L_2} \\ \frac{1}{C} & 0 & \frac{1}{-C} & 0 & 0 & 0 \\ 0 & \frac{1}{C} & 0 & \frac{1}{-C} & 0 & 0 \end{bmatrix}$$

$$\boldsymbol{G} = \begin{bmatrix} \frac{V_D}{2L_1} & 0 \\ 0 & \frac{V_D}{2L_1} \\ 0 & 0 \\ 0 & 0 \\ 0 & 0 \\ 0 & 0 \end{bmatrix} \boldsymbol{K}_{\alpha\beta} \qquad \boldsymbol{P} = \begin{bmatrix} 0 & 0 \\ 0 & 0 \\ \frac{1}{-L_2} & 0 \\ 0 & \frac{1}{-L_2} \\ 0 & 0 \\ 0 & 0 \end{bmatrix} \boldsymbol{K}_{\alpha\beta}$$

$$\boldsymbol{C} = \begin{bmatrix} \lambda_1 & 0 & 0 & 0 & 0 & 0 \\ 0 & \lambda_1 & 0 & 0 & 0 & 0 \\ 0 & 0 & \lambda_2 & 0 & 0 & 0 \\ 0 & 0 & 0 & \lambda_2 & 0 & 0 \\ 0 & 0 & 0 & 0 & \lambda_3 & 0 \\ 0 & 0 & 0 & 0 & 0 & \lambda_3 \end{bmatrix}$$

In the state-space output equation, $\boldsymbol{y}(t) = \boldsymbol{C}\boldsymbol{x}(t)$, the state variables that need to be controlled are selected and assigned the constant weighting factors contained in the $\boldsymbol{C}$ matrix. The weighting factors provide the option of customised control priorities of the selected variables. In the output vector, $\boldsymbol{y} = [\ \lambda_1\boldsymbol{i}_{1\alpha\beta}\ \ \lambda_2\boldsymbol{i}_{2\alpha\beta}\ \ \lambda_3\boldsymbol{v}_{C\alpha\beta}\ ]^T$, all three of the state variables are controlled simultaneously, as this improves the transient response, and stabilises control over short horisons.

This state-space model differs from those used in [46] as it contains an additional term, $\boldsymbol{P}\boldsymbol{v_g}(t)$, to incorporate the presence of the grid into the model. Both the input vectors $\boldsymbol{u}$ and $\boldsymbol{v_g}$ are in the *abc* reference frame and are transformed to the $\alpha\beta$ reference frame within the state space model by multiplication with $\boldsymbol{K}_{\alpha\beta}$ included in the input matrices $\boldsymbol{G}$ and $\boldsymbol{P}$.

The continuous-time model is discretised in order to obtain a discrete-time model. Time is divided into fixed sampling intervals of length T_s, and k denotes the current position in time such that $t = kT_s,\ k \in \mathbb{N}$. At each time instance k, each phase leg of the system may only assume one of two possible switch states contained in the finite control set $u_a,\ u_b,\ u_c \in \{-1, 1\}$ and $\boldsymbol{u}(t) = \boldsymbol{u}(k)$ remains constant during each interval. Du Hamel's formula [78] is applied to integrate the continuous-time state-space equations from $t = kT_s$ to $t = (k+1)T_s$ to obtain the discrete-time representation:

$$\begin{aligned} \boldsymbol{x}(k+1) &= \boldsymbol{A}\boldsymbol{x}(k) + \boldsymbol{B}\boldsymbol{u}(k) + \boldsymbol{T}\boldsymbol{v_g}(k) \\ \boldsymbol{y}(k) &= \boldsymbol{C}\boldsymbol{x}(k), \end{aligned} \tag{3.5.2}$$

where

$$\begin{aligned} \boldsymbol{A} &= e^{\boldsymbol{F}T_s} \\ \boldsymbol{B} &= -\boldsymbol{F}^{-1}(\mathbf{I} - \boldsymbol{A})\boldsymbol{G} \\ \boldsymbol{T} &= -\boldsymbol{F}^{-1}(\mathbf{I} - \boldsymbol{A})\boldsymbol{P} \end{aligned}$$

The model is evaluated at each time instant k to determine the state $\boldsymbol{x}$ in the next time-step $k+1$ which is a result of the applied switch state $\boldsymbol{u}(k)$.

3.6 Cost function

The discrete-time state-space model predicts the outcome of the system output $\boldsymbol{y}$ for each possible switch state input $\boldsymbol{u}(k)$. These outcomes are evaluated by a cost function:

$$J = \sum_{\ell=k}^{k+N-1} ||\boldsymbol{y}_e(\ell+1)||_2^2 + \lambda_u \, ||\Delta\boldsymbol{u}(\ell)||_2^2 \tag{3.6.1}$$

consisting of two control objectives. This cost function calculates the cost J associated with a certain choice of switching sequence and is also generally known as the objective function. The cost always has a non-negative scalar value. The first part of the cost function implements the objective to minimise the tracking error, $\boldsymbol{y}_e(\ell+1) = \boldsymbol{y}^*(\ell+1) - \boldsymbol{y}(\ell+1)$, by penalising deviation of the predicted outcomes $\boldsymbol{y}$ from their references $\boldsymbol{y}^*$. All three of the state variables $\boldsymbol{i}_1, \boldsymbol{i}_2$ and $\boldsymbol{v}_c$ are being controlled. The reference for the grid-side current $\boldsymbol{i}_2$ is known, but the references for the other variables are calculated

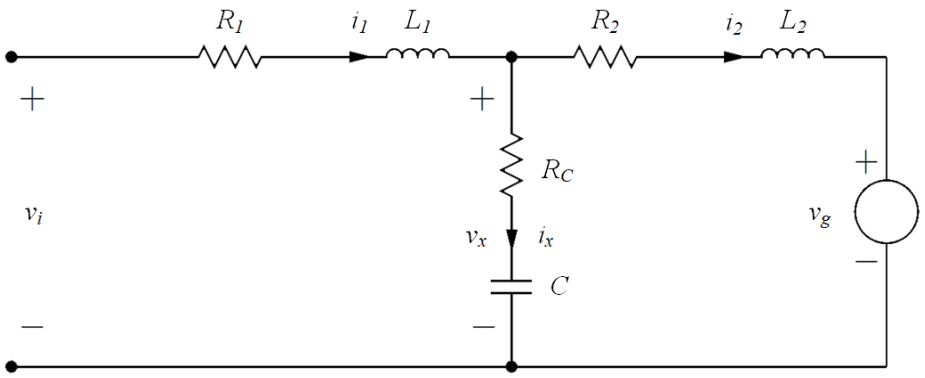

Figure 3.3: Per-phase model of the LCL-filter.

by deriving their phasors from the grid-side current reference:

$$\begin{aligned}\tilde{V}_x &= \tilde{V}_g + \tilde{I}_{2,ref}\,(R_2 + sL_2)\\ \tilde{V}_c &= \frac{\tilde{V}_x}{1 + sCR_c}\\ \tilde{I}_1 &= \tilde{I}_{2,ref} + \frac{\tilde{V}_c}{sC}\,,\end{aligned}$$

where $s = j\omega$, $\omega = 2\pi f$ and v_x is indicated in the per-phase model in Figure 3.3. The phasor magnitudes serve as the reference amplitudes:

$$\begin{aligned}I_{c,ref} &= |\tilde{I}_1|\\ V_{c,ref} &= |\tilde{V}_c|,\end{aligned}$$

and the phasor angles provide the reference angles relative to the phase of the grid-side current reference:

$$\begin{aligned}\phi_1 &= \angle\tilde{I}_1\\ \phi_c &= \angle\tilde{V}_c\end{aligned}$$

The reference signals for the controlled variables can be expressed as:

$$\begin{aligned}i_{1,ref}(t) &= I_{1,ref}\sin(2\pi ft + \phi_1)\\ i_{2,ref}(t) &= I_{2,ref}\sin(2\pi ft)\\ v_{c,ref}(t) &= V_{c,ref}\sin(2\pi ft + \phi_c)\end{aligned}$$

In the cost function, $J = \sum_{\ell=k}^{k+N-1} ||\boldsymbol{y}_e(\ell+1)||_2^2 + \lambda_u\,||\Delta\boldsymbol{u}(\ell)||_2^2$, the second part represents the objective to lower switching losses by minimising the switching frequency. The switching effort is defined as $\Delta\boldsymbol{u}(\ell) = \boldsymbol{u}(\ell) - \boldsymbol{u}(\ell-1)$, such that each change in switch-state will result in increased cost. The cost

function penalises the tracking error and switching effort by adding the squared Euclidean norm of each vector:

$$||\Delta \boldsymbol{u}(\ell)||_2 \quad = \quad \sqrt{\Delta u_a^2(\ell) + \Delta u_b^2(\ell) + \Delta u_c^2(\ell)}$$

A non-negative scalar weighting factor λ_u is applied to control the trade-off between the two control objectives. The length of the prediction horison N represents the finite number of discrete time steps into the future over which the outcomes are predicted and evaluated by the cost function [46].

3.7 Optimisation approach

At the current discrete position in time, k, the output reference tracking and switching effort is evaluated by the cost function for N steps into the future, in other words from time step $k+1$ to $k+N$. The switching sequence that has to be determined for the finite number of horisons into the future is contained in $\boldsymbol{U}(k)$ and must be compiled in such a way that it minimises the cost function. $\boldsymbol{Y}(k)$ represents the predicted output sequence, as a result of a candidate switching sequence. The reference for the output sequence is denoted as $\boldsymbol{Y}^*(k)$. Figure 3.4 offers a simple example of how the output sequence tracks its reference as the switch state is manipulated.

$$\boldsymbol{U}(k) = \begin{bmatrix} \boldsymbol{u}(k) \\ \boldsymbol{u}(k+1) \\ \vdots \\ \boldsymbol{u}(k+N-1) \end{bmatrix} \qquad \boldsymbol{Y}(k) = \begin{bmatrix} \boldsymbol{y}(k+1) \\ \boldsymbol{y}(k+2) \\ \vdots \\ \boldsymbol{y}(k+N) \end{bmatrix}.$$

The optimisation problem can be expressed as:

$$\boldsymbol{U}_{opt}(k) = \arg\min_{\boldsymbol{U}(k)} \; J$$

where the optimal switching sequence $\boldsymbol{U}_{opt}(k)$ is obtained by selecting the candidate solution sequence $\boldsymbol{U}(k)$, which results in the minimum cost. The cost function is dependent on the current state $\boldsymbol{x}(k)$ of the system, the previously chosen and applied switch state $\boldsymbol{u}(k-1)$, the reference $\boldsymbol{Y}^*(k)$ for the output sequence $\boldsymbol{Y}(k)$ and finally a candidate switching sequence $\boldsymbol{U}(k)$ requiring cost evaluation.

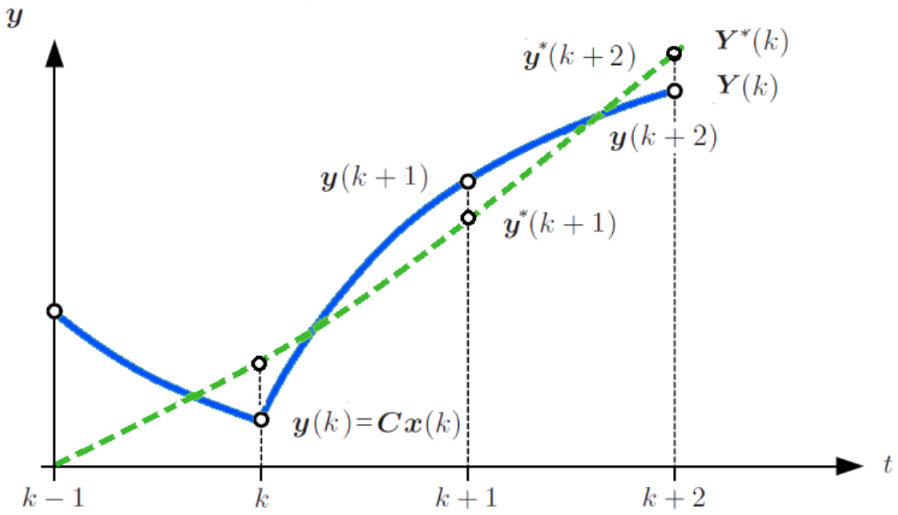

(a) Reference and predicted output

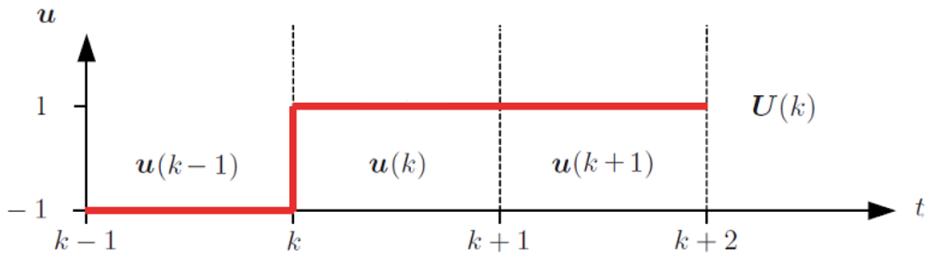

(b) Switching sequence

Figure 3.4: Reference tracking and evolution of the output $\boldsymbol{y}$ as a function of the input switching sequence for a horison of $N = 2$. Amended from [12].

The state equation is applied successively over the prediction horison:

$$
\begin{aligned}
\boldsymbol{x}(k+1) &= \boldsymbol{A}\boldsymbol{x}(k) + \boldsymbol{B}\boldsymbol{u}(k) + \boldsymbol{T}\boldsymbol{v_g}(k) \\
\boldsymbol{x}(k+2) &= \boldsymbol{A}\boldsymbol{x}(k+1) + \boldsymbol{B}\boldsymbol{u}(k+1) + \boldsymbol{T}\boldsymbol{v_g}(k+1) \\
&= \boldsymbol{A}^2\boldsymbol{x}(k) + \boldsymbol{A}\boldsymbol{B}\boldsymbol{u}(k) + \boldsymbol{A}\boldsymbol{T}\boldsymbol{v_g}(k) + \boldsymbol{B}\boldsymbol{u}(k+1) + \boldsymbol{T}\boldsymbol{v_g}(k+1) \\
\boldsymbol{x}(k+3) &= \boldsymbol{A}^3\boldsymbol{x}(k) + \boldsymbol{A}^2\boldsymbol{B}\boldsymbol{u}(k) + \boldsymbol{A}\boldsymbol{B}\boldsymbol{u}(k+1) + \boldsymbol{B}(\boldsymbol{u}(k+2)) \\
&\quad + \boldsymbol{A}^2\boldsymbol{T}\boldsymbol{v_g}(k) + \boldsymbol{A}\boldsymbol{T}\boldsymbol{v_g}(k+1) + \boldsymbol{T}(\boldsymbol{v_g}(k+2)) \\
&\vdots \\
\boldsymbol{x}(k+N) &= \boldsymbol{A}^N\boldsymbol{x}(k) + \boldsymbol{A}^{N-1}\boldsymbol{B}\boldsymbol{u}(k) + \cdots + \boldsymbol{A}^0\boldsymbol{u}(k+N-1) \\
&\quad + \boldsymbol{A}^{N-1}\boldsymbol{T}\boldsymbol{v_g}(k) + \boldsymbol{A}^{N-2}\boldsymbol{T}\boldsymbol{v_g}(k+1) + \cdots + \boldsymbol{A}^0\boldsymbol{v_g}(k+N-1)
\end{aligned}
$$

From this the general expression for the state of the system is deduced:

$$\begin{aligned} \boldsymbol{x}(k+m) &= \boldsymbol{A}^m\boldsymbol{x}(k) + \sum_{\ell=0}^{m-1} \boldsymbol{A}^{m-1-\ell}\boldsymbol{B}\boldsymbol{u}(k+\ell) \\ &\quad + \sum_{\ell=0}^{m-1} \boldsymbol{A}^{m-1-\ell}\boldsymbol{T}\boldsymbol{v}_{\boldsymbol{g}}(k+\ell), \\ \text{therefore} \quad \boldsymbol{y}(k+m) &= \boldsymbol{C}\boldsymbol{x}(k+m) \\ &= \boldsymbol{C}\boldsymbol{A}^m\boldsymbol{x}(k) + \sum_{\ell=0}^{m-1} \boldsymbol{C}\boldsymbol{A}^{m-1-\ell}\boldsymbol{B}\boldsymbol{u}(k+\ell) \\ &\quad + \sum_{\ell=0}^{m-1} \boldsymbol{C}\boldsymbol{A}^{m-1-\ell}\boldsymbol{T}\boldsymbol{v}_{\boldsymbol{g}}(k+\ell) \end{aligned}$$

$$\text{for } m = 1, \ldots, N.$$

The output sequence $\boldsymbol{Y}(k) = [\boldsymbol{y}(k+1) \ \ldots \ \boldsymbol{y}(k+N)]^T$ is rewritten in matrix notation as:

$$\boldsymbol{Y}(k) = \boldsymbol{\Gamma}\boldsymbol{x}(k) + \boldsymbol{\Upsilon}\boldsymbol{U}(k) + \boldsymbol{\Psi}\boldsymbol{V}_{\boldsymbol{g}}(k),$$

$\boldsymbol{\Psi}\boldsymbol{V}_{\boldsymbol{g}}(k)$ being an extension with regards to the equation from [46], where:

$$\begin{aligned} \boldsymbol{\Gamma} &= \begin{bmatrix} \boldsymbol{C}\boldsymbol{A} & \boldsymbol{C}\boldsymbol{A}^2 & \boldsymbol{C}\boldsymbol{A}^3 & \ldots & \boldsymbol{C}\boldsymbol{A}^N \end{bmatrix}^T, \\ \boldsymbol{\Upsilon} &= \begin{bmatrix} \boldsymbol{C}\boldsymbol{B} & \boldsymbol{0} & \cdots & \boldsymbol{0} \\ \boldsymbol{C}\boldsymbol{A}\boldsymbol{B} & \boldsymbol{C}\boldsymbol{B} & \cdots & \boldsymbol{0} \\ \vdots & \vdots & & \vdots \\ \boldsymbol{C}\boldsymbol{A}^{N-1}\boldsymbol{B} & \boldsymbol{C}\boldsymbol{A}^{N-2}\boldsymbol{B} & \cdots & \boldsymbol{C}\boldsymbol{B} \end{bmatrix} \end{aligned}$$

and therefore $\boldsymbol{\Psi}$ can be derived in a similar manner as:

$$\boldsymbol{\Psi} = \begin{bmatrix} \boldsymbol{C}\boldsymbol{T} & \boldsymbol{0} & \cdots & \boldsymbol{0} \\ \boldsymbol{C}\boldsymbol{A}\boldsymbol{T} & \boldsymbol{C}\boldsymbol{T} & \cdots & \boldsymbol{0} \\ \vdots & \vdots & & \vdots \\ \boldsymbol{C}\boldsymbol{A}^{N-1}\boldsymbol{T} & \boldsymbol{C}\boldsymbol{A}^{N-2}\boldsymbol{T} & \cdots & \boldsymbol{C}\boldsymbol{T} \end{bmatrix}.$$

Each of the zero matrices have the same number of rows as the $\boldsymbol{C}$ matrix and columns as the $\boldsymbol{B}$ matrix. Incorporating this dynamic evolution of the model into the cost function produces:

$$J = \|\boldsymbol{\Gamma}\boldsymbol{x}(k) + \boldsymbol{\Upsilon}\boldsymbol{U}(k) + \boldsymbol{\Psi}\boldsymbol{V}_{\boldsymbol{g}}(k) - \boldsymbol{Y}^{\star}(k)\|_2^2 + \lambda_u \|\boldsymbol{S}\boldsymbol{U}(k) - \boldsymbol{E}\boldsymbol{u}(k-1)\|_2^2,$$

where the first part penalises reference tracking error and the second part the switching frequency. This cost function is then sectioned into these two

parts, J_A and J_B, to make the matrix multiplication and simplification more manageable:

$$\begin{aligned}
J &= \|\boldsymbol{\Gamma x}(k) + \boldsymbol{\Upsilon U}(k) + \boldsymbol{\Psi V_g}(k) - \boldsymbol{Y}^\star(k)\|_2^2 + \lambda_u \|\boldsymbol{SU}(k) - \boldsymbol{Eu}(k-1)\|_2^2 \\
&= J_A + J_B,
\end{aligned}$$

$$\begin{aligned}
J_A &= \|\boldsymbol{\Gamma x}(k) + \boldsymbol{\Upsilon U}(k) + \boldsymbol{\Psi V_g}(k) - \boldsymbol{Y}^\star(k)\|_2^2 \\
&= [\boldsymbol{\Gamma x}(k) + \boldsymbol{\Upsilon U}(k) + \boldsymbol{\Psi V_g}(k) - \boldsymbol{Y}^\star(k)]^T [\boldsymbol{\Gamma x}(k) + \boldsymbol{\Upsilon U}(k) + \boldsymbol{\Psi V_g}(k) - \boldsymbol{Y}^\star(k)] \\
&= [\boldsymbol{\Gamma x}(k) + \boldsymbol{\Upsilon U}(k) - \boldsymbol{Y}^\star(k)]^T [\boldsymbol{\Gamma x}(k) + \boldsymbol{\Upsilon U}(k) - \boldsymbol{Y}^\star(k)] \\
&\quad + [\boldsymbol{\Gamma x}(k) + \boldsymbol{\Upsilon U}(k) - \boldsymbol{Y}^\star(k)]^T \boldsymbol{\Psi V_g}(k) \\
&\quad + [\boldsymbol{\Psi V_g}(k)]^T [\boldsymbol{\Gamma x}(k) + \boldsymbol{\Upsilon U}(k) - \boldsymbol{Y}^\star(k)] + [\boldsymbol{\Psi V_g}(k)]^T [\boldsymbol{\Psi V_g}(k)] \\
&= \Big\{ [\boldsymbol{\Gamma x}(k) - \boldsymbol{Y}^\star(k)]^T [\boldsymbol{\Gamma x}(k) - \boldsymbol{Y}^\star(k)] + [\boldsymbol{\Gamma x}(k) - \boldsymbol{Y}^\star(k)]^T \boldsymbol{\Upsilon U}(k) \\
&\quad + [\boldsymbol{\Upsilon U}(k)]^T [\boldsymbol{\Gamma x}(k) - \boldsymbol{Y}^\star(k)] + [\boldsymbol{\Upsilon U}(k)]^T [\boldsymbol{\Upsilon U}(k)] \Big\} \\
&\quad + 2 [\boldsymbol{\Gamma x}(k) + \boldsymbol{\Upsilon U}(k) - \boldsymbol{Y}^\star(k)]^T \boldsymbol{\Psi V_g}(k) + \boldsymbol{V_g}(k)^T \left[\boldsymbol{\Psi}^T \boldsymbol{\Psi}\right] \boldsymbol{V_g}(k) \\
&= \Big\{ \|\boldsymbol{\Gamma x}(k) - \boldsymbol{Y}^\star(k)\|_2^2 + 2 [\boldsymbol{\Gamma x}(k) - \boldsymbol{Y}^\star(k)]^T \boldsymbol{\Upsilon U}(k) + \boldsymbol{U}(k)^T \left[\boldsymbol{\Upsilon}^T \boldsymbol{\Upsilon}\right] \boldsymbol{U}(k) \Big\} \\
&\quad + 2 [\boldsymbol{\Gamma x}(k) + \boldsymbol{\Upsilon U}(k) - \boldsymbol{Y}^\star(k)]^T \boldsymbol{\Psi V_g}(k) + \|\boldsymbol{\Psi V_g}(k)\|_2^2
\end{aligned}$$

$$\begin{aligned}
J_B &= \lambda_u \|\boldsymbol{SU}(k) - \boldsymbol{Eu}(k-1)\|_2^2 \\
&= \lambda_u [\boldsymbol{SU}(k) - \boldsymbol{Eu}(k-1)]^T [\boldsymbol{SU}(k) - \boldsymbol{Eu}(k-1)] \\
&= \lambda_u \Big\{ [\boldsymbol{SU}(k)]^T \boldsymbol{SU}(k) - [\boldsymbol{SU}(k)]^T \boldsymbol{Eu}(k-1) \\
&\quad - [\boldsymbol{Eu}(k-1)]^T \boldsymbol{SU}(k) - [\boldsymbol{Eu}(k-1)]^T \boldsymbol{Eu}(k-1) \Big\} \\
&= \lambda_u \Big\{ - [\boldsymbol{SU}(k)]^T \boldsymbol{Eu}(k-1) - [\boldsymbol{Eu}(k-1)]^T \boldsymbol{SU}(k) \Big\} + \boldsymbol{U}(k)^T \left\{ \lambda_u \boldsymbol{S}^T \boldsymbol{S} \right\} \boldsymbol{U}(k) \\
&= \lambda_u \|\boldsymbol{Eu}(k-1)\|_2^2 - 2\lambda_u \Big\{ [\boldsymbol{Eu}(k-1)]^T \boldsymbol{SU}(k) \Big\} + \boldsymbol{U}(k)^T \left\{ \lambda_u \boldsymbol{S}^T \boldsymbol{S} \right\} \boldsymbol{U}(k),
\end{aligned}$$

$$\begin{aligned}
J &= J_A + J_B \\
&= \|\boldsymbol{\Gamma x}(k) - \boldsymbol{Y}^\star(k)\|_2^2 + \|\boldsymbol{\Psi V_g}(k)\|_2^2 + \lambda_u \|\boldsymbol{Eu}(k-1)\|_2^2 \\
&\quad + 2 [\boldsymbol{\Gamma x}(k) - \boldsymbol{Y}^\star(k)]^T \boldsymbol{\Upsilon U}(k) + 2 [\boldsymbol{\Gamma x}(k) + \boldsymbol{\Upsilon U}(k) - \boldsymbol{Y}^\star(k)]^T \boldsymbol{\Psi V_g}(k) \\
&\quad - 2\lambda_u \Big\{ [\boldsymbol{Eu}(k-1)]^T \boldsymbol{SU}(k) \Big\} \\
&\quad + \boldsymbol{U}(k)^T \left\{ \boldsymbol{\Upsilon}^T \boldsymbol{\Upsilon} + \lambda_u \boldsymbol{S}^T \boldsymbol{S} \right\} \boldsymbol{U}(k) \\
&= \|\boldsymbol{\Gamma x}(k) - \boldsymbol{Y}^\star(k)\|_2^2 + \|\boldsymbol{\Psi V_g}(k)\|_2^2 + \lambda_u \|\boldsymbol{Eu}(k-1)\|_2^2 + 2 [\boldsymbol{\Gamma x}(k) - \boldsymbol{Y}^\star(k)]^T \boldsymbol{\Psi V_g}(k) \\
&\quad + 2 [\boldsymbol{\Gamma x}(k) - \boldsymbol{Y}^\star(k)]^T \boldsymbol{\Upsilon U}(k) + 2 [\boldsymbol{\Upsilon U}(k)]^T \boldsymbol{\Psi V_g}(k) - 2\lambda_u \Big\{ [\boldsymbol{Eu}(k-1)]^T \boldsymbol{SU}(k) \Big\} \\
&\quad + \boldsymbol{U}(k)^T \left\{ \boldsymbol{\Upsilon}^T \boldsymbol{\Upsilon} + \lambda_u \boldsymbol{S}^T \boldsymbol{S} \right\} \boldsymbol{U}(k),
\end{aligned} \tag{3.7.1}$$

where

$$\boldsymbol{S} = \begin{bmatrix} \boldsymbol{I}_3 & \mathbf{0}_{3\times3} & \cdots & \mathbf{0}_{3\times3} \\ -\boldsymbol{I}_3 & \boldsymbol{I}_3 & \cdots & \mathbf{0}_{3\times3} \\ \mathbf{0}_{3\times3} & -\boldsymbol{I}_3 & \cdots & \mathbf{0}_{3\times3} \\ \vdots & \vdots & & \vdots \\ \mathbf{0}_{3\times3} & \mathbf{0}_{3\times3} & \cdots & \boldsymbol{I}_3 \end{bmatrix} \quad \text{and} \quad \boldsymbol{E} = \begin{bmatrix} \boldsymbol{I}_3 \\ \mathbf{0}_{3\times3} \\ \mathbf{0}_{3\times3} \\ \vdots \\ \mathbf{0}_{3\times3} \end{bmatrix}.$$

The matrices $\boldsymbol{S}$ and $\boldsymbol{E}$ consist of zero and identity matrices dimensioned 3-by-3 in accordance to the three phases of the system. More detail can be obtained in [46]. The eight terms in equation (3.7.1) are all added together to produce the cost J, which is a constant. Each of these terms are therefore also constants and can be seen as 1-by-1 matrices. A 1-by-1 matrix is a special case for which the following is permitted: $(\mathbf{JL})^T = \mathbf{L}^T\mathbf{J}^T$. Therefore the sixth term in equation (3.7.1) can be manipulated as follows:

$$\begin{aligned} 2\left[\boldsymbol{\Upsilon}\boldsymbol{U}(k)\right]^T\boldsymbol{\Psi}\boldsymbol{V_g}(k) &= 2\left\{\left[\boldsymbol{\Upsilon}\boldsymbol{U}(k)\right]^T\left[\boldsymbol{\Psi}\boldsymbol{V_g}(k)\right]\right\}^T \\ &= 2\left[\boldsymbol{\Psi}\boldsymbol{V_g}(k)\right]^T\left[\boldsymbol{\Upsilon}\boldsymbol{U}(k)\right] \\ &= 2\boldsymbol{V_g}^T(k)\boldsymbol{\Psi}^T\boldsymbol{\Upsilon}\boldsymbol{U}(k) \end{aligned}$$

From (3.7.1) the cost function can be written in the more compact form:

$$\begin{aligned} J &= \theta(k) + 2\boldsymbol{\Theta}^T(k)\boldsymbol{U}(k) + \boldsymbol{U}^T(k)\boldsymbol{Q}\boldsymbol{U}(k) \\ &= \theta(k) + 2\boldsymbol{\Theta}^T(k)\boldsymbol{U}(k) + \|\boldsymbol{U}(k)\|^2_{\boldsymbol{Q}}, \end{aligned}$$

where

$$\begin{aligned} \theta(k) &= \|\boldsymbol{\Gamma}\boldsymbol{x}(k) - \boldsymbol{Y}^\star(k)\|_2^2 + \|\boldsymbol{\Psi}\boldsymbol{V_g}(k)\|_2^2 \\ &\quad +\lambda_u\|\boldsymbol{E}\boldsymbol{u}(k-1)\|_2^2 + 2\left[\boldsymbol{\Gamma}\boldsymbol{x}(k) - \boldsymbol{Y}^\star(k)\right]^T\boldsymbol{\Psi}\boldsymbol{V_g}(k), \\ \boldsymbol{\Theta}(k) &= \{\left[\boldsymbol{\Gamma}\boldsymbol{x}(k) - \boldsymbol{Y}^\star(k)\right]^T\boldsymbol{\Upsilon} + \boldsymbol{V_g}^T(k)\boldsymbol{\Psi}^T\boldsymbol{\Upsilon} \\ &\quad -\lambda_u\left[\boldsymbol{E}\boldsymbol{u}(k-1)\right]^T\boldsymbol{S}\}^T, \\ \boldsymbol{Q} &= \boldsymbol{\Upsilon}^T\boldsymbol{\Upsilon} + \lambda_u\boldsymbol{S}^T\boldsymbol{S}, \end{aligned}$$

and $\boldsymbol{Q}$ is symmetric and positive definite. Hereby a vector $\boldsymbol{\xi}$ weighted with the matrix $\boldsymbol{Q}$ is given by $\|\boldsymbol{\xi}\|^2_{\boldsymbol{Q}} = \boldsymbol{\xi}^T\boldsymbol{Q}\boldsymbol{\xi}$. Only the first two variables of the new cost function, namely $\theta(k)$ and $\boldsymbol{\Theta}(k)$ change due to the inclusion of the grid voltage as an input vector $\boldsymbol{V_g}$ in the model, while $\boldsymbol{Q}$ remains the same as in [46]. The second term $2\boldsymbol{\Theta}^T(k)\boldsymbol{U}(k)$ of the new cost function is also a 1-by-1 vector, therefore

$$\begin{aligned} 2\boldsymbol{\Theta}^T(k)\boldsymbol{U}(k) &= 2\left[\boldsymbol{\Theta}^T(k)\boldsymbol{U}(k)\right]^T \\ &= 2\boldsymbol{U}^T(k)\boldsymbol{\Theta}(k) \end{aligned}$$

By considering this, the following algebraic manipulation and grouping can further be performed on the cost function:

$$\begin{aligned} J &= \|\boldsymbol{U}(k)\|^2_{\boldsymbol{Q}} + 2\boldsymbol{\Theta}^T(k)\boldsymbol{U}(k) + \theta(k) \\ &= \boldsymbol{U}^T(k)\boldsymbol{Q}\boldsymbol{U}(k) + \left[\boldsymbol{\Theta}^T(k)\boldsymbol{U}(k) + \boldsymbol{U}^T(k)\boldsymbol{\Theta}(k)\right] \\ &\qquad + \left[\boldsymbol{\Theta}^T(k)\boldsymbol{Q}^{-T}\boldsymbol{\Theta}(k) - \boldsymbol{\Theta}^T(k)\boldsymbol{Q}^{-T}\boldsymbol{\Theta}(k)\right] + \theta(k) \\ &= [\boldsymbol{U}^T(k)\boldsymbol{Q}\boldsymbol{U}(k) + \boldsymbol{U}^T(k)\boldsymbol{Q}\boldsymbol{Q}^{-1}\boldsymbol{\Theta}(k) + \boldsymbol{\Theta}^T(k)\boldsymbol{Q}^{-T}\boldsymbol{Q}\boldsymbol{U}(k) \\ &\qquad + \boldsymbol{\Theta}^T(k)\boldsymbol{Q}^{-T}\boldsymbol{Q}\boldsymbol{Q}^{-1}\boldsymbol{\Theta}(k)] - \boldsymbol{\Theta}^T(k)\boldsymbol{Q}^{-T}\boldsymbol{\Theta}(k) + \theta(k) \\ &= \left[\boldsymbol{U}(k) + \boldsymbol{Q}^{-1}\boldsymbol{\Theta}(k)\right]^T \boldsymbol{Q}\left[\boldsymbol{U}(k) + \boldsymbol{Q}^{-1}\boldsymbol{\Theta}(k)\right] - \boldsymbol{\Theta}^T(k)\boldsymbol{Q}^{-T}\boldsymbol{\Theta}(k) + \theta(k) \\ &= \left[\boldsymbol{U}(k) + \boldsymbol{Q}^{-1}\boldsymbol{\Theta}(k)\right]^T \boldsymbol{Q}\left[\boldsymbol{U}(k) + \boldsymbol{Q}^{-1}\boldsymbol{\Theta}(k)\right] + \text{const}(k) \end{aligned}$$

The constant term, consisting of $\boldsymbol{Q}$, $\boldsymbol{\Theta}(k)$ and $\theta(k)$, is dependent on the current state $\boldsymbol{x}(k)$, switch state $\boldsymbol{u}(k-1)$, reference $\boldsymbol{Y}^*$ and grid voltage $\boldsymbol{V_g}$ which are known values that remain constant during the search. The constant term is not dependent on $\boldsymbol{U}$, which changes as each of the available solution sequences are investigated for optimality. For these reasons the constant term may be omitted from the minimisation problem. The rest of the cost function is however a function of the variable $\boldsymbol{U}$, this is the part that needs minimisation.

$\boldsymbol{Q}$ is a positive semidefinite matrix as $\boldsymbol{z}^T\boldsymbol{Q}\,\boldsymbol{z} \geqslant 0$ for all $\boldsymbol{z} \in \mathbb{R}$. The transformation matrix $\boldsymbol{H}$ is a lower triangular matrix obtained by taking the Cholesky decomposition of $\boldsymbol{Q}^{-1}$, as:

$$\boldsymbol{H}^T\boldsymbol{H} = \boldsymbol{Q} \quad \text{where} \quad \boldsymbol{H} = \begin{bmatrix} h_{11} & 0 & 0 \\ h_{21} & h_{22} & 0 \\ h_{31} & h_{32} & h_{33} \end{bmatrix}. \tag{3.7.2}$$

$\boldsymbol{H}$ remains the same after the inclusion of the grid voltage because $\boldsymbol{Q}$ remains unchanged with regards to [46]. The unconstrained optimum $\boldsymbol{U}_{unc}$ is the optimal solution sequence obtained by removing the integer constraints of the switch state $\boldsymbol{u}$ as set out in equation (3.3.1) and is calculated as follows [46]:

$$\boldsymbol{U}_{unc}(k) = -\boldsymbol{Q}^{-1}\boldsymbol{\Theta}(k).$$

Due to a changed $\boldsymbol{\Theta}(k)$, the unconstrained optimum $\boldsymbol{U}_{unc}$ differs from that in [46] due to the influence of the grid. In the cost function $\boldsymbol{Q}$ and $\boldsymbol{Q}^{-1}\boldsymbol{\Theta}(k)$ are now replaced by $\boldsymbol{H}^T\boldsymbol{H}$ and $\boldsymbol{U}_{unc}$ respectively:

$$\begin{aligned} J &= \left[\boldsymbol{U}(k) - \boldsymbol{U}_{unc}(k)\right]^T \boldsymbol{H}^T\boldsymbol{H}\left[\boldsymbol{U}(k) - \boldsymbol{U}_{unc}(k)\right] + \text{const}(k) \\ &= \left[\boldsymbol{H}\left(\boldsymbol{U}(k) - \boldsymbol{U}_{unc}(k)\right)\right]^T \left[\boldsymbol{H}\boldsymbol{U}(k) - \boldsymbol{H}\boldsymbol{U}_{unc}(k)\right] + \text{const}(k) \\ &= \left[\boldsymbol{H}\boldsymbol{U}(k) - \bar{\boldsymbol{U}}_{unc}(k)\right]^T \left[\boldsymbol{H}\boldsymbol{U}(k) - \bar{\boldsymbol{U}}_{unc}(k)\right] + \text{const}(k). \end{aligned}$$

The optimal switching sequence is identified by searching for the sequence that results in the minimum cost J as in equation (3.6.1). This problem is

now reformulated into an integer least-squares (ILS) problem in vector form with $\boldsymbol{U}$ as the optimisation variable:

$$\boldsymbol{U}_{opt}(k) = \arg\min_{\boldsymbol{U}(k)} \left\| \boldsymbol{H}\boldsymbol{U}(k) - \bar{\boldsymbol{U}}_{unc}(k) \right\|_2^2, \tag{3.7.3}$$

$\bar{\boldsymbol{U}}_{unc}$ is obtained by multiplying the unconstrained solution with the transformation matrix $\boldsymbol{H}$:

$$\bar{\boldsymbol{U}}_{unc}(k) = \boldsymbol{H}\boldsymbol{U}_{unc}(k). \tag{3.7.4}$$

To illustrate the influence of the $\boldsymbol{H}$ matrix, an example is presented in Figure 3.5 of a three-phase system over a horison of $N = 1$. Each axis in the orthogonal coordinate system represents the switch state of one phase-leg. The dashed line cube represents the orthogonal solution space and the points on its vertices, all candidate sequences. The orthogonal coordinate system is transformed by multiplication with the transformation matrix $\boldsymbol{H}$ and delivers a scaled and skewed solution space, indicated by the small solid line cube in Figure 3.5. An exhaustive search has to be performed by evaluating every point $\boldsymbol{H}\boldsymbol{U}$ with equation (3.7.3) to identify the solution with the shortest euclidean distance from the transformed unconstrained solution $\bar{\boldsymbol{U}}_{unc}$ [12].

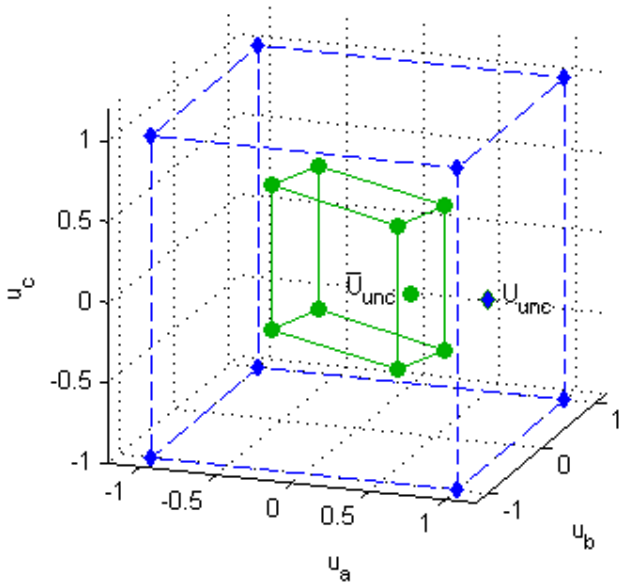

Figure 3.5: Visualisation of the optimisation problem for a three-phase system with a horison of $N = 1$ in an orthogonal coordinate system (dashed blue line) and how it compares with the transformed problem (solid green line).

In a system with p phases (or legs) each with s possible switch positions, the number of possible switching states $\boldsymbol{u}(k)$ can be expressed as s^p. The number of candidate switching sequences $\boldsymbol{U}(k)$ that exist over a horisons of

N time steps are s^{pN}. For this three-phase system with two possible switch positions per phase, there are 2^{3N} candidate sequences. Traditionally, in the search for an optimal sequence within the set of all candidate sequences, each one of these sequences are evaluated by the cost function to find the least costly one. This approach is only feasible for short horisons because as N increases the number of candidate solutions increases exponentially. In the case of long horisons a sphere decoding algorithm can optimise the search process.

3.8 Sphere Decoding

The aim of sphere decoding is to exclude as many sub-optimal solutions as possible from the search by only evaluating solution points within the radius ρ of a sphere centred around the transformed unconstrained optimum $\bar{\boldsymbol{U}}_{unc}$.

$$\rho(k) \geq \left\| \bar{\boldsymbol{U}}_{unc}(k) - \boldsymbol{H}\boldsymbol{U}(k) \right\|_2$$

Because $\boldsymbol{H}$ is a lower triangular matrix, the equation for the sphere radius can be rewritten as follows [12]:

$$\begin{aligned} \rho^2(k) \quad \geq \quad & (\bar{u}_{unc,1}(k) - h_{11}u_1(k))^2 \\ & + (\bar{u}_{unc,2}(k) - h_{21}u_1(k) - h_{22}u_2(k))^2 \\ & + (\bar{u}_{unc,3}(k) - h_{31}u_1(k) - h_{32}u_2(k) - h_{33}u_3(k))^2 \\ & + \ldots \end{aligned} \tag{3.8.1}$$

where h_{ij} represents the $(i,j)^{\text{th}}$ element in the transformation matrix $\boldsymbol{H}$ as in Equation 3.7.2, and $\bar{u}_{unc,i}(k)$ and $u_i(k)$ represent the i^{th} elements in the vectors $\bar{\boldsymbol{U}}_{unc}(k)$ and $\boldsymbol{U}(k)$. Hereby the radius calculation can be simplified into one-dimensional parts that can be solved sequentially. These parts can be associated with the dimensions in the solution space illustrated in Figure 2.9 or with the levels in the solution-search tree provided in Figure 2.8. This search tree is based on the branch-and-bound principle: branching entails exploring the possible switching sequences available, while bounding limits the search to sequences that fall within the sphere.

It is important to choose the initial radius in such a way that it is small enough to eliminate as many candidate switching sequences as possible, yet large enough to avoid having an empty solution due to all solutions falling outside of the sphere. The initial radius is calculated with an initial estimate $\boldsymbol{U}_{ini}(k)$ of a possible optimum solution:

$$\rho_{ini}(k) = \left\| \bar{\boldsymbol{U}}_{unc}(k) - \boldsymbol{H}\boldsymbol{U}_{ini}(k) \right\|_2 .$$

The initial solution estimate is determined by component-wise rounding (represented by the *floor* and *ceiling* rounding indicators $\lfloor$ and $\rceil$) of the

unconstrained solution to the nearest finite control set values of 1 or −1. This is known as the Babai estimate [79]:

$$\boldsymbol{U}_{ini}(k) = \lfloor \boldsymbol{U}_{unc}(k) \rceil.$$

In Figure 3.6, viewing the solution space in Figure 3.5 from above, an example is given of how the sphere is applied. The unconstrained optimum $\boldsymbol{U}_{unc}$ of the orthogonal solution space is an equal distance away from two possible solution points, $[1\ 1\ 1]^T$ and $[1{-}1\ 1]^T$. The optimal solution cannot be declared before the transformation by applying $\boldsymbol{H}$ has been performed as in (3.7.4). In the transformed solution space it is observed that the one solution point falls outside of the sphere before the other, therefore exposing the true optimal solution $\boldsymbol{U}_{opt}$ [12].

The sphere decoder is a recursive function and for a three-phase system it will enter $3N$ recursive levels. The structure of the function is provided in the sphere decoding algorithm, adapted from [12]:

function $\boldsymbol{U}_{opt}, \rho^2 = \text{SphDec}(\boldsymbol{U}, d^2, i, \rho^2, \bar{\boldsymbol{U}}_{unc})$
  for each $u \in \{-1, 1\}$ **do**
    $U_i = u$
    $d'^2 = \left\|\bar{U}_{i,unc} - \boldsymbol{H}_{i,1:i}\boldsymbol{U}_{1:i}\right\|_2^2 + d^2$
    if $d'^2 \leq \rho^2$ **then**
      if $i < 3N$ **then**
        $\boldsymbol{U}'_{opt}, \rho'^2 = \text{SphDec}(\boldsymbol{U}, d'^2, i+1, \rho^2, \bar{\boldsymbol{U}}_{unc})$
        $\boldsymbol{U}_{opt} = \boldsymbol{U}'_{opt}$
        $\rho^2 = \rho'^2$
      else
        $\boldsymbol{U}_{opt} = \boldsymbol{U}$
        $\rho^2 = d'^2$
      end if
    end if
  end for end function

$\boldsymbol{U}$ is compiled one component at a time evaluating the switch-state options from the set $u \in \{-1, 1\}$ for each phase leg. As the sphere decoder advances from one level to the next, the distance of the possible solutions from its centre is calculated according to the simplified one-dimensional problem provided in Equation 3.8.1. The triangular $\boldsymbol{H}$ matrix makes it possible to determine the squared distances d'^2 component-by-component by adding to the summed total d^2 of the preceding levels. If the particular squared Euclidean distance d'^2 is smaller than the current squared radius ρ^2 of the sphere, the decoder proceeds

to the next switch component U_{i+1} in $\boldsymbol{U}$. When the decoder reaches the last component U_{3N}, a complete candidate solution sequence $\boldsymbol{U}$ is obtained, and if its distance is less than that of the current optimum from the sphere centre, the radius is updated to this distance and the value of $\boldsymbol{U}$ is stored as the new optimum $\boldsymbol{U}_{opt}$.

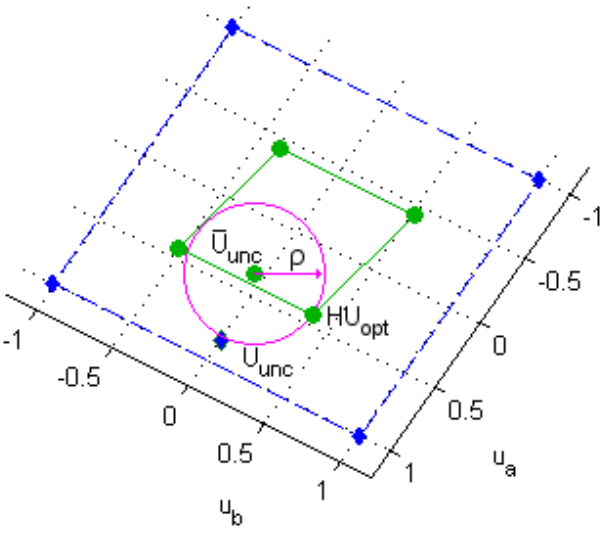

Figure 3.6: Top view of Figure 3.5 showing the *ab*-plane to gain perspective on the sphere and the points which lie closest to its centre.

3.9 Summary

In Figure 3.7 the main themes of this chapter are briefly listed. Within the chapter a current controller design for a three-phase grid-connected converter with LCL-filter is provided. Finite control set (FCS) model predictive control (MPC) is used to manipulate the semiconductor switches in the converter directly in order to perform control in the system. The dynamics of the switches are incorporated as an integer constraint. A state-space model was derived to capture the dynamics of the system and calculate its response to the switching actions included as an input vector. The output vector includes all state variables for control. The grid voltage was incorporated into the model as an additional input vector along-side the switching vector. Therefore the optimisation approach, used to transform the cost-function minimisation problem towards the integer least-squares (ILS) problem, had to be reworked to consider this additional element, hereby extending on the work done in [46]. The cost function consisting of two control objectives, namely minimising tracking-error and switching losses, was compiled for the means of evaluating the future impact and optimality of possible switching sequences. A sphere

decoding algorithm was incorporated as an efficient way of solving the ILS problem for long horisons.

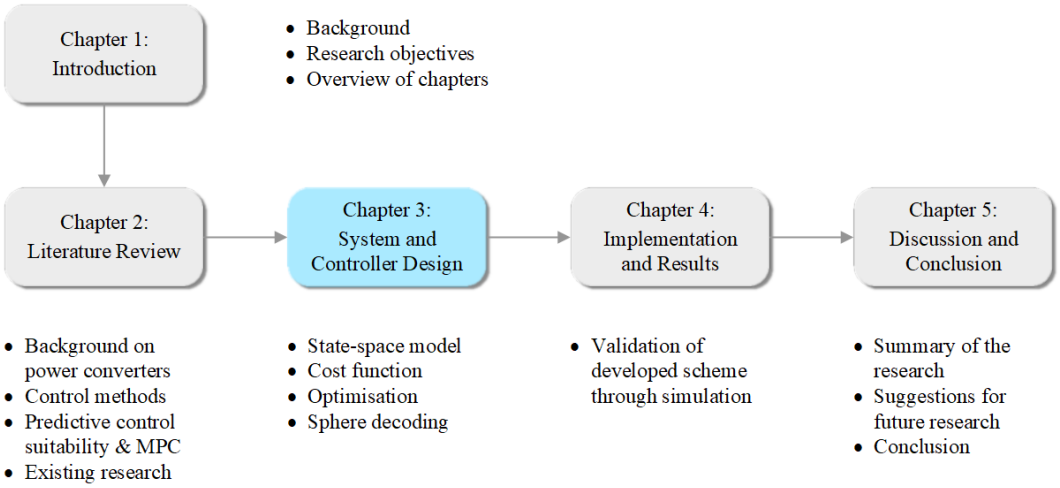

Figure 3.7: Brief overview of the thesis chapters.

Chapter 4

Implementation and Results

4.1 Introduction

In this chapter the current control strategy developed in Chapter 3 is evaluated in terms of its applicability to grid-tied converters by comparing the following approaches through simulation:

- model predictive control (MPC) with a short prediction horison of one time step,
- model predictive control with a long prediction horison of twelve time steps,
- open-loop pulse width modulation (PWM), a general technology that is used with grid-connecting power converters [18], and
- naturally-sampled space vector modulation (SVM), a variation of PWM.

Firstly the simulation design provides an explanation on how these control scenarios are implemented in simulation to allow for their evaluation. Thereafter the results produced by the simulation are presented and discussed. Finally the conclusion provides a summary of the findings.

4.2 Simulation design

4.2.1 Model predictive control

A MATLAB script was written to simulate the controller that is discussed in Chapter 3. In Figure 4.1 a flow diagramme is presented which explains the logic processes within the written MATLAB script. The first task is to initialise the system parameters such as the filter's component values, and provide the state-space matrices that describe the system behaviour. These are then used to build the integer quadratic formulation matrices $\boldsymbol{\Gamma}, \boldsymbol{\Upsilon}, \boldsymbol{\Psi}, \boldsymbol{S}$ and $\boldsymbol{E}$. The

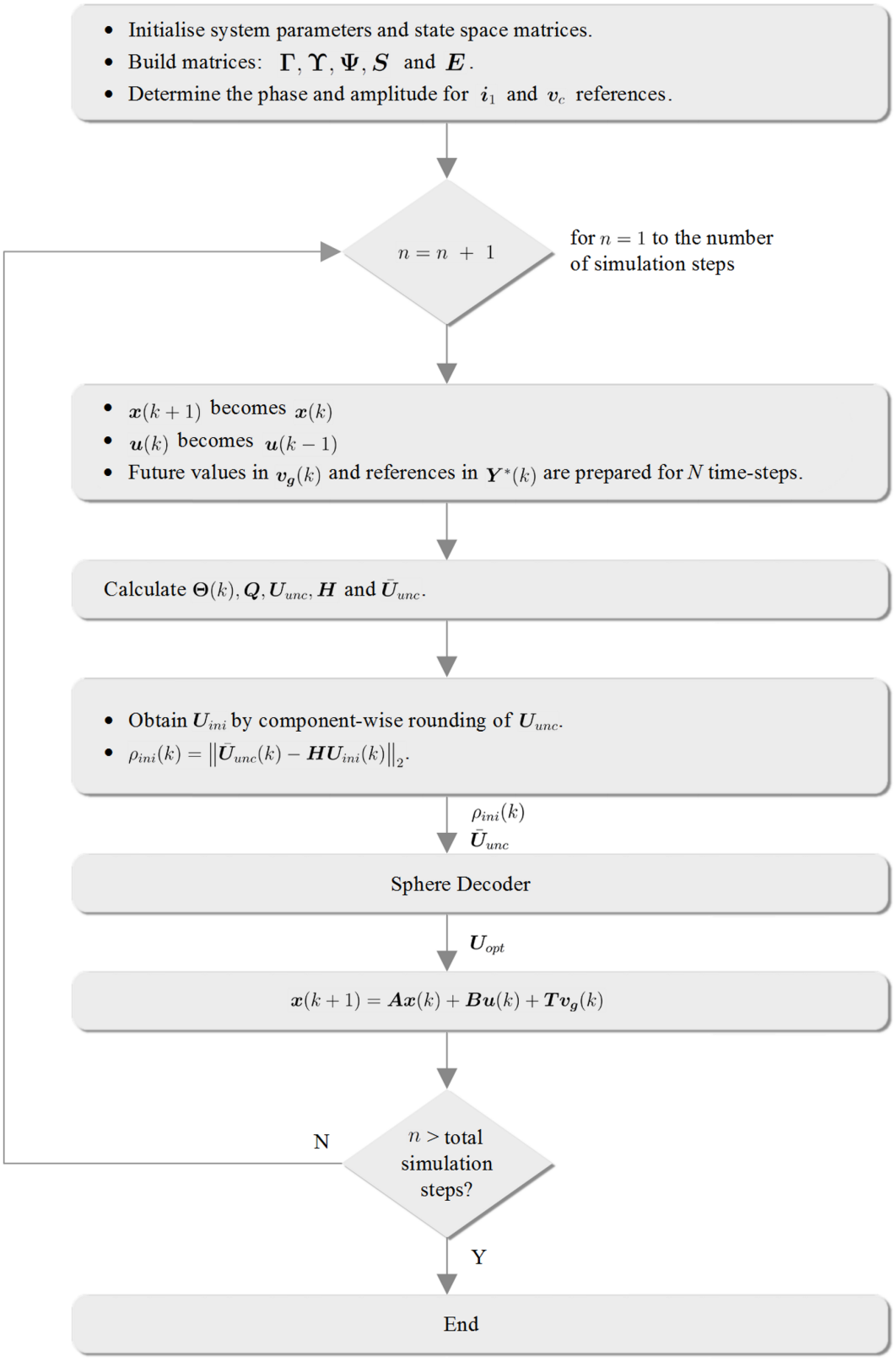

Figure 4.1: Main function flow diagram of the direct MPC simulation script.

phase and amplitude for the $\boldsymbol{i}_1$ and $\boldsymbol{v}_c$ references are determined from phasor calculations using the known grid-current reference.

A loop is used to count down each simulation step that is performed. During each time step the optimisation approach and sphere decoder is applied to select the optimal switching sequence and apply its first state before the next re-evaluation. The future state of the system $\boldsymbol{x}(k+1)$ calculated with the state space equation $\boldsymbol{x}(k+1) = \boldsymbol{A}\boldsymbol{x}(k)+\boldsymbol{B}\boldsymbol{u}(k)+\boldsymbol{T}\boldsymbol{v}_{\boldsymbol{g}}(k)$ as in Equation 3.5.2, it then becomes the current state. The future reference values contained in $\boldsymbol{Y}^*(k)$ for $\boldsymbol{i}_1, \boldsymbol{i}_2$ and $\boldsymbol{v}_c$ are prepared for the N time steps of the horison. The grid-voltage vector $\boldsymbol{V}_{\boldsymbol{g}}(k)$ is also filled with its N future values. Thereafter $\boldsymbol{\Theta}(k), \boldsymbol{Q}$, the unconstrained solution $\boldsymbol{U}_{unc}(k)$, the transformation matrix $\boldsymbol{H}$ and the transformed unconstrained solution $\boldsymbol{U}_{unc}(k)$ are calculated accordingly. The initial solution estimate $\boldsymbol{U}_{unc}(k)$ is obtained when the unconstrained solution is rounded component-wise. The initial radius $\rho_{ini}(k)$ is the Euclidean distance between the transformed initial solution estimate and the transformed unconstrained solution. $\boldsymbol{U}_{unc}(k)$ and $\rho_{ini}(k)$ is then supplied to the sphere decoding function to perform an efficient search for the optimal solution. The sphere decoding function then returns the optimal solution sequence $\boldsymbol{U}_{opt}(k)$ to the main function. Only the first element of the sequence is applied as the switch state to the state-space model. This process continues until the end of the simulation is reached.

4.2.2 System parameters

The system is specified to have a constant DC-link voltage of V_D= 1000 V and a grid-side current reference with an amplitude of 20 A and phase of zero degrees with respect to the grid voltage. The fundamental frequency is 50 Hz and the grid voltage is assumed to be constant with a $230\sqrt{2}$ V amplitude. The filter parameters are provided in Table 4.1. The constants in the $\boldsymbol{C}$ matrix of the state-space model from Equation 3.5.1 are assigned the following control weightings: $k_1 = k_2 = 1$ for the inductor currents and $k_3 = 0.1$ for control of

Table 4.1: System parameters

Parameter		Value
DC voltage	V_D	1000 V
Grid-voltage amplitude	V_g	$230\sqrt{2}$ V
Reference-current amplitude	I_2^*	20 A
Converter-side inductor	L_1	20 mH
Grid-side inductor	L_2	1.6 mH
Internal resistances	$R_1 = R_2$	0.1 Ω
Filter capacitor	C	65.25 μF
Capacitor resistance	R_c	5 Ω

the capacitor voltage. For the discussions that follow on the sample output, dynamic response and the spectrum, a long-horison approach with $N = 12$ is used to demonstrate the functioning of the simulation and the developed model for the controller. The weighting factor in the cost function is set to $\lambda_u = 2$ to obtain a switching frequency of $f_{sw} = 1.2$ kHz at a sampling period of $T_s = 40\mu$s.

4.2.3 Weighting factor adjustment

The weighting factor λ_u determines the trade-off between the two control objectives in the cost function (Equation 3.6.1) namely minimisation of tracking error and switching frequency. Figures 4.2 and 4.3 show the influence of λ_u on each of the two objectives respectively for a single-phase long-horison ($N = 12$) scenario. The weighting factor is applied as a penalty on the switching term in the cost function, and can be adjusted in order to obtain a specific average switching frequency. Because the controller searches for a new optimal sequence at every sampling instant k, the switching is variable throughout the simulation, not having a fixed sequence or switching frequency. The switching frequency is therefore calculated as an average by dividing half of the total switch changes throughout the steady-state of the simulation, through the total elapsed time in steady-state.
It can be seen that when the value of λ_u is increased to the extent that the switching frequency tends toward zero, the tracking error greatly increases, as

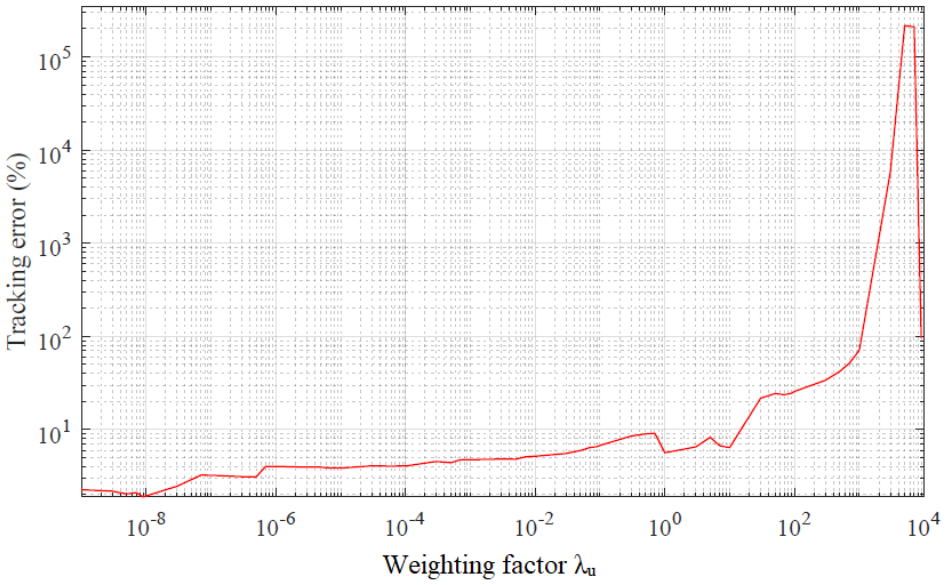

Figure 4.2: An example of how adjustment of the weighting factor can influence the current-tracking error for a single-phase controller with a long horison of $N = 12$.

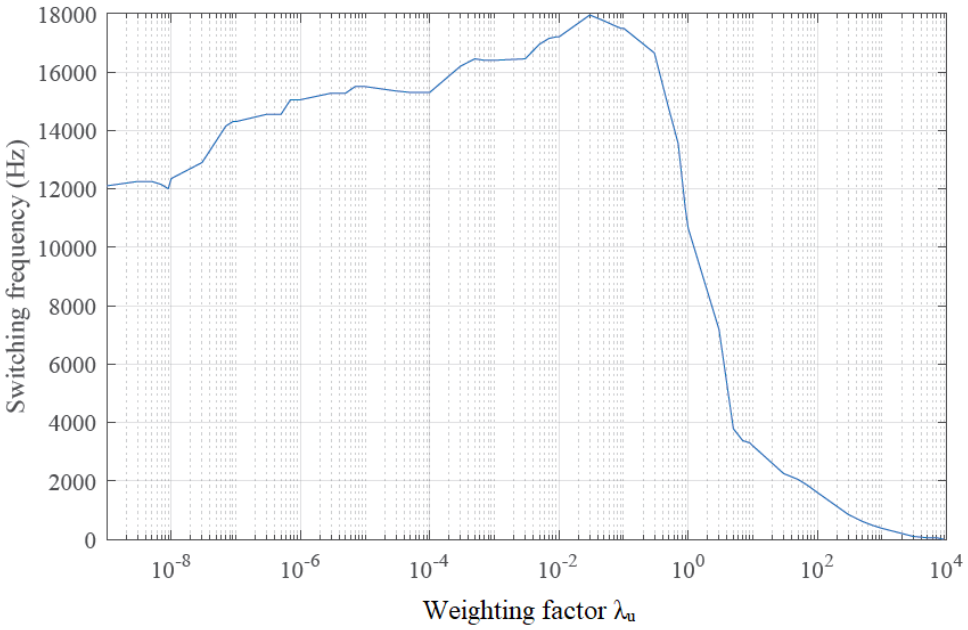

Figure 4.3: An example of how switching frequency changes with the adjustment of the weighting factor for a single-phase controller with a long horison of $N = 12$.

the controller becomes more and more restricted to change the switch state in order to bring a correction to the signal to follow its reference. At very small values of λ_u, the penalty on the switching term becomes so small it tends to zero, therefore providing freedom to the controller to prioritise tracking accuracy, thus minimising the tracking error.

4.2.4 Sphere decoding

The sphere decoder algorithm within Section 3.8 is a recursive function and for a three-phase system it will enter $3N$ recursive levels. Figure 4.4 demonstrates the computational efficiency that the sphere decoding algorithm offers by counting the number of floating point operations (FLOPS) that are performed during the execution of the solution search. Addition, subtraction, multiplication, division and a square root is each counted as one FLOP. An exhaustive search was done by modifying the sphere decoding function in such a way that it does not prune sub-optimal solution branches and explores the whole search tree. This differs from the traditional approach of performing an exhaustive search by reaching the possible solutions through a systematic exploration of the search tree which offers simplified adaptability of the horison length. Figure 4.4 presents the FLOPS per solution search on a log scale according to horison length for both an exhaustive search and an optimised

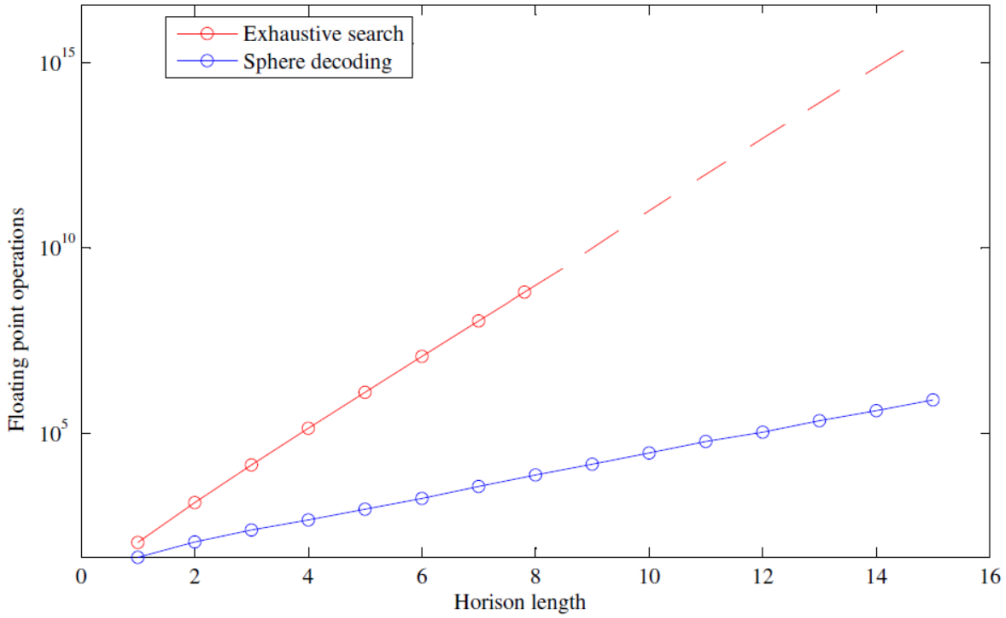

Figure 4.4: FLOPS executed during an exhaustive search, and during an optimised search using sphere decoding.

search completed by the sphere decoder. The FLOPS are counted for each time step of the first fundamental period from $t = 0$s to $t = 0.02$s and then averaged. It can be seen that an exhaustive search becomes computationally overwhelming [12] at a horison length of about $N = 8$, but it indicates a definite trend for what can be expected from the longer horisons. Both the exhaustive and sphere decoding methods display exponential growth as the horison length increases. The sphere decoding algorithm provides a very significant reduction in computational effort and is able to allow predictions of up to fifteen time steps long.

4.2.5 Disregarding the grid

The MPC strategy developed incorporates the grid voltage in the optimisation approach building on previous work done [46]. To determine the performance of a controller that does not consider the grid voltage, the grid voltage vector $\boldsymbol{V_g} = [\boldsymbol{v_g}(k)\ \boldsymbol{v_g}(k+1)\ \ldots\ \boldsymbol{v_g}(k+N-1)]$ is set to zero for the solution search. When calculating the outcome of the state variables as a result of the selected switching action, the grid-voltage is given its true value to determine the effect in a grid-connected scenario. Figure 4.5 provides the resulting grid-side current waveform i_{2a} and the reference signal i^*_{2a}. It is seen that the controller is unable to provide accurate current tracking with the amplitude of i_{2a} about a quarter of that of its reference.

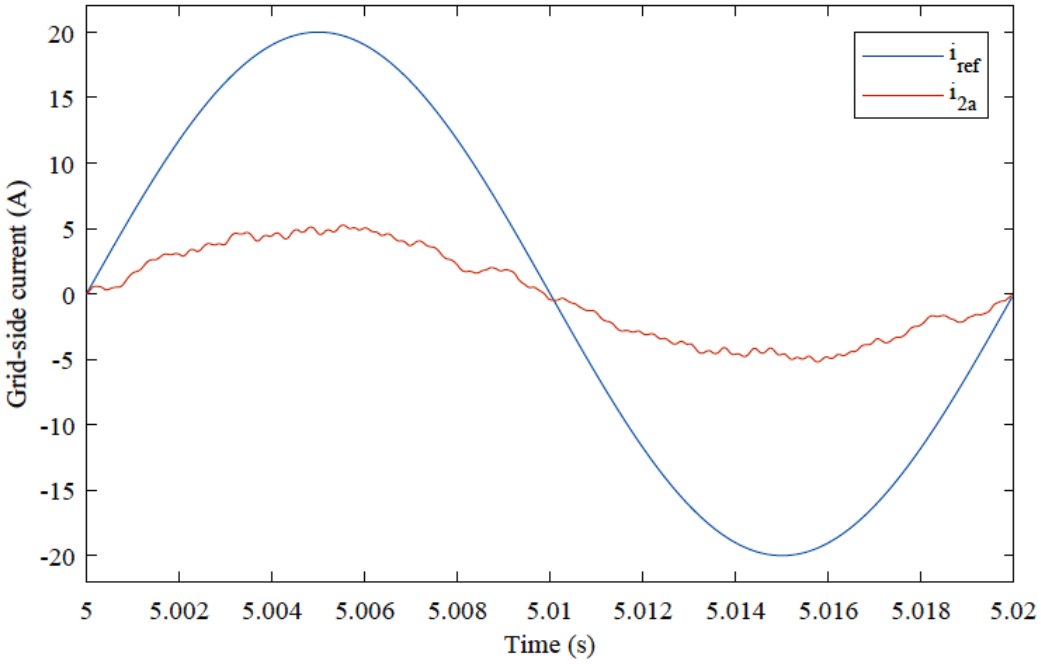

Figure 4.5: Resulting grid-side current and reference for a controller that disregards the grid-voltage in the optimisation approach.

4.2.6 Sample output

Figure 4.6 provides the steady-state grid-side current $\boldsymbol{i}_2$ against its reference $\boldsymbol{i}_2^*$ in all three phases. It can be seen how the values of $\boldsymbol{i}_2$ vary around the corresponding references as a result of the switching ripple. This variation coincides with the changing switch states. It can be seen that the waveforms are not identical. The switch state in a specific phase leg does have an influence on the future states of the system across all phases. During the selection of an optimal control sequence, the switching sequence within each phase may differ in any way, as long as the resulting three-phase waveforms are collectively most optimal according to the weighted objectives within the cost function. Therefore the selected three-phase switching sequence must minimise the cost J by providing the best trade-off between the number of switching and reference-tracking error combined.

Figure 4.7 shows the two a-phase inductor currents i_{1a} and i_{2a} with their references. A phase difference which is introduced by the filter capacitance [47] is observed between the two inductor currents. The converter-side current $\boldsymbol{i}_1$ is a result of large ripple. After this ripple current passes through the filter capacitor, the ripple in the grid-side current $\boldsymbol{i}_2$ is greatly reduced compared to that in $\boldsymbol{i}_1$. The a-phase capacitor voltage and its reference are provided in Figure 4.8. The capacitor voltage is very smooth and follows its reference very well without noticeable ripple.

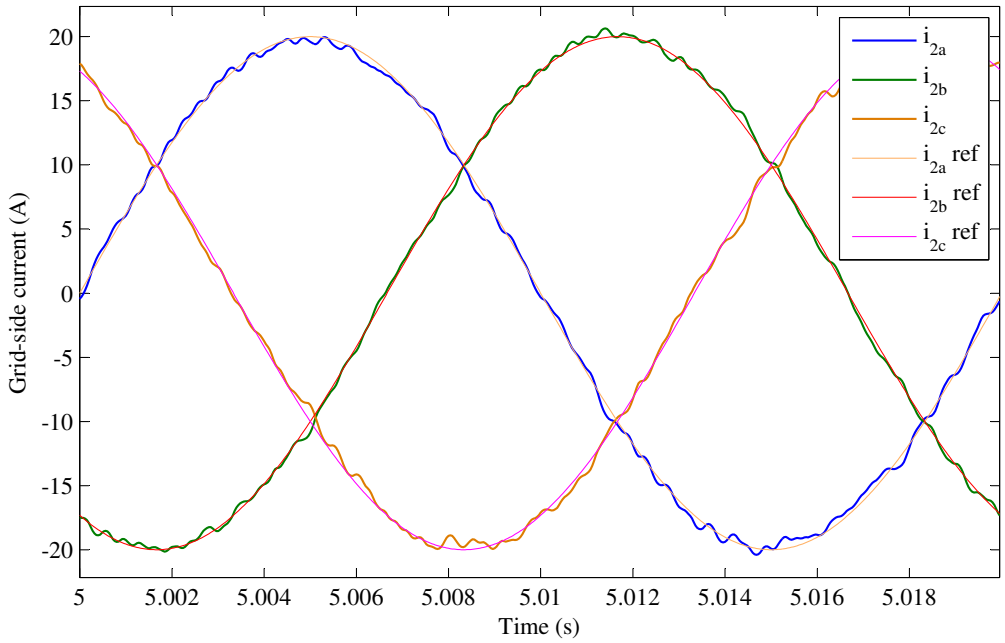

Figure 4.6: Steady-state three-phase output currents and references using a long horison of $N = 12$.

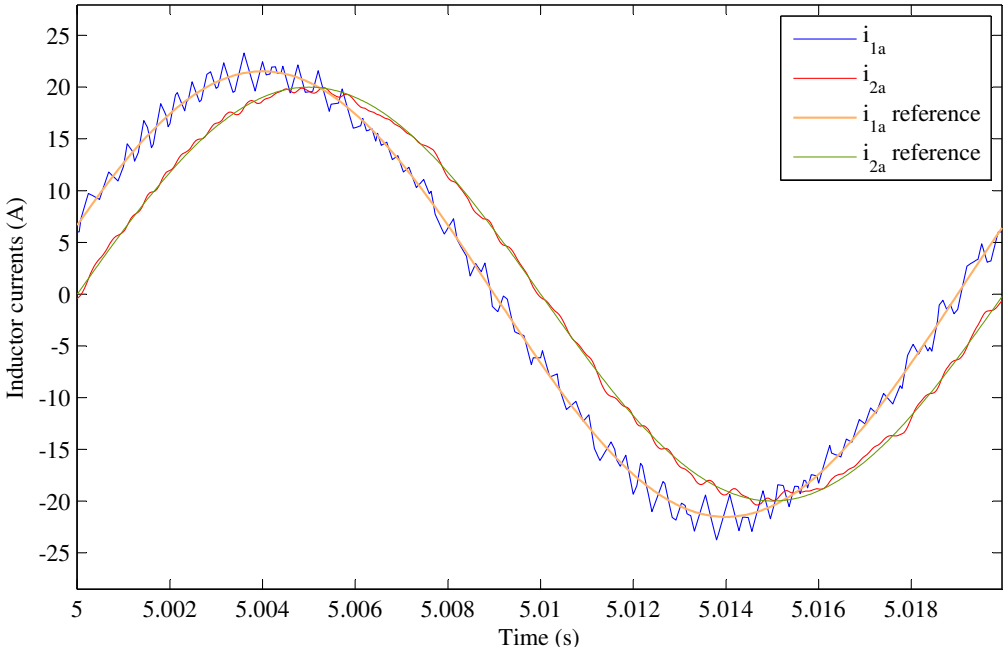

Figure 4.7: Inductor currents and references in the a-phase during steady-state operation with a long horison of $N = 12$.

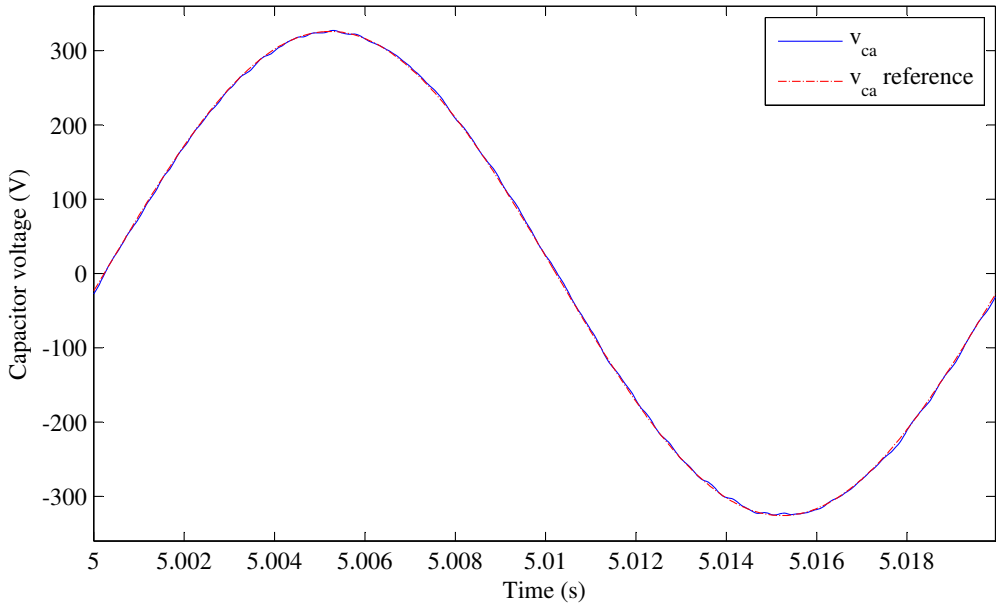

Figure 4.8: Capacitor voltage and its reference in the a-phase during steady-state operation with a long horison of $N = 12$.

4.2.7 Dynamic response of MPC model

The transient response of the developed and implemented MPC model is validated by applying a step in amplitude to the grid-current reference. The response of the system to this step is observed in Figure 4.9 and Figure 4.10 for the short-horison ($N = 1$) and long-horison ($N = 12$) approach respectively. This step in the reference is simulated in such a way that the controller is able to anticipate it, and is tested to show the dynamic response of the MPC controller in general. Both short-horison and long-horison approaches show fast and smooth transient responses, with little overshoot present after the abrupt step in amplitude. It is observed that the long-horison controller anticipated the step and made early adjustments before the step was encountered. From the moment the new amplitude was enforced, the controller was able to adjust the grid-current amplitude to the desired level in 0.001 seconds, the duration of 25 sampling periods equivalent to 1.2 times an averaged switching period. The short-horison controller only responded optimally a while after the occurrence of the step was encountered, fully adjusting within 0.0017 seconds, leaving it at a disadvantage with regards to response time.

Figure 4.11 shows the transient response when the controller does not anticipate an approaching step in the future. The increase in amplitude is only implemented in the reference output sequence

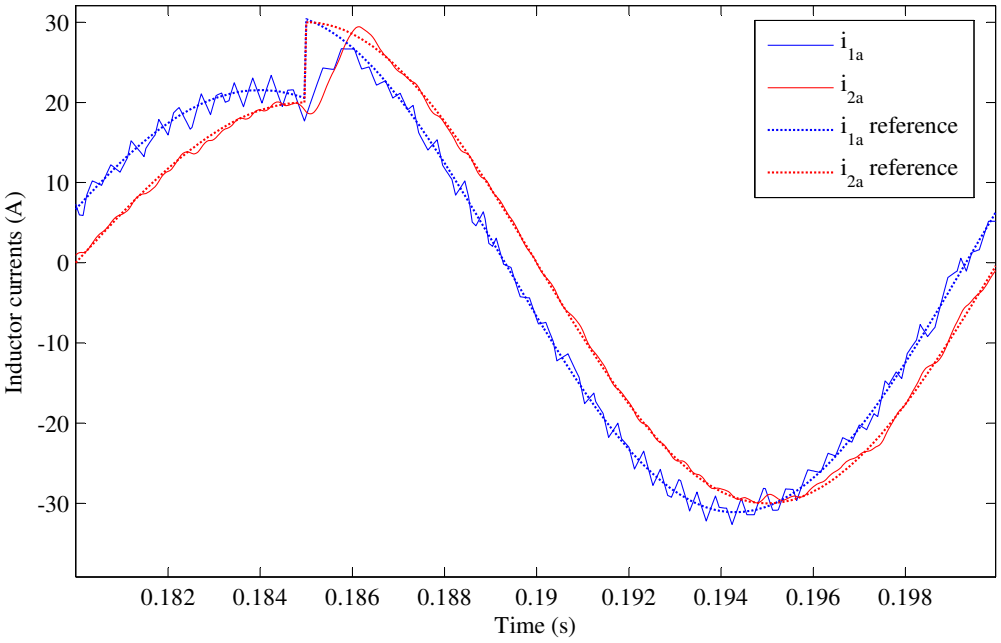

Figure 4.9: Response of inductor currents to a step in the reference amplitude using a short horison of $N = 1$.

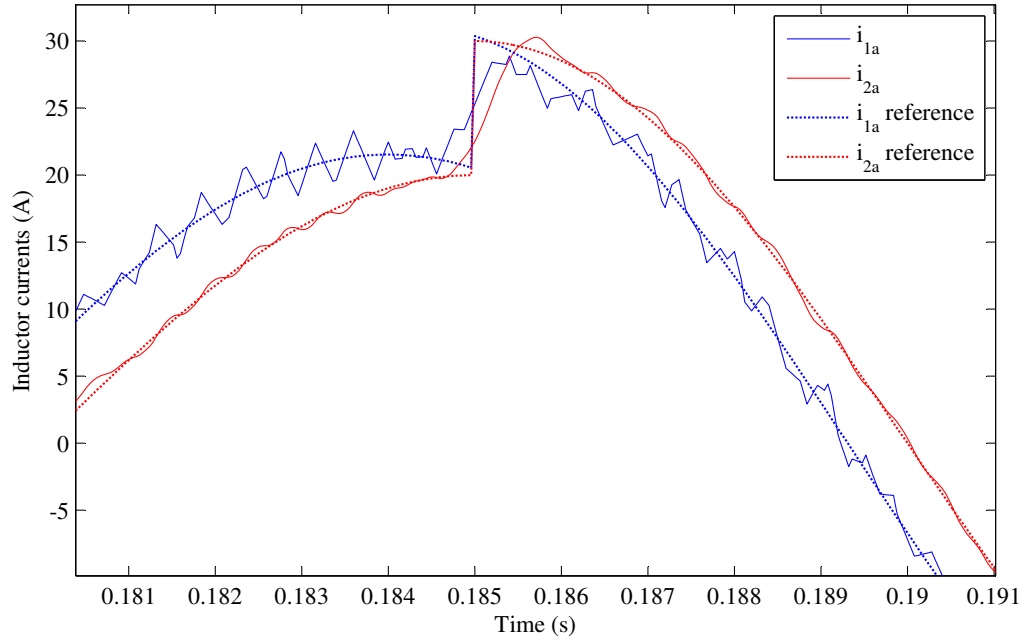

Figure 4.10: Response of inductor currents to a step in the reference amplitude using a long horison of $N = 12$.

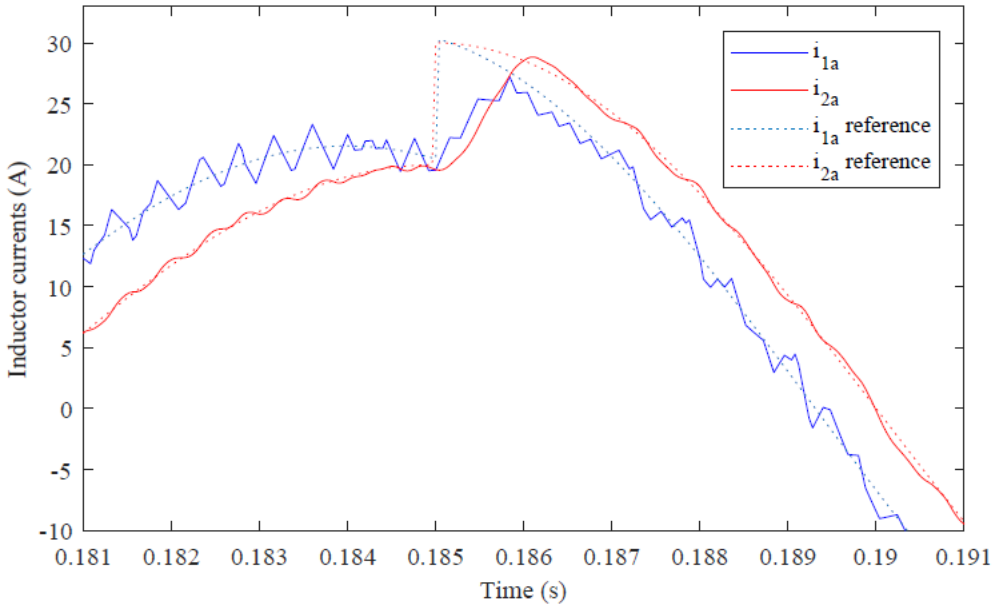

Figure 4.11: Response of inductor currents to an unanticipated step in the reference amplitude using a long horison of $N = 12$.

$\boldsymbol{Y}^*(k) = [\boldsymbol{y}^*(k+1) \ \ldots \ \boldsymbol{y}^*(k+N)]^T$ once the step reaches time step k. The long-horison controller has minimal overshoot and is also able to adjust quickly within 0.001 seconds, but is not able to minimise the tracking error as effectively as an anticipated step where the controller implements adjustments before the step is reached.

4.3 Spectral analysis of MPC

Figure 4.12 provides the resulting spectrum $I_2(f)$ in decibels (dB) for a long-horison approach with N=12, f_{sw}=1.2 kHz and T_s=40μs calculated from the grid-side current's values between 250 and 350 simulated periodic 50 Hz cycles using a rectangular window. Model predictive control spreads the spectral content by transferring some of the switching energy into noise instead of harmonics. For this reason the spectrum is divided up into 50 Hz frequency bands which serve as bins within which all energy is summed to produce the discrete harmonics that take into account all energy, including that dispersed as noise. The resulting harmonics of $I_2(f)$ and $I_1(f)$, at multiples of the fundamental 50 Hz frequency, are provided in Figure 4.13 and Figure 4.14 respectively. The first harmonic is at the fundamental frequency f_1 and represents the amplitude of the sinusoidal grid-side current $\boldsymbol{i}_2$ and converter-side current $\boldsymbol{i}_1$. The harmonics that follow represent the distortion in the signals.

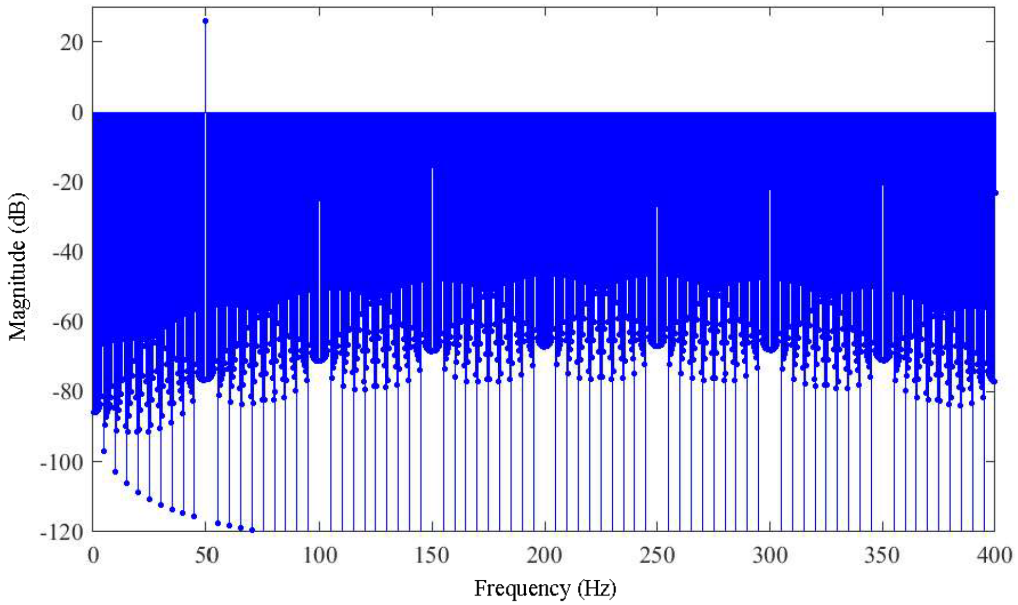

Figure 4.12: Output-current spectrum of the a-phase.

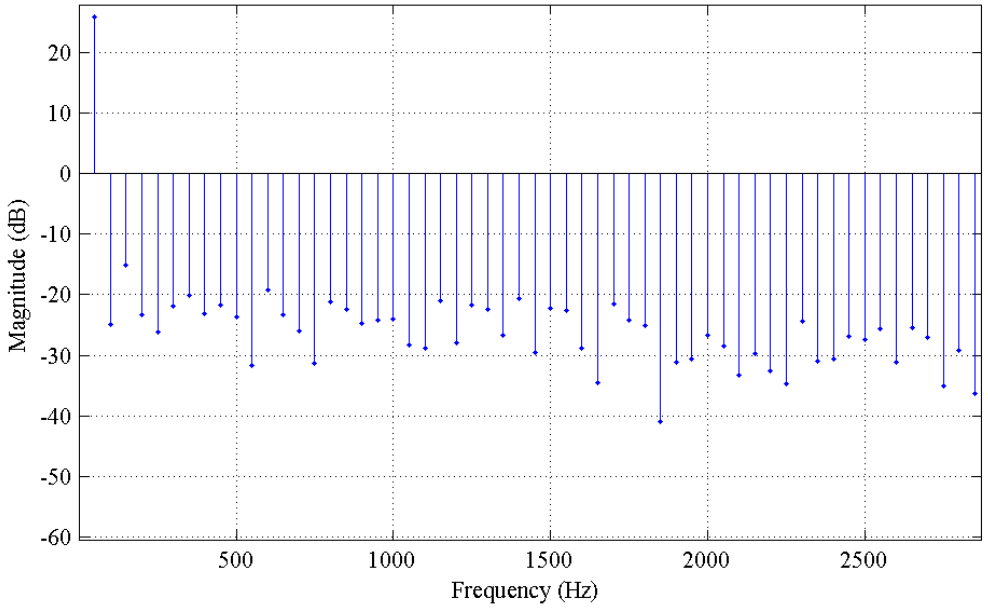

Figure 4.13: Output-current spectrum of the a-phase with discrete harmonics.

The total harmonic distortion (THD) of the grid-side current is calculated by taking the square root of the sum of squared harmonic amplitudes excluding the fundamental component $I_{2(1)}$, then dividing that square root by $I_{2(1)}$ [16; 80]. The overall THD for the three phases was determined by summing the

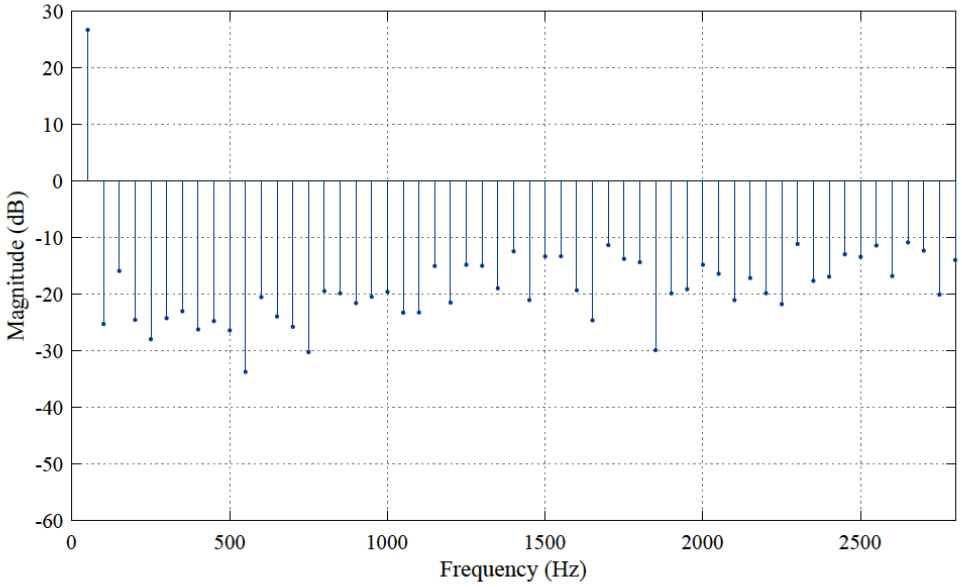

Figure 4.14: Converter-current spectrum of the a-phase with discrete harmonics.

THD's of the individual phases and taking their mean [12].

$$THD = \left(\frac{1}{I_{2(1)}} \sqrt{\sum_{n=2}^{\infty} \left| I_{2(n)} \right|^2} \right) \times 100\%$$

4.3.1 Pulse width modulation

The direct MPC current-control model developed during this study is compared to the performance of an open-loop, naturally sampled PWM control scheme. Pulse width modulation (PWM) is studied extensively as a classic method for current control. The comparator of a pulse width modulator generates a pulsed signal by comparing a sinusoidal reference voltage to a triangular carrier signal. This pulsed signal drives the semiconductor switches and has a fundamental component that is proportional to the reference signal [10]. To implement the PWM controller and obtain its resulting grid-current spectrum, the amplitude and phase of the reference signal has to be determined. Firstly the impedances in the system, provided in Figure 4.15, are grouped as follows:

$$\begin{aligned}\tilde{Z}_1 &= R_1 + sL_1 \\ \tilde{Z}_2 &= R_2 + sL_2 \\ \tilde{Z}_c &= R_c + \frac{1}{sC},\end{aligned}$$

where $s = j\omega$ and $\omega = 2\pi f$. Kirchoff's voltage law is applied to the circuit in order to obtain the transfer function $H(s) = \frac{I_2(s)}{V_i(s)}$:

$$\begin{aligned}0 &= -\tilde{V}_i + \tilde{Z}_1\tilde{I}_1 + \tilde{V}_x \\ &= -\tilde{V}_i + \tilde{Z}_1\left(\frac{\tilde{V}_x}{\tilde{Z}_2||\tilde{Z}_c}\right) + \tilde{V}_x \\ &= -\tilde{V}_i + \tilde{V}_x\left(1 + \frac{\tilde{Z}_1}{\tilde{Z}_2||\tilde{Z}_c}\right) \\ \tilde{V}_i &= (\tilde{Z}_2\tilde{I}_2)\left(\frac{\tilde{Z}_2||\tilde{Z}_c + \tilde{Z}_1}{\tilde{Z}_2||\tilde{Z}_c}\right) \\ \frac{\tilde{I}_2(s)}{\tilde{V}_i(s)} &= \frac{\tilde{Z}_2||\tilde{Z}_c}{\tilde{Z}_2(\tilde{Z}_2||\tilde{Z}_c + \tilde{Z}_1)},\end{aligned}$$

For the principle of superposition the grid voltage is set to zero for the derivation of the transfer function. At the fundamental frequency $\tilde{V}_g = 230\sqrt{2}\angle 0°$ and $\tilde{I}_2 = 20\sqrt{2}\angle 0°$:

$$\tilde{V}_x = \tilde{V}_g + \tilde{Z}_2\tilde{I}_2 \tag{4.3.1}$$

$$\begin{aligned}\tilde{I}_x &= \frac{\tilde{V}_x}{\tilde{Z}_c} \\ &= \frac{\tilde{V}_g + \tilde{Z}_2\tilde{I}_2}{\tilde{Z}_c}\end{aligned} \tag{4.3.2}$$

$$\tilde{V}_i = \tilde{V}_x + \tilde{Z}_1(\tilde{I}_x + \tilde{I}_2) \tag{4.3.3}$$

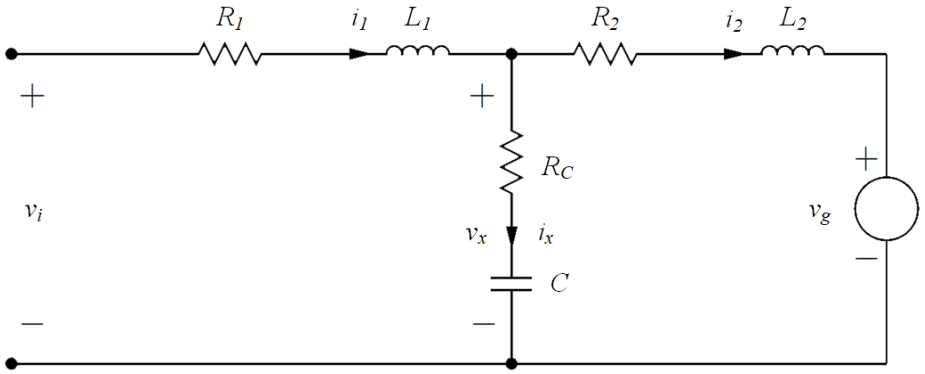

Figure 4.15: Per-phase model of the LCL-filter.

Substitute (4.3.1) and (4.3.2) into (4.3.3) to give:

$$\tilde{V}_i = (\tilde{V}_g + \tilde{Z}_2\tilde{I}_2) + \tilde{Z}_1\left(\frac{\tilde{V}_g + \tilde{Z}_2\tilde{I}_2}{\tilde{Z}_c} + \tilde{I}_2\right)$$

The amplitude modulation index can then be expressed as:

$$m_a = \frac{|\tilde{V}_i|}{\frac{V_D}{2}}$$

and the modulation angle as $\phi = \angle\tilde{V}_i$ which will serve as the angle of the PWM reference. The grid current can be derived as follows:

$$\begin{aligned}
\tilde{V}_i &= \tilde{Z}_1\tilde{I}_1 + (\tilde{Z}_2\tilde{I}_2 + \tilde{V}_g) \\
&= (\tilde{Z}_2\tilde{I}_2 + \tilde{V}_g)\left[\frac{\tilde{Z}_1}{\tilde{Z}_2||\tilde{Z}_c}\right] + (\tilde{Z}_2\tilde{I}_2 + \tilde{V}_g) \\
\tilde{I}_2 &= \frac{\tilde{V}_g\left[\frac{\tilde{Z}_1}{\tilde{Z}_2||\tilde{Z}_c} + 1\right] - \tilde{V}_i}{-\tilde{Z}_2\left[\frac{\tilde{Z}_1}{\tilde{Z}_2||\tilde{Z}_c} + 1\right]}
\end{aligned} \tag{4.3.4}$$

For the first case $\tilde{V}_g = 0$ and $\tilde{V}_i = jm_a\frac{V_D}{2}e^{j\phi}$ are substituted into (4.3.4) to give $\tilde{I}_{2A}$. To calculate $\tilde{I}_{2B}$, $\tilde{V}_g = 230V$ and $\tilde{V}_i = 0$ is substituted. The two grid currents that result from each individual voltage source's effect is summed as phasors to give the total grid current at 50 Hz:

$$I_2 = |\tilde{I}_{2A} + \tilde{I}_{2B}|$$

to obtain the amplitudes of the grid-side current's harmonics at the frequencies $mf_{sw} + nf_1$:

$$I_2(s) = \left|V_i(s)\left(\frac{I_2}{(}s)V_i(s)\right)\right|.$$

The Fourier series expansion of the output voltage from the inverter can be expressed as follows [15]:

$$\begin{aligned}
v_i(t) = &\frac{1}{2}A_{00} + \sum_{n=1}^{\infty}\left[A_{0n}\cos(n\omega_1 t) + B_{0n}\sin(n\omega_1 t)\right] \\
&+ \sum_{m=1}^{\infty}\left[A_{m0}\cos(m\omega_s t) + B_{m0}\sin(m\omega_s t)\right] \\
&+ \sum_{m=1}^{\infty}\sum_{n=\pm1}^{\pm\infty}\left[A_{mn}\cos(m\omega_s t + n\omega_1 t) + B_{mn}\sin(m\omega_s t + n\omega_1 t)\right],
\end{aligned}$$

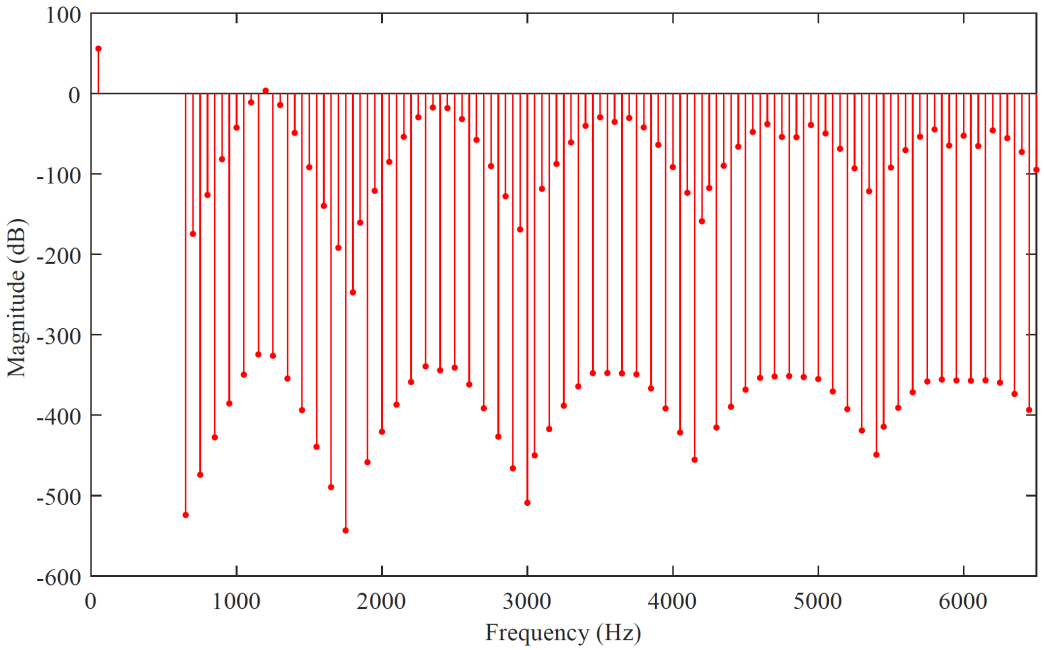

Figure 4.16: Output current spectrum of the a-phase (PWM).

where $\omega_1 = 2\pi f_1$, $\omega_s = 2\pi f_{sw}$ and m represents the integer multiples of the switching frequency around which the harmonics are grouped in fundamental frequency multiples represented by n. The frequency at which the harmonic is located is $mf_{sw} + nf_1$ and its amplitude is $|A_{mn} + jB_{mn}|$ where [15]:

$$A_{mn} + jB_{mn} = \frac{V_D}{jm\pi} J_n\left(\frac{m\pi m_a}{2}\right) e^{jn\pi}\left(1 - (-1)^n e^{jm\pi}\right)$$

More detail on the Bessel function $J_n(x)$ is provided in Appendix A.1.

In Figure 4.16 the grid-side current spectrum produced by the PWM converter is shown. For this three-phase system the triplen harmonics are eliminated. Here the characteristic harmonic grouping around multiples of the switching frequency can be seen.

4.3.2 Space vector modulation

Space vector modulation (SVM) is a form of PWM that was introduced in the 1980s [81]. It uses an alternative way of determining the pulse widths for the switching sequence based on the knowledge that a two-level three-phase converter has eight possible switching combinations that are identified as eight space vectors. Naturally sampled double-edge SVM uses a triangular carrier signal which is compared to a space vector modulation signal to generate the switching sequence. A sinusoidal modulation signal with the modulation index

m_a as amplitude and the modulation angle ϕ added to the phase:

$$\boldsymbol{i}^*_{abc} = m_a \begin{bmatrix} \sin(2\pi ft + \phi) \\ \sin(2\pi ft + \phi - \frac{2\pi}{3}) \\ \sin(2\pi ft + \phi - \frac{4\pi}{3}) \end{bmatrix}$$

is modified to generate the space-vector equivalent modulation waveform [81]:

$$\boldsymbol{i}^*_{mod} = \boldsymbol{i}^*_{abc} - \frac{1}{2}(max(\boldsymbol{i}^*_{abc}) + min(\boldsymbol{i}^*_{abc}))$$

In Figure 4.17 the space-vector modulation waveform is compared to the triangular carrier signal. For instance, intervals where the instantaneous value of the modulation waveform is greater than the carrier signal, the switch state is set to $u = 1$. In the opposite case the switch state becomes $u = -1$, as can be seen in Figure 4.18.

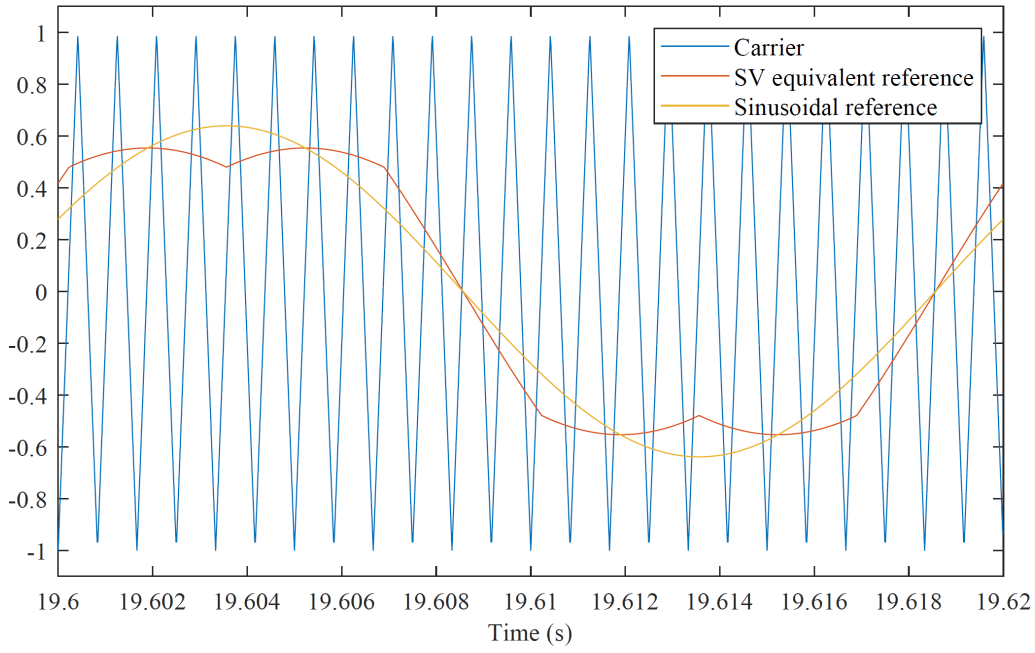

Figure 4.17: Triangular carrier, space-vector modulation signal and sinusoidal waveform generated to determine the switching pulse widths.

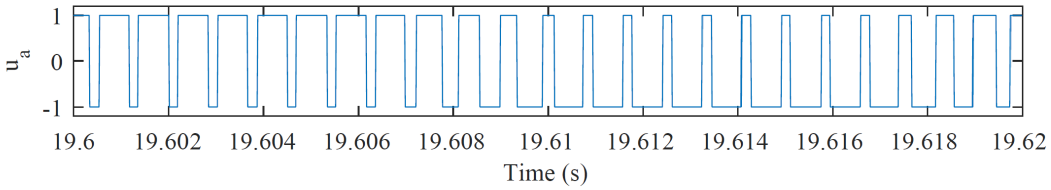

Figure 4.18: Space-vector modulated switching pulses.

The frequency at which the harmonic is located is $mf_{sw} + nf_1$ and its amplitude is $|A_{mn} + jB_{mn}|$ where

$$A_{0n} + jB_{0n}|_{n>1} = \frac{\sqrt{3}m_a V_D}{\pi} \left(\begin{array}{l} \frac{1}{n+1} \left[\begin{array}{l} \sin\left([n+1]\frac{\pi}{6}\right) \cos\left([n+1]\frac{\pi}{2}\right) \\ \times \left\{ \sqrt{3} + 2\cos\left([n+1]\frac{\pi}{3} + \frac{\pi}{6}\right) \right\} \end{array} \right] \\ \\ + \frac{1}{n-1} \left[\begin{array}{l} \sin\left([n-1]\frac{\pi}{6}\right) \cos\left([n-1]\frac{\pi}{2}\right) \\ \times \left\{ \sqrt{3} + 2\cos\left([n-1]\frac{\pi}{3} - \frac{\pi}{6}\right) \right\} \end{array} \right] \end{array} \right)$$

for the baseband harmonics ($m = 0,\ n > 1$) [81]. More detail is provided on the Bessel function $J_n(x)$ in Appendix A.1. In the case of the carrier harmonics ($m > 0,\ n = 0$) and sideband harmonics ($m > 0,\ n \neq 0$) the next equation is used to determine the harmonic amplitudes [81]:

$$A_{mn} + jB_{mn} = \frac{8V_D}{m\pi^2} \left(\begin{array}{l} \frac{\pi}{6} \sin\left([m+n]\frac{\pi}{2}\right) \left\{ J_n\left(m\frac{3\pi}{4}m_a\right) + 2\cos n\frac{\pi}{6} J_n\left(m\frac{\sqrt{3}\pi}{4}m_a\right) \right\} \\ \\ + \frac{1}{n} \sin m\frac{\pi}{2} \cos n\frac{\pi}{2} \sin n\frac{\pi}{6} \left\{ J_0\left(m\frac{3\pi}{4}m_a\right) - J_0\left(m\frac{\sqrt{3}\pi}{4}m_a\right) \right\} \Big|_{n\neq 0} \\ \\ + \sum_{\substack{k=1 \\ k\neq -n}}^{\infty} \left[\begin{array}{l} \frac{1}{[n+k]} \sin\left([m+k]\frac{\pi}{2}\right) \cos\left([n+k]\frac{\pi}{2}\right) \sin\left([n+k]\frac{\pi}{6}\right) \\ \times \left\{ J_k\left(m\frac{3\pi}{4}m_a\right) + 2\cos\left([2n+3k]\frac{\pi}{6}\right) J_k\left(m\frac{\sqrt{3}\pi}{4}m_a\right) \right\} \end{array} \right] \\ \\ + \sum_{\substack{k=1 \\ k\neq n}}^{\infty} \left[\begin{array}{l} \frac{1}{[n-k]} \sin\left([m+k]\frac{\pi}{2}\right) \cos\left([n-k]\frac{\pi}{2}\right) \sin\left([n-k]\frac{\pi}{6}\right) \\ \times \left\{ J_k\left(m\frac{3\pi}{4}m_a\right) + 2\cos\left([2n-3k]\frac{\pi}{6}\right) J_k\left(m\frac{\sqrt{3}\pi}{4}m_a\right) \right\} \end{array} \right] \end{array} \right)$$

Figure 4.19 provides the spectrum of the converter's space-vector modulated grid-side current. In three-phase systems the triplen harmonics are eliminated. It can be seen that the harmonic content is concentrated around multiples of the switching frequency, which is $f_{sw} = 1.2$ kHz in this case.

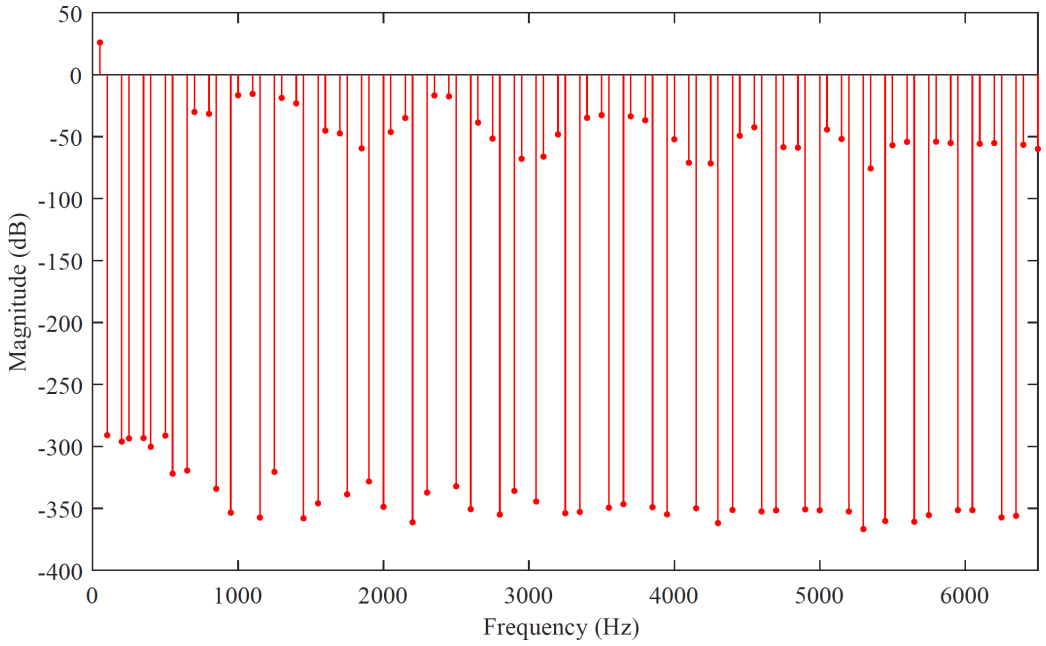

Figure 4.19: Output current spectrum obtained from space vector modulation.

4.4 Performance evaluation and comparison

The suitability of the developed control approach is evaluated by comparing the four control scenarios (MPC with a short horison of $N = 1$, MPC with a long horison of $N = 12$, open-loop PWM-based control and naturally-sampled SVM) with a focus on compliance to the grid-code harmonic limits. These control scenarios are evaluated at both a low switching frequency and a high switching frequency. For the first set of results, all control approaches are evaluated at a switching frequency of 1.2 kHz while a sampling interval of $T_s = 40\mu$s is applied, equivalent to a sampling frequency of 25 kHz. The second set is obtained with a switching frequency of 10.3 kHz, with a sampling interval of $T_s = 20\mu$s, doubling the sampling frequency to 50 kHz. The steady-state response is observed at about $t = 10$s, and is shown over one 50 Hz fundamental period. Each result includes the a-phase grid-side current and its reference, corresponding switching sequence and performance against the harmonic limits. Each spectrum is calculated from 200 steady-state fundamental periods.

4.4.1 Performance at a low switching frequency

The results of the first set of simulations are presented in Figure 4.20 (MPC with short horison), Figure 4.21 (MPC with long horison), Figure 4.22 (naturally sampled open-loop PWM) and Figure 4.23 (naturally sampled SVM). Each of the four control approaches is adjusted to have a switching frequency of approximately 1.2 kHz. To achieve this for the N=1 and N=12

cases, the weighting factor in the cost function was adjusted to $\lambda_u = 0.8$ and $\lambda_u = 2$ respectively. For PWM and SVM the switching frequency is directly specified beforehand as $f_{sw} = 1.2$ kHz. The pulse-width modulated switching sequence shown in Figure 4.22b, and the space vector modulated sequence in Figure 4.23b is generated according to this switching frequency and remains constant for every fundamental period. This differs from MPC where the switching sequence varies throughout the simulation and the switching frequency is not fixed or constant. The switching frequency is therefore determined as an average and is limited to be $f_{sw} < f_s/2$, less than half the sampling frequency but not equal, as the controller does not change the switch state during every single sampling instant.

A prediction horison of twelve time steps spans 480μs ahead of the current position in time, as opposed to the single 40μs time step. This enables the long-horison approach to anticipate a better trade-off between the objectives of switching reduction and reference tracking. Table 4.2 provides the tracking error of the fundamental 50 Hz component $I_2(f_1)$ for these approaches, calculated as follows using the amplitude of the reference current and the harmonic amplitude at f_1 obtained from the fft of the grid current:

$$tracking\ error \quad = \quad \left(\frac{I_2(f_1) \ - \ I_{2\ ref}}{I_{2\ ref}} \right) \times 100\%$$

The tracking errors for the short- and long-horison MPC approaches are 1.74% and 0.53% respectively. This verifies that long-horison control provides an optimised trade-off between control objectives by improving the tracking of the fundamental component with the same number of switching transitions taking place. There is no tracking error provided for the open-loop PWM and naturally-sampled SVM as the reference is calculated so that the tracking error of the fundamental component is zero.

It is also seen that long-horison MPC offers lower total harmonic distortion (THD) than short-horison control with a THD of 2.3% versus 3.36% respectively, much less than the 7.93% and 5.03% distortion resulting from PWM and SVM. This can be observed as the grid-current i_{2a} in Figure 4.21a has smaller ripple for the same number of switching transitions when controlled by MPC with the long prediction horison than with the short-horison control in Figure 4.20a. The largest ripple is observed in the PWM-controlled output current in Figure 4.22a.

The South African NRS 079-2-1:2010 grid code [16] places limits on the grid-current harmonic distortion at multiples of the fundamental frequency. These limits are expressed in terms of the harmonic amplitudes as percentages of the fundamental component and are provided in Appendix A.2.

With classic control schemes such as PWM, the resulting spectrum consists of discrete spectral lines grouped around multiples of the switching- or carrier frequency. In Figure 4.22c the spectral content present around the 24th harmonic multiple of the fundamental frequency, equivalent to the first

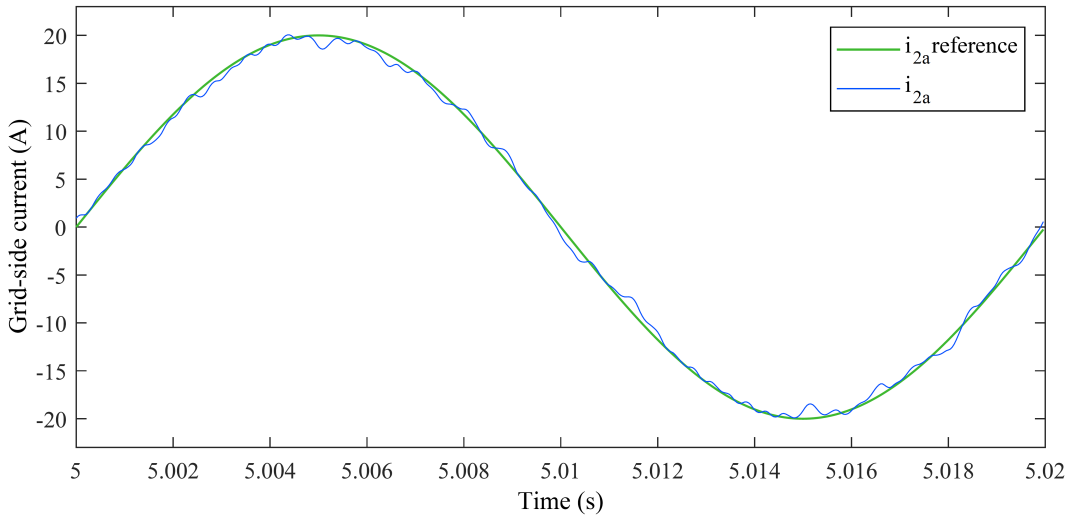

(a) Grid-side current and reference

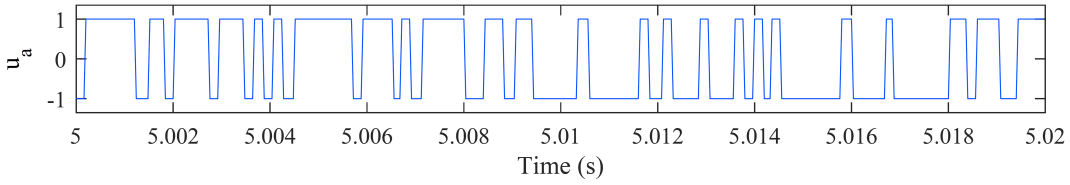

(b) Switching sequence

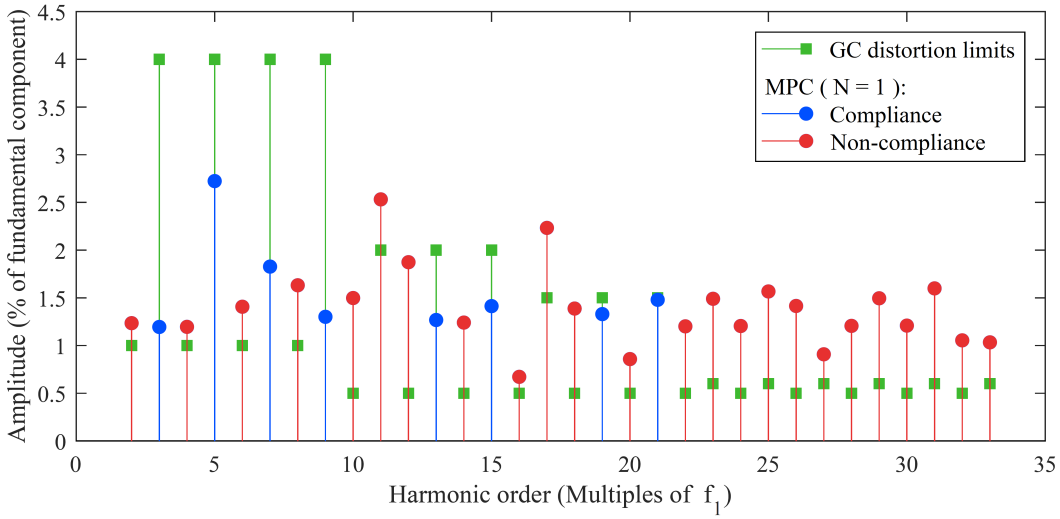

(c) Grid-side current harmonics compared to grid-code harmonic distortion limits

Figure 4.20: Results for the MPC short-horison (N = 1) case at $f_{sw} = 1.2$ kHz.

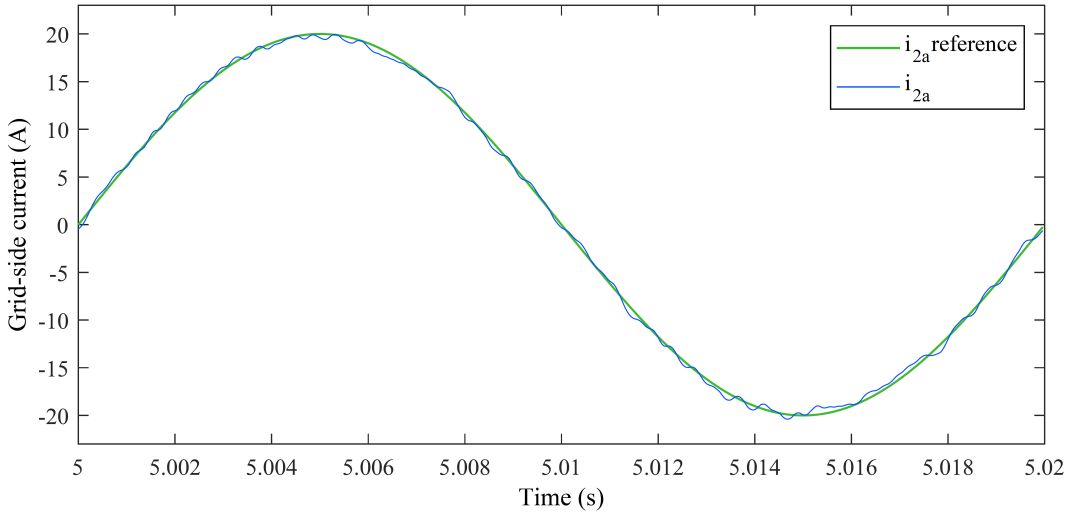

(a) Grid-side current and reference

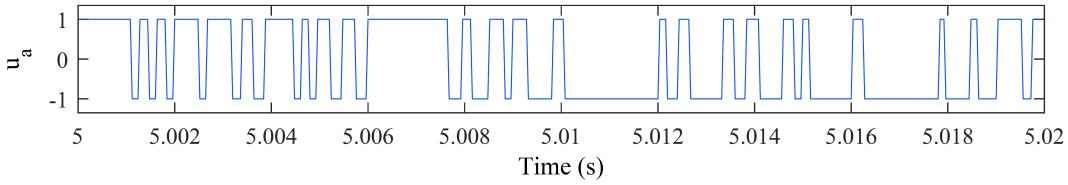

(b) Switching sequence

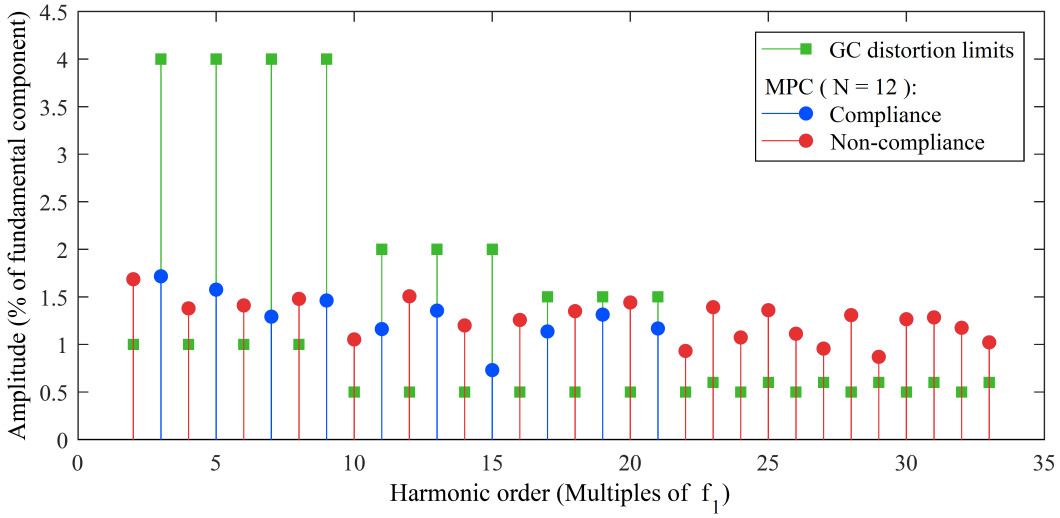

(c) Grid-side current harmonics compared to grid-code harmonic distortion limits

Figure 4.21: Results for the MPC long-horison (N = 12) case at $f_{sw} = 1.2$ kHz.

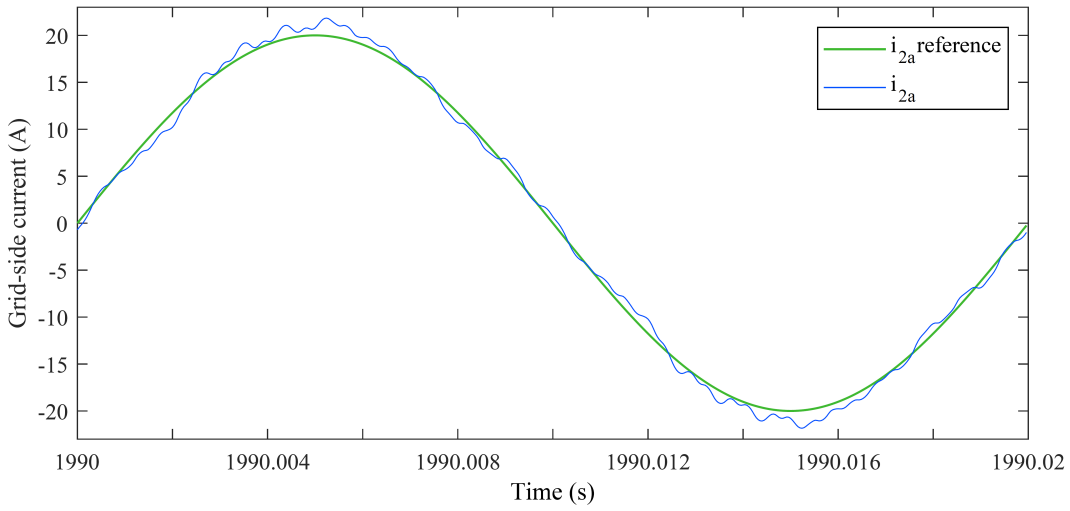

(a) Grid-side current and reference

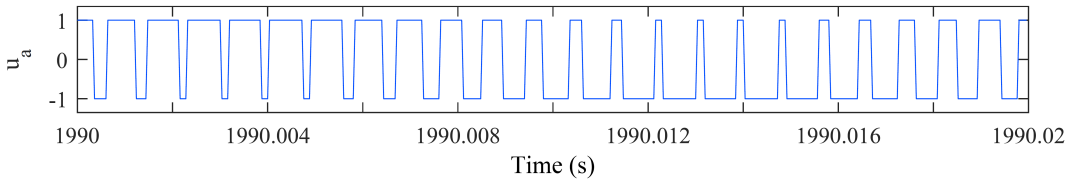

(b) Switching sequence

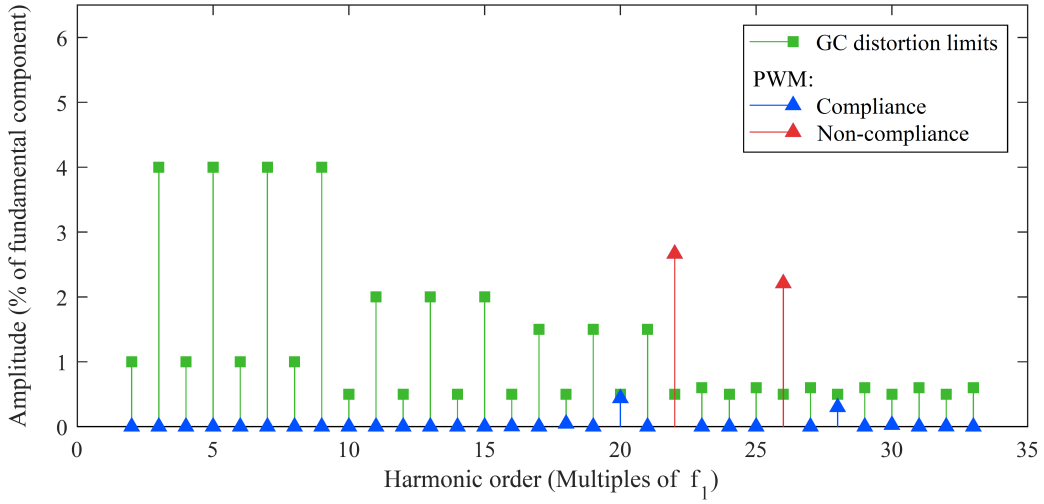

(c) Grid-side current harmonics compared to grid-code harmonic distortion limits

Figure 4.22: Results for the PWM case at $f_{sw} = 1.2$ kHz.

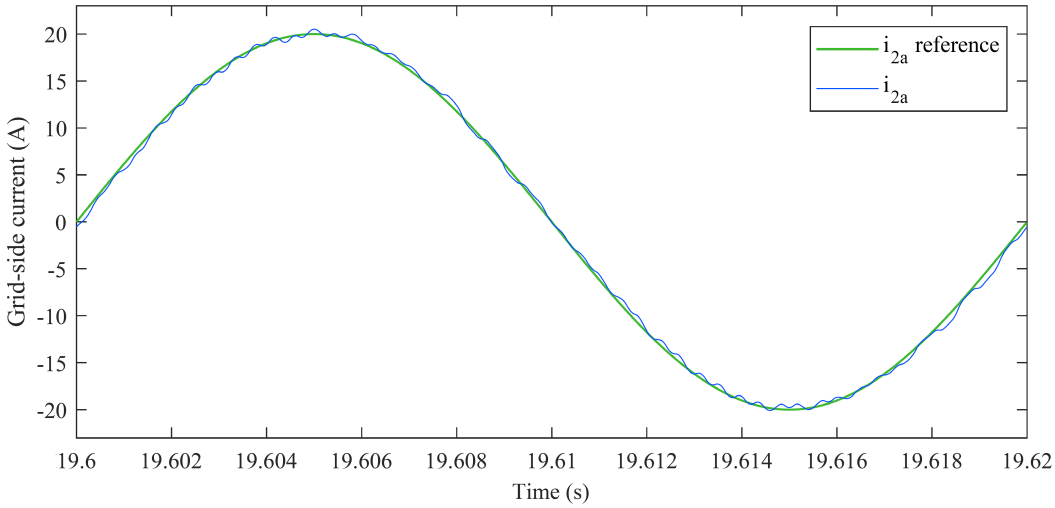

(a) Grid-side current and reference

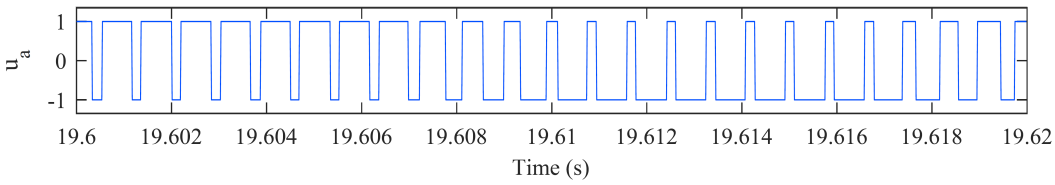

(b) Switching sequence

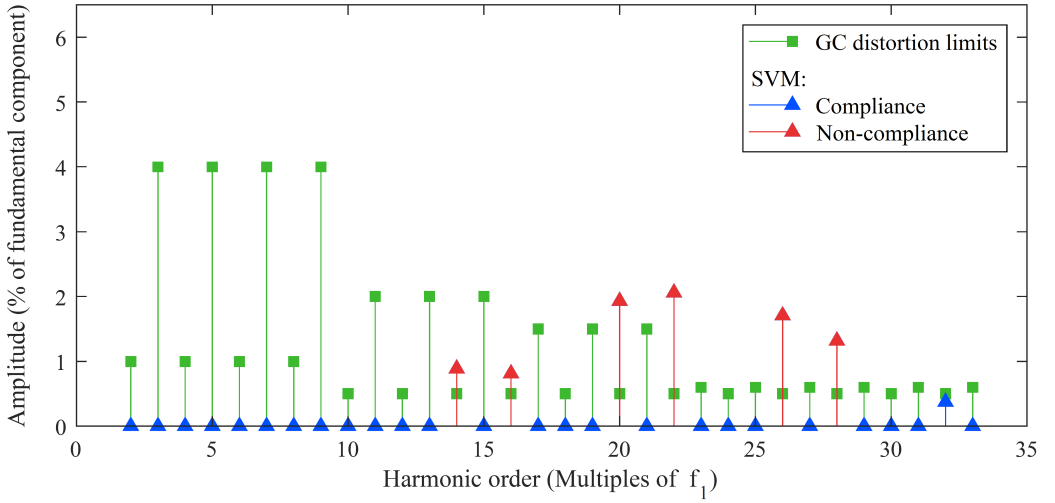

(c) Grid-side current harmonics compared to grid-code harmonic distortion limits

Figure 4.23: Results for the SVM case at $f_{sw} = 1.2$ kHz.

Table 4.2: Summary of the simulation results

Approach	Weighting factor λ_u	Tracking error	THD	Grid-code compliance
$T_s = 40\mu$s, f_{sw}=1.2 kHz:				
MPC (N=1)	0.8	1.74%	3.36%	No
MPC (N=12)	2	0.53%	2.30%	No
PWM	-	-	7.93%	No
SVM	-	-	5.03%	No
$T_s = 20\mu$s, f_{sw}=10.3 kHz:				
MPC (N=1)	6×10^{-4}	0.12%	0.27%	No
MPC (N=12)	6×10^{-7}	0.03%	0.19%	Yes
PWM	-	-	0.87%	Yes
SVM	-	-	0.56%	Yes

multiple of the switching frequency, exceeds the harmonic limits on the 22nd and 26th harmonics, bearing in mind the absence of the triplen harmonics in a three-phase system as discussed earlier. With SVM a similar trend is observed in Figure 4.23c, but with more widely spread harmonic content at even harmonic positions around the switching frequency, except at the triplen harmonics.

Model predictive control results in the spread of spectral content but still shows a very slight concentration of content around multiples of the switching frequency. Due to some of the switching energy being converted to noise, the energy is summed in 50 Hz frequency bands to obtain the discrete harmonic amplitudes at multiples of the fundamental frequency f_1. The harmonic distortion resulting from the long-horison approach, Figure 4.21c, is slightly lower than from the short-horison approach in Figure 4.20c, but both exceed the limits on all higher-order harmonics: those surrounding the switching frequency (24th harmonic) and higher. Furthermore, both approaches also violate restrictions on all the even harmonics in the lower-order range, with the short-horisons approach exceeding limits on a few odd harmonics as well.

4.4.2 Performance at a high switching frequency

During the second set of results the performance of the four approaches (short-horison MPC in Figure 4.24; long-horison MPC in Figure 4.25; open-loop PWM in Figure 4.26) and naturally-sampled SVM in Figure 4.27) are investigated at a higher switching frequency of $f_{sw} = 10.3$ kHz and a sampling frequency of $f_s = 50$ kHz. The weighting factor was adjusted to $\lambda_u = 6{\times}10^{-4}$ and $\lambda_u = 6{\times}10^{-7}$ for the short- and long-horison cases respectively.

From Table 4.2 it is seen once more that MPC with long horisons outperforms MPC with short horisons through a lower tracking error and

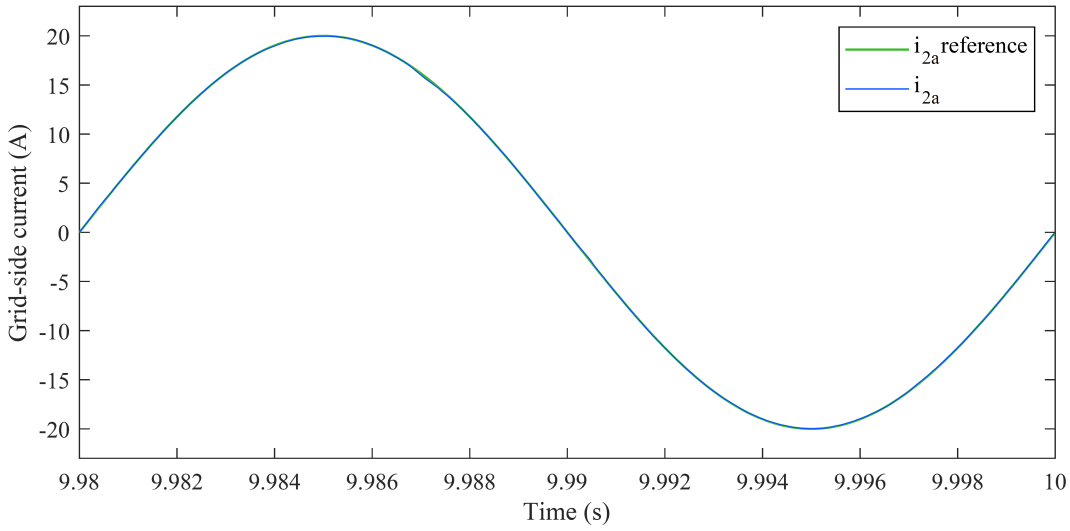

(a) Grid-side current and reference

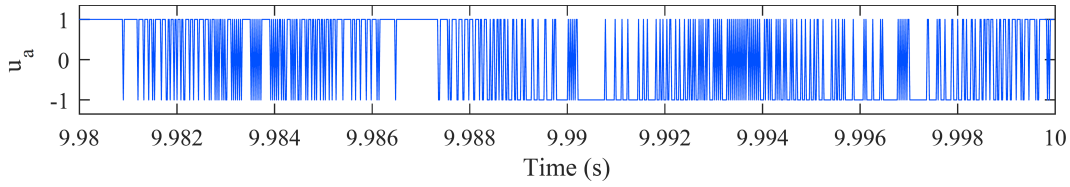

(b) Switching sequence

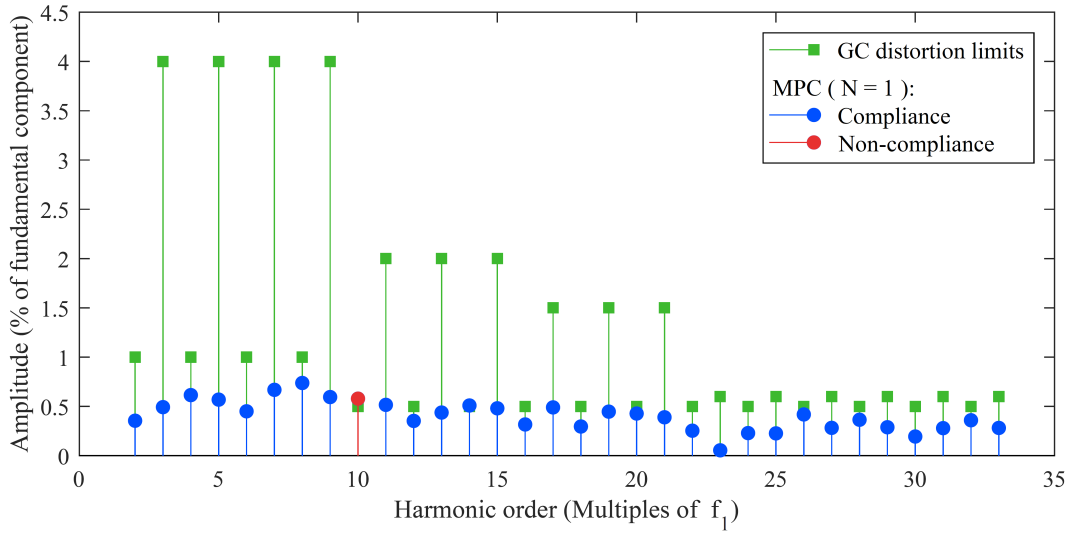

(c) Grid-side current harmonics compared to grid-code harmonic distortion limits

Figure 4.24: Results for the MPC short-horison (N = 1) case at $f_{sw} = 10.3$ kHz.

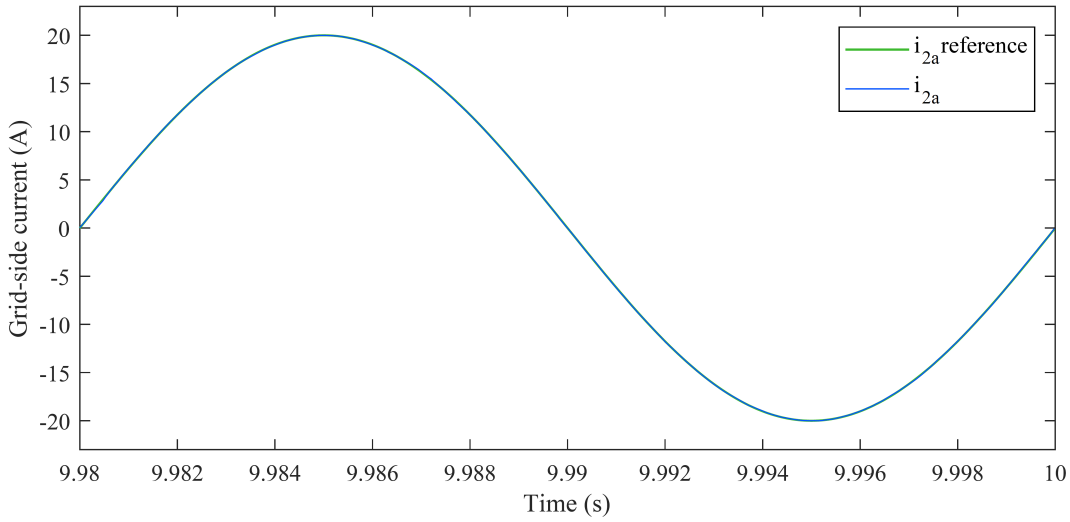

(a) Grid-side current and reference

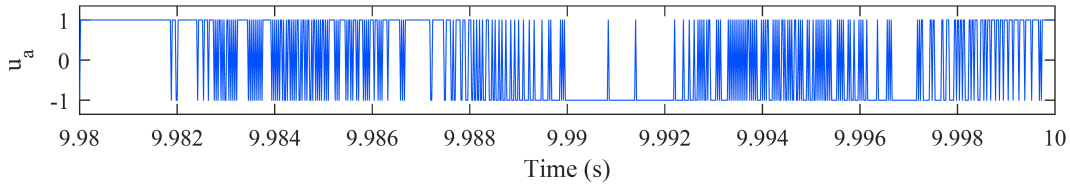

(b) Switching sequence

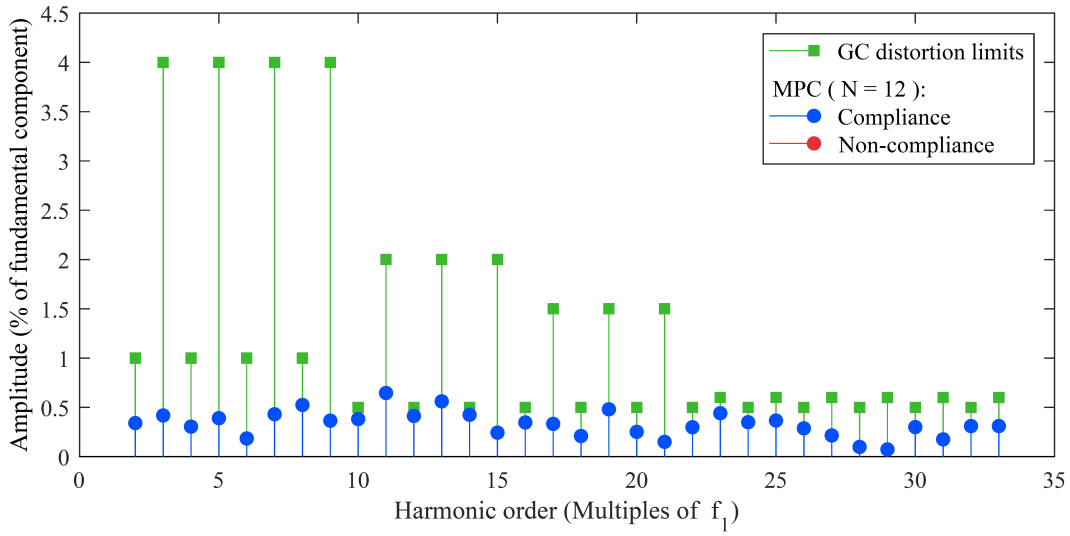

(c) Grid-side current harmonics compared to grid-code harmonic distortion limits

Figure 4.25: Results for the MPC long-horison (N = 12) case at $f_{sw} = 10.3$ kHz.

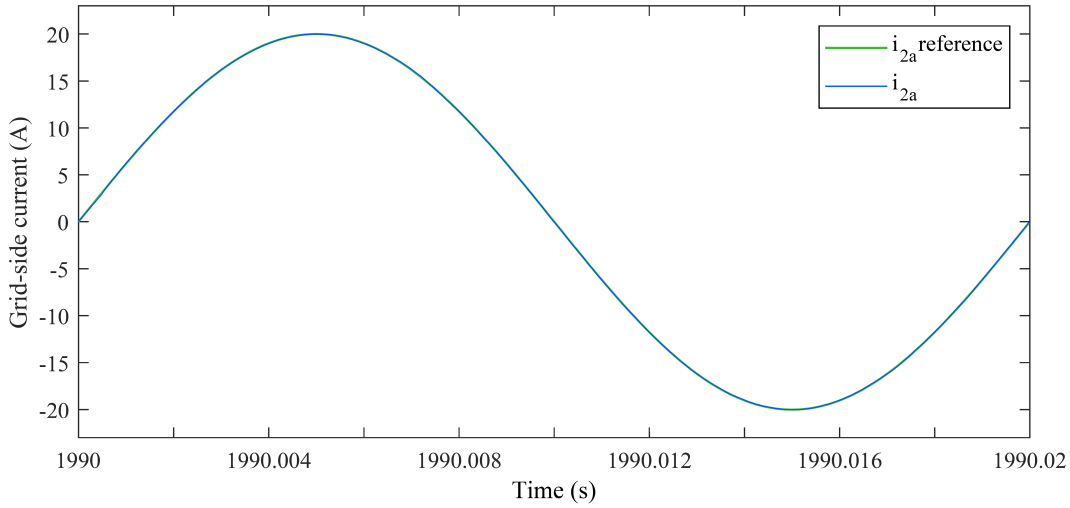

(a) Grid-side current and reference

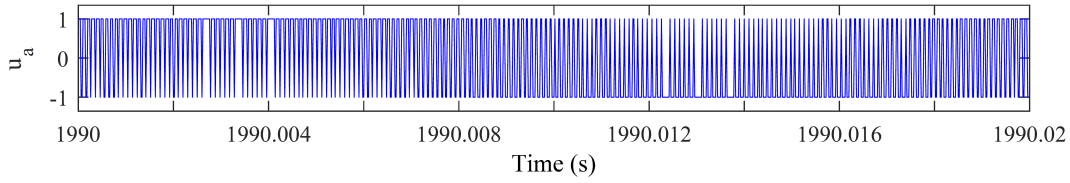

(b) Switching sequence

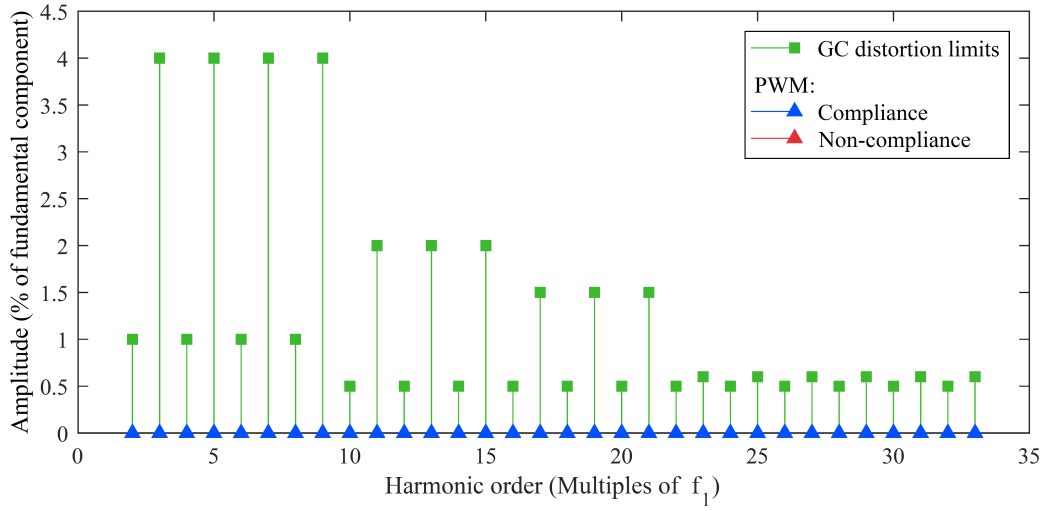

(c) Grid-side current harmonics compared to grid-code harmonic distortion limits

Figure 4.26: Results for the PWM case at $f_{sw} = 10.3$ kHz.

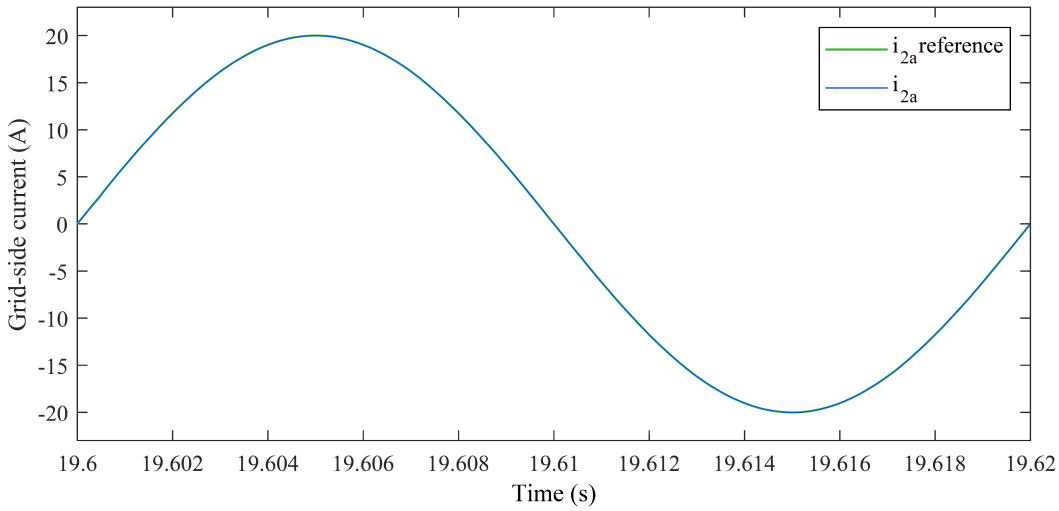

(a) Grid-side current and reference

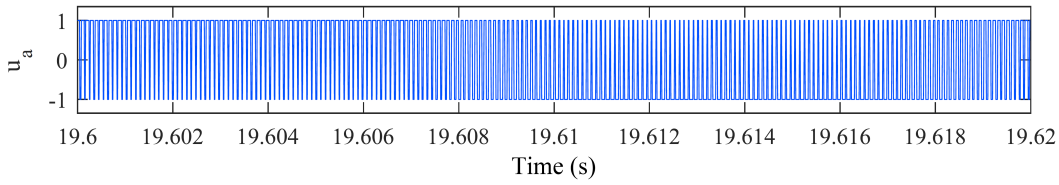

(b) Switching sequence

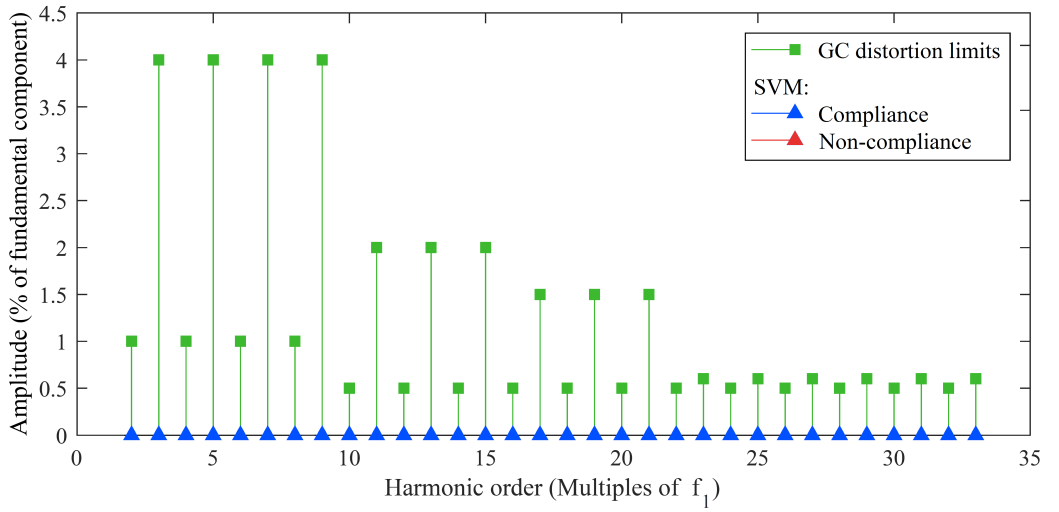

(c) Grid-side current harmonics compared to grid-code harmonic distortion limits

Figure 4.27: Results for the SVM case at $f_{sw} = 10.3$ kHz.

THD percentage. Both the tracking error and THD are much lower at a high switching frequency than those obtained at the low switching frequency. The grid-side currents for all four scenarios are smooth with no noticeable ripple.

MPC with long horisons, PWM and SVM manage to perform within the grid-code current-distortion limits. The grid-current spectrum produced by MPC with a short horison adheres to all harmonic limits, except at the tenth harmonic (500 Hz). This coincides with the resonant frequencies of the LCL-filter [14]:

$$f_{res1} = \frac{1}{2\pi\sqrt{CL_2}} \qquad \text{and} \qquad f_{res2} = \frac{1}{2\pi\sqrt{C\dfrac{L_1L_2}{L_1+L_2}}},$$

which delivers $f_{res1} = 493$ Hz and $f_{res2} = 512$ Hz when substituting the filter's component values, provided in Table 4.1, into the equations. Through the application of a longer prediction horison the MPC controller manages to displace enough energy away from the filter's resonant frequencies at the tenth harmonic to fully comply with the harmonic distortion limits. This eliminates the need for active damping (AD) of filter resonance (e.g.: through virtual resistance (VR)-based approaches [63; 82; 48; 47]) as required by linear controllers which make use of classic control techniques.

4.5 Summary

Figure 4.28 provides a glance on how this chapter relates to those that surround it. This chapter provides the evaluation of the model-predictive direct current-control strategy developed in Chapter 3, for a three-phase grid-connected converter with LCL-filter by implementation in a MATLAB-based simulation for evaluation. A sphere decoding algorithm was implemented as a computationally efficient solver for the solution search. The model shows correct functioning as current controller, fast transient response and good reference tracking of the fundamental 50 Hz component. The suitability of the current-control scheme for a grid-connected converter setup was investigated by comparing it with open-loop PWM, naturally-sampled SVM, as well as the short- and long-horison application of the developed MPC scheme. The spectrum of the grid-side current was tested against the harmonic distortion limits of the NRS 079-2-1:2010 grid code for current injected into the grid. The evaluation was performed at both a low and a high switching frequency.

At low frequencies both MPC with short- and long-horison approaches show non-compliance with the harmonic limits in the higher frequency range around the switching frequency and onwards, as well as limits at even harmonics in the lower frequency range. With an increase in switching frequency a point is reached where the method manages to comply with the grid-code harmonic

requirements, but this is at a much higher switching frequency than the range that is ideally intended for MPC to leverage its benefits from long horisons. One way the to reduce the switching frequency at which the controller functions satisfactorily is to adjust or re-design the filter parameters.

MPC utilising long prediction horisons is able to anticipate future effects of actuations and plan further in advance. From the results it was confirmed that MPC with long horisons provides a more optimal trade-off between the two control objectives, reference tracking and switching reduction, than MPC with short horisons as it delivered better reference tracking and lower total harmonic distortion. It was also observed that long-horison control automatically attenuates the filter resonance to an acceptable level that fully complies with the grid code, eliminating the need for active damping techniques used with linear controllers.

At high switching frequency it is clear that the method is currently outperformed by PWM and SVM. Despite the control approach's current inadequacies, there is room for improvement through future research regarding harmonic performance.

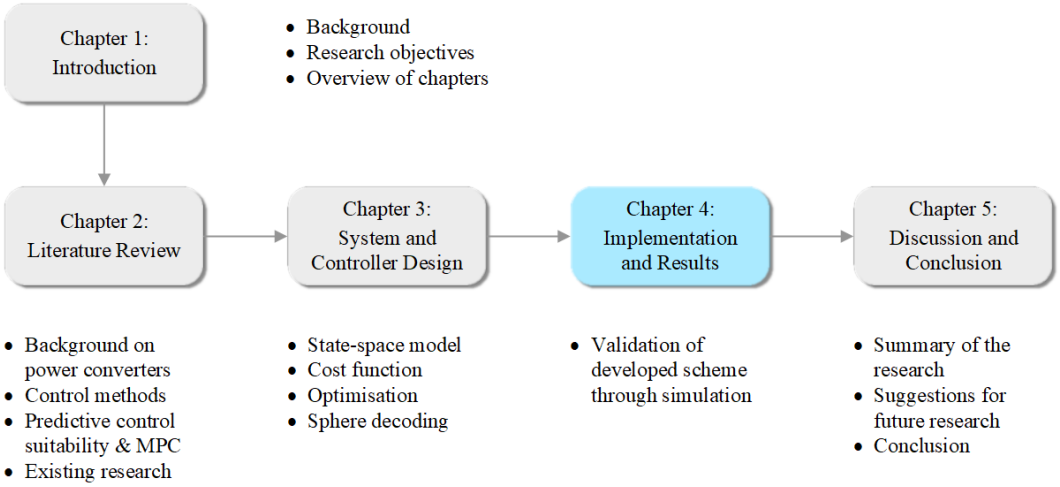

Figure 4.28: Brief overview of the thesis chapters.

Chapter 5

Discussion and Conclusion

In this chapter a summary is given of the whole thesis and how the research objectives were met, where-after the main findings and recommendations for future research are made before the final conclusion is drawn.

5.1 Summary of the research

The focus of the research is the development and evaluation of a MPC current-control strategy for a three-phase grid-connected converter with LCL-filter. All of the research objectives were achieved during the study:

- A discrete-time state space model was derived that describes the grid-tied converter.
- The optimisation approach for MPC with long horisons as described in [46] was adapted and extended to incorporate the grid voltage.
- The following control objectives were incorporated into the cost function:
  - To minimise current tracking error.
  - To minimise switching frequency.
- A sphere decoding algorithm was described and implemented as a recursive function that solved the optimisation problem in a computationally efficient manner.
- The developed control approach was implemented and evaluated by MATLAB-based simulations.

A review follows on each chapter to summarise the main points that were addressed in the thesis and how they support the objectives of the study.

5.1.1 Chapter 1

The first chapter introduced the background and context of the research, stated the main focus and objectives of the thesis and provided a roadmap of the thesis chapters.

5.1.2 Chapter 2

A literature review was conducted to provide an understanding of and background on the history and applications of power converters. A classification and discussion was provided on the types of control methods that are applied to power converters, followed by a discussion on the suitability of predictive control methods to present-day control systems and power converters. The specific types of predictive control methods and specifically model predictive control (MPC), its benefits, drawbacks and basic concepts, were discussed. A review was done on existing research relevant to model predictive control of grid-tied converters.

5.1.3 Chapter 3

In Chapter 3 the three-phase system and the proposed controller are described and developed mathematically by defining the constraints of the finite control set regarding the integer switch states, and deriving a state-space model that can be used to describe and predict the behaviour of the system according to its inputs, hereby achieving the first objective.

This model differs from that developed in [46] as within the state-space equation the grid voltage is considered as an additional input vector alongside the switch-state input vector, rather than being included in the state vector as is the general trend in [47; 48]. This meant that the algebra of the standard MPC optimisation approach be reworked to accommodate the inclusion of the grid voltage as an input vector and this achieved the second objective of the research.

For the third objective a cost function was formulated to include two weighted control objectives, namely reducing reference tracking error and secondly switching frequency reduction as a means to reduce losses in the converter. This cost function was used to evaluate the optimality of available switching actions, as the option that minimises the cost is the most optimal. The state-space equation was used to predict the future behaviour of the system according to a specific sequence of switching states applied. The cost of each switch action was summed over the prediction horison of N time steps to give the overall cost of a specific switching-sequence. The number of possible sequences and their predicted outcomes increased exponentially the longer the chosen horison length, posing an exhaustive search computationally if every available sequence was to be evaluated. The minimisation of the

cost function was rewritten to become an integer least-squares (ILS) problem with the switching sequence vector $\boldsymbol{U}(k)$ as the optimisation variable, and a transformation matrix $\boldsymbol{H}$ necessary to generate the discrete solutions space wherein all candidate solutions $\boldsymbol{U}(k)$ were mapped.

In fulfilment of the fourth objective sphere decoding was incorporated as an efficient solver of the ILS-problem at a long prediction horison that inherently has an exponentially enlarging/extending set of candidate solutions. The sphere decoder approaches the ILS-problem as a minimisation of the Euclidean distance between its central point (position of the unconstrained solution) and candidate solutions in the solution space. The closer the solution lies to the sphere's center, the more optimal it is. A Babai estimate of what the most optimal solution might be is used as the starting point of the search to exclude as many sub-optimal solution points from the search as possible. As the sphere decoder explores the nodes of the search tree, it either prunes the branch if its Euclidean distance falls outside of the sphere's radius, or advances along the branch to the next node to repeat the evaluation. Once it reaches a complete set of actuations at the bottom of the tree that fall within the radius, it considers it as a new temporary optima and tightens the radius to that candidate's distance from the sphere's center. The decoder proceeds in this manner until only one candidate remains in the sphere, which is then selected as the official optimal solution.

5.1.4 Chapter 4

In the fourth chapter the fifth objective which entails the implementation and evaluation of the MPC control scheme for the three-phase grid-connected converter with LCL-filter is addressed. The first part of the chapter describes how the mathematical model developed in Chapter 3 was implemented in a MATLAB-based simulation. A flow diagram is used to describe the logical flow within the main function script that simulates the grid-connected converter with LCL-filter and how control is performed by the MPC strategy. An algorithm is formulated to perform the sphere decoding from program code and is implemented as a recursive function written in a separate MATLAB script and called from within the main MPC function to perform the optimised search. The efficiency of the sphere decoder is evaluated by counting the number of floating point operations (FLOPS) performed during the solution search and comparing them to the FLOPS performed during an exhaustive search at different prediction horison lengths N. The use of the sphere decoder enables a horison length of $N = 15$ to be used during the simulation, whereas the exhaustive search limited the simulation to a prediction horison of $N = 8$ time steps due to its computational burden.

Sample output from the simulation, such as the capacitor voltage, inverter- and grid-side current waveforms, are investigated to verify that the MPC controller model and its implementation in the simulation was functioning

correctly. The dynamic response was also tested by insertion of a step in the reference amplitude, to which the controller adjusted very quickly. Thereafter an explanation was given on how the spectral content of the grid-side current was determined from the simulation's time-domain results to obtain the discrete harmonics and THD.

After the explanation of how the simulation was developed for the MPC and sphere decoder's implementation, detail regarding the implementation of an open-loop PWM controller and space vector modulator for the same three-phase grid-connected converter is given, such as generation of the modulated switching signals and calculation of the spectrum by using the Fourier series expansion and Bessel function.

In the second part of the chapter an evaluation is provided of the developed current control scheme through a comparison of the following control approaches: MPC with a short horison, MPC with a long horison, open-loop naturally-sampled PWM and SVM. These approaches were each evaluated at a low switching frequency and a high switching frequency. Attributes such as tracking error of the fundamental 50 Hz component and total harmonic distortion are also compared.

At low switching frequencies the developed MPC scheme exceeds a significant number of harmonic limits predominantly at even harmonics, thus not providing satisfactory performance according to the NRS 079-2-1:2010 grid-code current distortion limits. With an increase in switching frequency a point is reached where the long-horison approach manages to comply with the grid-code harmonic requirements, but this is at a much higher switching frequency than the range that is ideally intended for MPC to leverage the benefits of long horisons. A more detailed breakdown of the findings follows.

5.2 Main findings

The model and simulation developed of the MPC scheme functions correctly:

- The controller is able to track the fundamental 50 Hz component with accuracy.
- The controller has fast transient response as it reacts quickly to abrupt changes in the reference by fully adjusting within less than two milliseconds with little overshoot.

The sphere decoder was proven to provide a significant efficiency improvement over an exhaustive search approach.

MPC performs better using long-horison control than with short-horison control:

- Long-horison control automatically attenuates LCL-filter resonance present in short-horison control without the use of active damping techniques generally used in linear controllers. It is able to displace some of the switching energy away from the resonant frequencies of the LCL-filter.
- Long-horison control is able to anticipate and prepare for a inserted step in amplitude a number of time steps ahead due to its prediction horison spanning further into the future than in the short-horison case.
- Long-horison control shows smaller reference-tracking error when compared to short horisons when compared at the same switching frequency, it is therefore able to optimise the switching sequence to reduce tracking error using the same number of switching transitions.
- Long-horison control provides lower overall THD and smaller ripple in the grid-side current than short-horison control, open-loop PWM and SVM when compared at the same switching frequency.

Performance against the NRS 079-2-1:2010 grid code harmonic distortion limits and the traditional PWM-type approaches:

- It is observed that MPC produces less ripple in the grid-side current at both short and long horisons than PWM with the same switching frequency. PWM has a fixed switching frequency and pulse-width modulated switching sequence throughout, whereas MPC offers more flexibility of the switching frequency as it is able to constantly optimise and adapt the switching sequence to provide an optimal trade-off according to the desired control objectives and their priority weightings within the cost function.
- PWM and SVM approaches do not comply to the grid code harmonic limits when the switching frequency and its surrounding harmonic content falls within the range of the grid code (0 Hz - 1.7 kHz).
- At a low switching frequency MPC does not comply with the current distortion harmonic limits at even harmonics, nor at harmonics higher than the switching frequency.
- At a high switching frequency long-horison MPC is able to comply with the grid-code harmonic distortion limits, however short-horison control falls short of compliance to the harmonic limit at the filter resonance frequency.

5.3 Suggestions for future research

- Further work can be done on the control approach to improve the performance regarding even and higher-order harmonics in order to comply with the distortion limits of the grid code. [83] uses the concept of a spectrogram, which is the squared magnitude of the short-time Fourier transform (STFT). The MPC scheme applies spectrogram constraints to the output spectrum across multiple time steps of the prediction horison. Spectrogram MPC is able to enforce hard constraints on the spectrum, hereby differing from the frequency-weighted methods incorporated with MPC such as band-pass filters [84] and high-pass Butterworth filters [85], where the high frequency behaviour is penalised and fine-tuned in the cost function.

- Improvement in the design of the filter should be investigated. Switching at lower frequencies will require a larger filter, as a larger converter-side inductor reduces current ripple, and the larger the filter capacitor, the more current ripple goes through the capacitor instead of the utility network. The drawbacks related to these parameter adjustments are increased component size and cost. One way of reducing distortion could be to extend the LCL-filter, but this significantly increases the control complexity, could imply a larger input voltage requirement and increases the system cost.

- Further research can be done regarding the practical implementation of the controller for long horisons to restrict the computational time needed for each time step / sampling period. A reduction is needed from several minutes taken in simulation to the several microseconds needed in real time by a practical implementation.

5.4 Conclusion

During the research the suitability of a direct model predictive current control strategy for a three-phase grid-connected converter with LCL-filter was evaluated. The control objectives entailed minimising current-tracking error and switching frequency. The research contributed to knowledge creation in the field of model predictive control (MPC) in power electronics by extending on the work done in [46] by incorporating the grid voltage as an input vector in the mathematical model and optimisation approach.

A sphere decoder was incorporated in order to relieve the computational burden related to an exhaustive search, by improving the efficiency by which the simulation executes a solution search. This makes it possible to use long prediction horisons of up to fifteen time steps during the simulation approach.

The performance when using MPC with short horisons versus long horisons was investigated and compared to an open-loop pulse-width modulation controller, evaluated at both a low and high switching frequency. The developed controller provided accurate current-reference tracking and fast transient response for both short and long horisons, however it was noticed that long-horison control is clearly superior and automatically damps the resonant frequencies of the filter. At low switching frequencies the controlled grid-side current does however not fully comply with the harmonic distortion limits specified by the South African grid code. The odd harmonics are generally within the specified limits, but the even harmonics requires improvement. This strategy is therefore not suitable for grid-tied inverter applications, however future research can be done to develop methods to suppress the even and high-order harmonics. The use of longer horisons improves performance but there is an increased computational burden which is a barrier to simulation efforts and practical implementation.

In the past the adoption of MPC was limited by the computational abilities at the time, today it is possible to implement such a controller in simulation and perform predictions and optimisation over long horisons [10; 11; 46]. The increasing rate at which technology and computational power advances provides a prospect that the practical implementation of long-horison MPC controllers will become feasible in the near future.

Appendices

Appendix A

Additional Theory

A.1 Bessel function

Bessel function of the first type [15]:

$$J_n x = \frac{1}{2\pi}\int_{-\pi}^{\pi} e^{j(xsiny - ny)}dy$$

Characteristics:

$$\begin{aligned} J_n - x &= (-1)^n J_n(x) \\ J_{-n}(x) &= (-1)^n J_n(x) \end{aligned}$$

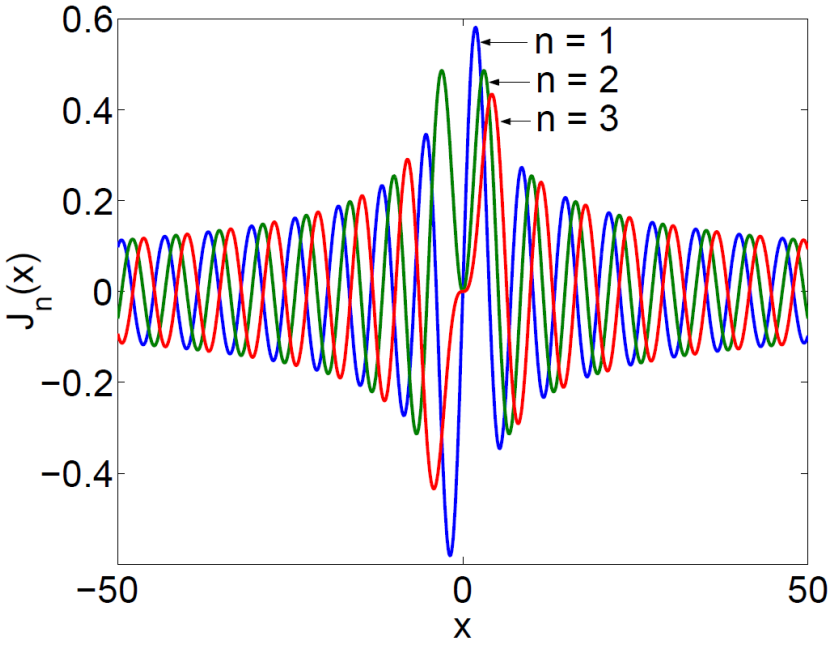

Figure A.1: Output of a first order Bessel function. [15].

A.2 Grid code

The NRS 097-2-1:2010 [16] currently serves as the grid code to facilitate the interconnection of renewable energy sources to the national utility grid in South Africa. Herein harmonic distortion limits are specified for current injected into the grid. Low current-distortion levels prevent harmful effects on other equipment connected to the grid. In accordance with the IEC 61727:2004 the individual harmonics have to comply with the percentages provided in Table A.1:

Table A.1: Current distortion limits according to harmonics [16].

Odd harmonics	**Distortion limit**
3^{rd} through 9^{th}	Less than 4.0%
11^{th} through 15^{th}	Less than 2.0%
17^{th} through 21^{st}	Less than 1.5%
23^{rd} through 33^{rd}	Less than 0.6%
Even harmonics	**Distortion limit**
2^{nd} through 8^{th}	Less than 1.0%
10^{th} through 32^{nd}	Less than 0.5%

List of References

[1] International Energy Agency and International Energy Agency Staff: *Electricity Information 2002: With 2001 Data*. IEA Statistics. OECD, International Energy Agency, 9 Rue de la Fédération, 75015 Paris, France, 2002. ISBN 978-92-64-19793-0.

[2] International Energy Agency and International Energy Agency Staff: *Electricity Information 2010: With 2009 Data*. IEA Statistics. OECD, International Energy Agency, 9 Rue de la Fédération, 75015 Paris, France, 2010. ISBN 978-92-64-08418-6.

[3] International Energy Agency and International Energy Agency Staff: *Electricity Information 2017: With 2016 Data*. IEA Statistics. OECD, International Energy Agency, 9 Rue de la Fédération, 75015 Paris, France, 2017. ISBN 978-92-64-27812-7.

[4] Walwyn, D. and Brent, A.: Renewable energy gathers steam in south africa. *Renewable and Sustainable Energy Reviews*, vol. 41, pp. 390–401, 2015.

[5] PV insights: Solar PV wafer weekly spot price. 2013.

[6] Brown, A., Müller, S. and Dobrotkova, Z.: Renewable energy: Markets and prospects by technology. *IEA information paper*, 2011.

[7] Bull, S.: Renewable energy today and tomorrow. *Proceedings of the IEEE*, vol. 89, no. 8, pp. 1216–1226, 2001.

[8] Al Qamer: Solar (PV). [Online], 2016. Retrieved on 30/09/2017. Available at: `http://www.alqamer.com/index.php/2016-02-01-19-25-41/solar-pv`

[9] Lai, W.F., Chen, S.M., Liang, T.J., Lee, K.W. and Ioinovici, A.: Design and implementation of grid connection photovoltaic micro inverter. In: *2012 IEEE Energy Conversion Congress and Exposition (ECCE)*, pp. 2426–2432. Sept 2012. ISSN 2329-3721.

[10] Rodriguez, J. and Cortes, P.: *Predictive Control of Power Converters and Electrical Drives*, pp. 3–39. Wiley-IEEE Press, 2012. ISBN 9781119963981.

[11] Cortes, P., Kazmierkowski, M.P., Kennel, R.M., Quevedo, D.E. and Rodriguez, J.: Predictive control in power electronics and drives. *IEEE Transactions on Industrial Electronics*, vol. 55, no. 12, pp. 4312–4324, Dec 2008. ISSN 0278-0046.

[12] Geyer, T.: *Model Predictive Control of High Power Converters and Industrial Drives*. Wiley, 2016. ISBN 9781119010869.
Available at: `https://books.google.co.za/books?id=KtgQDQAAQBAJ`

[13] Karamanakos, P., Geyer, T. and Kennel, R.: Reformulation of the long-horizon direct model predictive control problem to reduce the computational effort. In: *2014 IEEE Energy Conversion Congress and Exposition (ECCE)*, pp. 3512–3519. Sept 2014. ISSN 2329-3721.

[14] Miranda, H., Teodorescu, R., Rodriguez, P. and Helle, L.: Model predictive current control for high-power grid-connected converters with output LCL-filter. In: *2009 35th Annual Conference of IEEE Industrial Electronics*, pp. 633–638. Nov 2009. ISSN 1553-572X.

[15] Du Toit Mouton, H: Power electronics. University of Stellenbosch, 2014.

[16] Eskom Standardization Section: *Grid interconnection of embedded generation, Part 2, Section 1*. World Energy Council, Pretoria, Republic of South Africa, 2010. ISBN 978-0-626-25101-7.

[17] Tiwari, G. and Mishra, R.: *Advanced Renewable Energy Sources*. Royal Society of Chemistry, 2015. ISBN 9781782625780.

[18] qing Yuan, Q., jie Wu, X., ting Zhang, T. and an Wang, K.: Model predictive control for the high-power grid-connecting pwm converters. In: *2013 International Conference on Electrical Machines and Systems (ICEMS)*, pp. 252–256. Oct 2013.

[19] U.S. Energy Information Administration: *International Energy Outlook 2016*. Office of Energy Analysis, U.S. Department of Energy, Washington, DC 20585, 2016.

[20] for Economic Co-Operation, O. and Development: *World Energy Outlook 2017*. OECD, 2017. ISBN 978-92-64-28205-6.

[21] for Economic Co-Operation, O. and Development: *World Energy Outlook 2016*. OECD, 2016. ISBN 978-92-64-26494-6.

[22] Abbey, C., Robinson, J. and Joos: Integrating renewable energy sources and storage into isolated diesel generator supplied electric power systems. In: *2008 13th International Power Electronics and Motion Control Conference*, pp. 2178–2183. 2008.

[23] Yaramasu, V. and Wu, B.: *Model Predictive Control of Wind Energy Conversion Systems*. IEEE Press Series on Power Engineering. Wiley, 2016. ISBN 9781118988589.

[24] Secretariat, UNFCCC: Report of the Conference of the Parties on its fifteenth session, held in Copenhagen from 7 to 19 December 2009. In: *United Nations Framework Convention on Climate Change*. 2009.

[25] Li, Y., Agelidis, V.G. and Shrivastava, Y.: Wind-solar resource complementarity and its combined correlation with electricity load demand. In: *2009 4th IEEE Conference on Industrial Electronics and Applications*, pp. 3623–3628. 2009.

[26] Secretariat, UNFCCC: Report of the Conference of the Parties on its twenty-first session, held in Paris from 30 November to 13 December 2015. In: *United Nations Framework Convention on Climate Change*. 2015.

[27] South Africa, Department of Energy: *State of Renewable Energy in South Africa*. Department of Energy (DOE), Pretoria, South Africa, 2015. ISBN 978-1-920435-08-0.

[28] Baker, L.: The evolving role of finance in South Africa's renewable energy sector. *Geoforum*, vol. 64, pp. 146–156, 2015.

[29] Eberhard, A.: The future of South African coal: Market, investment and policy challenges. *Program on Energy and Sustainable Development*, vol. 100, pp. 1–44, 2011.
Available at: `http://pesd.fsi.stanford.edu/sites/default/files/WP_100_Eberhard_Future_of_South_African_Coal.pdf`

[30] Eskom: Coal power. [Online], 2017. Retrieved on 15/10/2017.
Available at: `http://www.eskom.co.za/AboutElectricity/ElectricityTechnologies/Pages/Coal_Power.aspx`

[31] World Energy Council (WEC): *World Energy Resources: 2013 Survey*. World Energy Council, London, 2013. ISBN 978-0-946121-29-8.

[32] South Africa, Department of Minerals and Energy: *White Paper on the Energy Policy of the Republic of South Africa*. Department of Minerals and Energy, Pretoria, South Africa, 1998. ISBN 0-9584235-8-X.

[33] Fawkes, H.: Energy efficiency in south african industry. *Journal of Energy in Southern Africa*, vol. 16, no. 4, pp. 18–25, 2005.

[34] Davidson, O., Winkler, H., Kenny, A., Prasad, G., Nkomo, J., Sparks, D., Howells, M. and Alfstad, T.: *Energy policies for sustainable development in South Africa: Options for the future*. Energy Research Centre, University of Cape Town, Cape Town, South Africa, 2006. ISBN 0-620-36294-4.

[35] Nakumuryango, A. and Inglesi-Lotz, R.: South Africa's performance on renewable energy and its relative position against the oecd countries and the rest of Africa. *Renewable and Sustainable Energy Reviews*, vol. 56, pp. 999–1007, 2016.

[36] McCrone, A., Moslener, U., d'Estais, F., Usher, E. and Grüning, C.: *Global trends in renewable energy investment 2016*. Frankfurt School of Finance & Management:, Frankfurt, Germany, 2016.

[37] Twidell, J. and Weir, T.: *Renewable Energy Resources*. 3rd edn. Taylor & Francis, 2015. ISBN 9781317660378.

[38] Agudelo-Vera, C., Mels, A., Keesman, K. and Rijnaarts, H.: Resource management as a key factor for sustainable urban planning. *Journal of environmental management*, vol. 92, no. 10, pp. 2295–2303, 2011.

[39] Ponting, C.: *A New Green History of the World: The Environment and the Collapse of Great Civilizations*. Penguin Books, 2007. ISBN 0-14-303898-2.

[40] Diamond, J.: *Collapse: How societies choose to fail or succeed*. Penguin, 2005. ISBN 0-670-03337-5.

[41] Castellano, J., Ribera, A. and Ciurana, J.: Integrated system approach to evaluate social, environmental and economics impacts of buildings for users of housings. *Energy and Buildings*, vol. 123, pp. 106–118, 2016.

[42] Ellabban, O., Abu-Rub, H. and Blaabjerg: Renewable energy resources: Current status, future prospects and their enabling technology. *Renewable and Sustainable Energy Reviews*, vol. 39, pp. 748–764, 2014.

[43] Ahlfeldt, C., Brent, A., Gumede, D., Guy, D., Mosdell, S., Skeen, J., Spencer, F. and Thompson-Smeddle, L.: *A South African Renewable Energy Guide For Local Government*. Juta, Juta & Company Ltd, First Floor, Sunclare Building, 21 Dreyer Street, Claremont, 7708, 2012. ISBN 9780702186929.

[44] Louwerse, M. and Van Peer, W.: *Thematics: Interdisciplinary Studies*. Converging Evidence in Language and Communication Research Series. John Benjamins Publishing Company, 2002. ISBN 9781588112828.

[45] Femia, N., Petrone, G., Spagnuolo, G. and Vitelli, M.: *Power Electronics and Control Techniques for Maximum Energy Harvesting in Photovoltaic Systems*. Industrial Electronics. CRC Press, 2017. ISBN 9781351832427.

[46] Geyer, T. and Quevedo, D.E.: Multistep finite control set model predictive control for power electronics. *IEEE Transactions on Power Electronics*, vol. 29, no. 12, pp. 6836–6846, Dec 2014.

[47] Scoltock, J., Geyer, T. and Madawala, U.: Model Predictive Direct Power Control for a grid-connected converter with an LCL-filter. In: *Industrial Technology (ICIT), 2013 IEEE International Conference on*, pp. 588–593. Feb 2013.

[48] Scoltock, J., Geyer, T. and Madawala, U.K.: A Model Predictive Direct Current Control strategy with predictive references for MV grid-connected converters with LCL-filters. *IEEE Transactions on Power Electronics*, vol. 30, no. 10, pp. 5926–5937, Oct 2015. ISSN 0885-8993.

[49] Code, G.: High and extra high voltage, e. on netz gmbh bayreuth, germany, april 2006.

[50] Carrasco, J.M., Franquelo, L.G., Bialasiewicz, J.T., Galvan, E., PortilloGuisado, R.C., Prats, M.A.M., Leon, J.I. and Moreno-Alfonso, N.: Power-electronic systems for the grid integration of renewable energy sources: A survey.

IEEE Transactions on Industrial Electronics, vol. 53, no. 4, pp. 1002–1016, June 2006. ISSN 0278-0046.

[51] Takahashi, I. and Noguchi, T.: A new quick-response and high-efficiency control strategy of an induction motor. *IEEE Transactions on Industry Applications*, vol. IA-22, no. 5, pp. 820–827, Sept 1986. ISSN 0093-9994.

[52] Ohnishi, T.: Three phase pwm converter/inverter by means of instantaneous active and reactive power control. In: *Industrial Electronics, Control and Instrumentation, 1991. Proceedings. IECON'91., 1991 International Conference on*, pp. 819–824. IEEE, 1991.

[53] Holtz, J.: Pulsewidth modulation for electronic power conversion. *Proceedings of the IEEE*, vol. 82, no. 8, pp. 1194–1214, 1994.

[54] Blaschke, F.: The principle of field orientation as applied to the new transvektor closed-loop control system for rotating field machines. 1972.

[55] Kazmierkowski, M.P. and Malesani, L.: Current control techniques for three-phase voltage-source pwm converters: a survey. *IEEE Transactions on industrial electronics*, vol. 45, no. 5, pp. 691–703, 1998.

[56] Siwakoti, Y.P., Peng, F.Z., Blaabjerg, F., Loh, P.C., Town, G.E. and Yang, S.: Impedance-source networks for electric power conversion part ii: Review of control and modulation techniques. *IEEE Transactions on Power Electronics*, vol. 30, no. 4, pp. 1887–1906, April 2015. ISSN 0885-8993.

[57] Garcia, C.E., Prett, D.M. and Morari, M.: Model predictive control: theory and practice survey. *Automatica*, vol. 25, no. 3, pp. 335–348, 1989.

[58] Karamanakos, P., Geyer, T., Mouton, T. and Kennel, R.: Computationally efficient sphere decoding for long-horizon direct model predictive control. In: *2016 IEEE Energy Conversion Congress and Exposition (ECCE)*, pp. 1–8. Sept 2016.

[59] Hassibi, B. and Vikalo, H.: On the sphere-decoding algorithm i. expected complexity. *IEEE Transactions on Signal Processing*, vol. 53, no. 8, pp. 2806–2818, Aug 2005. ISSN 1053-587X.

[60] Quevedo, D.E., Aguilera, R.P. and Geyer, T.: Predictive control in power electronics and drives: Basic concepts, theory, and methods. In: *Advanced and Intelligent Control in Power Electronics and Drives*, pp. 181–226. Springer, 2014.

[61] Scoltock, J., Geyer, T. and Madawala, U.K.: A Model Predictive Direct Current Control strategy with predictive references for MV grid-connected converters with LCL-filters. *IEEE Transactions on Power Electronics*, vol. 30, no. 10, pp. 5926–5937, Oct 2015. ISSN 0885-8993.

[62] Mariethoz, S., Beccuti, A.G. and Morari, M.: Analysis and optimal current control of a voltage source inverter connected to the grid through an LCL-filter. In: *2008 IEEE Power Electronics Specialists Conference*, pp. 2132–2138. June 2008. ISSN 0275-9306.

[63] Panten, N., Hoffmann, N. and Fuchs, F.W.: Finite Control Set Model Predictive Current Control for Grid-Connected Voltage-Source Converters with LCL-filters: A study based on different state feedbacks. *IEEE Transactions on Power Electronics*, vol. 31, no. 7, pp. 5189–5200, July 2016. ISSN 0885-8993.

[64] Maccari, L.A., Montagner, V.F. and Lima, D.M.: Model predictive current controller applied to grid-connected LCL-filters. In: *2016 12th IEEE International Conference on Industry Applications (INDUSCON)*, pp. 1–6. Nov 2016.

[65] Yoo, D.K., Wang, L., Rogers, E. and Paszke, W.: Model predictive control of three phase voltage source converters with an LCL-filter. In: *2014 IEEE 23rd International Symposium on Industrial Electronics (ISIE)*, pp. 562–567. June 2014. ISSN 2163-5137.

[66] Pena-Alzola, R., Liserre, M., Blaabjerg, F., Sebastián, R., Dannehl, J. and Fuchs, F.W.: Analysis of the passive damping losses in LCL-filter-based grid converters. *IEEE Transactions on Power Electronics*, vol. 28, no. 6, pp. 2642–2646, 2013.

[67] Bierhoff, M.H. and Fuchs, F.W.: Active damping for three-phase pwm rectifiers with high-order line-side filters. *IEEE Transactions on Industrial Electronics*, vol. 56, no. 2, pp. 371–379, 2009.

[68] Rodriguez, J., Kazmierkowski, M.P., Espinoza, J.R., Zanchetta, P., Abu-Rub, H., Young, H.A. and Rojas, C.A.: State of the art of finite control set model predictive control in power electronics. *IEEE Transactions on Industrial Informatics*, vol. 9, no. 2, pp. 1003–1016, May 2013. ISSN 1551-3203.

[69] Rodriguez, J., Pontt, J., Silva, C.A., Correa, P., Lezana, P., Cortés, P. and Ammann, U.: Predictive current control of a voltage source inverter. *IEEE Transactions on Industrial Electronics*, vol. 54, no. 1, pp. 495–503, 2007.

[70] Geyer, T. and Quevedo, D.E.: Performance of multistep finite control set model predictive control for power electronics. *IEEE Transactions on Power Electronics*, vol. 30, no. 3, pp. 1633–1644, March 2015. ISSN 0885-8993.

[71] Geyer, T., Papafotiou, G. and Morari, M.: Model predictive direct torque control-part 1: Concept, algorithm, and analysis. *IEEE Transactions on Industrial Electronics*, vol. 56, no. 6, pp. 1894–1905, 2009.

[72] Geyer, T.: *Low complexity model predictive control in power electronics and power systems*. Cuvillier Verlag, 2005.

[73] Papafotiou, G., Kley, J., Papadopoulos, K.G., Bohren, P. and Morari, M.: Model predictive direct torque control-part 2: Implementation and experimental evaluation. *IEEE Transactions on Industrial Electronics*, vol. 56, no. 6, pp. 1906–1915, 2009.

[74] Geyer, T.: Generalized model predictive direct torque control: Long prediction horizons and minimization of switching losses. In: *Decision and Control, 2009 held jointly with the 2009 28th Chinese Control Conference. CDC/CCC 2009. Proceedings of the 48th IEEE Conference on*, pp. 6799–6804. IEEE, 2009.

[75] Geyer, T.: A comparison of control and modulation schemes for medium-voltage drives: Emerging predictive control concepts versus pwm-based schemes. *IEEE Transactions on Industry Applications*, vol. 47, no. 3, pp. 1380–1389, 2011.

[76] Scoltock, J., Geyer, T. and Madawala, U.: Model Predictive Direct Current Control for a grid-connected converter: LCL-filter versus L-filter. In: *2013 IEEE International Conference on Industrial Technology (ICIT)*, pp. 576–581. Feb 2013.

[77] Geyer, T.: Model predictive direct current control: Formulation of the stator current bounds and the concept of the switching horizon. *IEEE Industry Applications Magazine*, vol. 18, no. 2, pp. 47–59, 2012.

[78] Sternberg, S.: *Dynamical systems*, pp. 201 – 202. Courier Corporation, 2010.

[79] Karamanakos, P., Geyer, T. and Kennel, R.: Reformulation of the long-horizon direct model predictive control problem to reduce the computational effort. In: *2014 IEEE Energy Conversion Congress and Exposition (ECCE)*, pp. 3512–3519. Sept 2014. ISSN 2329-3721.

[80] Transmission and Distribution Committee of the IEEE Power Engineering Society: *IEEE Std 519-1992, Recommended Practices and Requirements for Harmonic Control in Electrical Power Systems*. IEEE, New York, United States of America, 2004. ISBN 1-55937-239-7.

[81] Holmes, D.G. and Lipo, T.A.: *Pulse width modulation for power converters: principles and practice*, vol. 18. John Wiley & Sons, 2003. ISBN 978-0-471-20814-3.

[82] Scoltock, J., Geyer, T. and Madawala, U.: Model Predictive Direct Current Control for a grid-connected converter: LCL-filter versus L-filter. In: *Industrial Technology (ICIT), 2013 IEEE International Conference on*, pp. 576–581. Feb 2013.

[83] Hours, J., Zeilinger, M., Gondhalekar, R. and Jones, C.: Spectrogram-MPC: Enforcing hard constraints on systems' output spectra. In: *2012 American Control Conference (ACC)*, pp. 2010–2017. 2012. ISSN 0743-1619.

[84] Cortes, P., Rodriguez, J., Quevedo, D. and Silva, C.: Predictive current control strategy with imposed load current spectrum. *IEEE Transactions on Power Electronics*, vol. 23, no. 2, pp. 612–618, 2008.

[85] Wills, A., Bates, D., Fleming, A., Ninness, B. and Moheimani, S.: Model predictive control applied to constraint handling in active noise and vibration control. *IEEE Transactions on Control Systems Technology*, vol. 16, no. 1, pp. 3–12, 2008.